Alma Mater Studiorum – Università di Bologna

DOTTORATO DI RICERCA IN

Scienze ambientali: tutela e gestione delle risorse naturali

Ciclo XXVIII

Settore Concorsuale di afferenza: 04/A4

Settore Scientifico disciplinare: GEO/12

TITOLO TESI

Predictability studies

for Regions Of Freshwater Influence

Presentata da: Giorgia Verri

Coordinatore Dottorato

Prof. Enrico Dinelli

Relatore

Prof. Nadia Pinardi

Esame finale anno 2016

Correlatori:

- **Dr. Paolo Oddo**

  Centre for Maritime Research and Experimentation CMRE, La Spezia, Italia
  Precedentemente: Istituto Nazional di Geofisica e Vulcanologia, Bologna Italia

- **Dr. Antonio Navarra**

  Centro Euro-Mediterraneo sui Cambiamenti Climatici, Italia
  Istituto Nazional di Geofisica e Vulcanologia, Bologna Italia

- **Dr. Joseph Tribbia**

  National Center for Atmospheric Research NCAR, Boulder Colorado

Acknowledgements

I'm endlessly grateful to my advisor Prof. Nadia Pinardi, I would say one of the best meetings of my life, for her constant support and valuable teachings.
I thank her and my Division Director, Dr. Giovanni Coppini, for giving me the chance to spend a visiting period at the National Center for Atmospheric Research, NCAR where I met intense researchers and friends. I feel extremely lucky to have had this opportunity. I'm thankful to my Division Director also for his advices and the time he devoted to my concerns.
I would like to acknowledge my co-tutors Dr. Paolo Oddo, Dr. Antonio Navarra and Dr. Joseph Tribbia, their huge expertise helped me a lot.
I finally would like to thank all my colleagues of OPA Division at CMCC, with whom I share days full of work but also full of smiles.
Last but not least, I want to thank my family, my mother Laura, my father Fulvio, my brother Luigi and my boyfriend Carlo. I am sure that a simple thank you will never be enough to express my gratitude.
This work is dedicated to Carlo, he knows why.

Contents

List of Figures

List of Tables

1 Introduction

1.1 River role in the world ocean circulation and the Mediterranean Sea

Rivers represent the primary link between the land and the ocean in the water cycle. Figure 4.2 shows the riverine freshwater discharge to the global coastal ocean following Milliman and Farnsworth, 2013: the mean annual discharge to the global ocean is estimate to be 36000 km^3/yr. Rivers discharging into the Black Sea and the Mediterranean Sea are estimated to be about 930 km^3/yr and are drawn Fig.4.2 as part of the European drainage into the North Atlantic (green area) which accounts for almost 2100 km^3/yr. The effects of the freshwater discharge are generally confined to the coastal zone of the open ocean, but if the basins receiving the freshwater release are semi-enclosed (i.e. the Mediterranean Sea, the Adriatic sub-basin and the Black Sea) the rivers may strongly affect the basin wide circulation and dynamics.

The literature counts several estimates of the total freshwater discharge into the Mediterranean Sea which have been performed by means of national and international repositories as the Global River Discharge database RivDIS (Vrsmarty et al., 1998), the Global Runoff Data Center (GRDC) hydrological database and the Mediterranean Hydrological Cycle Observing System, Medhycos, data server (Medhycos, 2001) or by means of modelling studies (Ludwig et al., 2009).

Most estimates vary around 400-450 km^3/yr for the Mediterranean Sea and 350-400 km^3/yr for the Black Sea. Major differences among the several databases are due to a strong damming occurred within the last 60 years (Skliris et al., 2007; Vervatis et al., 2013) in the Eastern and Western Mediterranean sub-basins involving their major freshwater sources (i.e. the construction of the Aswan Dam along the Nile, the damming of the Ebro river and the Russian rivers draining into the Black Sea).

Rivers flowing into the Adriatic Sea currently provide almost 1/3 of the total runoff of the Mediterranean basin with an annual rate estimate varying from 133

km^3/yr (Vrsmarty et al., 1998) to 164 km^3/yr (UNEP, 1978). In details the "river runoff" represents about 80% of the annual freshwater rate into the Adriatic Sea. About 19% of the total runoff rate is not conveyed by rivers but enters the sea as "land runoff" particularly along the dalmatian coast and an additional 1% is caused by "submarine springs" mostly near the eastern coast (Struglia et al., 2004). The river runoff in the Adriatic basin is mainly due to the Po river, carrying alone about 28% of the basin annual value, 19% comes from the other rivers along the northern coast (mainly Adige and Isonzo), 45% comes from the eastern coast (Buna/Bojana, Vjose and Neretva among the others), and the remaining 8% from the western coast (Raicich, 1996).

As know from the literature, the whole Mediterranean Sea is a "concentration basin" (Pinardi et al., 2006; Cessi and Pinardi, 2014) with negative annual heat flux meaning the net heat flux is upward oriented (-7 Wm^{-2} following Pettenuzzo et al., 2010), and positive annual freshwater flux (defined as evaporation minus precipitation and runoff) meaning that evaporation prevails on precipitation and runoff (0.64 m/yr following Pettenuzzo et al., 2010). The Adriatic Sea is instead a "dilution basin" (Pinardi et al., 2006) with a well marked negative annual heat flux (-33.2 Wm^{-2} following Pettenuzzo et al., 2010), but also a negative annual freshwater flux (-1.14 m/yr following Artegiani et al., 1997 a-b). The sign of the freshwater flux of the Adriatic basin is due to river runoff since evaporation and precipitation tend to balance each other on annual basis.

This work focuses on the Central Mediterranean Sea, which is composed of the Adriatic Sea in its northernmost extension and the Ionian Sea in its southern part, communicating each other at the Otranto Strait. We point out the Central Mediterranean Sea is one of the few Mediterranean areas where river runoff is important for the coastal as well as the open sea overturning circulation. As far as we know, there are few evidences in the literature of river effects on on the basin wide overturning circulation. Only Rahmstorf (1995) speculates an increasing freshwater inflow in the Northern Atlantic is potentially able to reduce or even shut down the local overturning circulation. Previously Skliris et al., 2007 and Somot et al., 2006 pointed out river role on the dense water formation processes of the Mediterranean basin. Spall (2012) demonstrates that, in marginal sea

areas as the Adriatic Sea, an increase in surface freshwater gain (due to both precipitation and runoff) can lead to a shutdown of water sinking and dense water formation, and the marginal sea Meridional Overturning Circulation may switch from anti-estuarine to estuarine mode.
River role on the Central Mediterranean Meridional Overturning Circulation, expecially on its downwelling branch in the Adriatic Sea, is here presented for the first time.

1.2 Structure of the Regions Of Freshwater Influence

Several theoretical as well as modeling studies (Simpson et al, 1993; Kourafalou et al, 1996; Kourafalou, 1999; Schiller and Kourafalou, 2010) pointed out the freshwater discharge radically affects the shelf areas adjacent to the estuaries, the so called Regions of Freshwater Influence (ROFIs).
A ROFI system experiences a physical regime that is radically different from the other parts of the shelf sea, where the wind stress, the surface heating-cooling and the tidal currents represent the predominant mechanisms of the buoyancy budget. Simpson (1993) and Garvine(1999) among the others have shown that the input of freshwater in a coastal area generates baroclinic dynamics. This means that river discharge creates its own local circulation: the freshwater inflow spreads offshore of the river mouth and promotes the water column stratification and the local overturning circulation (Chapman and Beardsley 1989).The resulting dynamical structure in the coastal region is the so called 'buoyant river plume' which consists of an offshore bulge turning anticyclonically plus a coastal alongshore current due to the geostrophic adjustment.
The offshore expansion of the buoyant river inflow into the continental shelf has been widely investigated in the literature: Yankovsky and Chapman (1997) categorized river plumes as 'surface advected plumes' and 'bottom advected plumes' based on the properties of the estuarine outflowing water: the outlet width, the

outlet depth, the velocity and density of the river discharge. The surface advected plume (Figure 4.3) develops when inflowing water remains on the top layer of the shelf area with the ambient dense water below. It spreads mainly radially and results in an offshore cyclostrophic bulge which is attached to the estuary and turns anticyclonically; a surface along-shore current due to the geostrophic adjustment is also present but very narrow. On the other hand, the bottom advected plume (Figure 4.4) is tipically established when the buoyant inflow occupies the entire water column into a depth greater than the outlet depth and its offshore transport is controlled by the advection in the frictional bottom boundary layer. The related coastal current remains in contact with the bottom while moving offshore, with the density front extending from the surface to the bottom. Generally high density difference between the plume and the ambient flow favors the surface advected plume while a bottom advected plume is established if the buoyant inflow shows a high volume transport.

More recent developments (Garvine and Whitney, 2006; Mac Cready 2009; Mac Cready and Geyer, 2010 among the others) focused on understanding which role the salt ocean water entering the estuary plays in the resulting river plume (Figure 1.4). Thus the estuary dynamics started to be investigated jointly with the coastal ocean dynamics and the characteristics of "sharply stratified", "partially stratified" and "well mixed" estuaries have been pointed out as well as their effects on the resulting river plume. A sharply stratified estuary is generally established when the "flow ratio", defined as the tidal velocity over the river streamflow velocity, is less than 0.1 with a sharp vertical salinity gradient. A partially stratified estuary shows a flow ration between 0.1 and 10 meaning that the tidal flow is comparable with the river flow and a relatively vigorous mixing in the vertical smooths the salinity gradient. A well mixed estuary shows a flow ratio major than 10 and the tidal pumping is so vigorous that the salinity is homogeneous in the vertical and varies in the horizontal (Fischer et al., 1979).

The shape and dynamics of a river plume are also affected by external forcings, mainly wind stress and tides. The predominant role of tides or wind stress on river plume depends on the strength of both wind stress (i.e. wind intensity and direction with respect to surface currents) and tides (i.e. spring or neap tides,

ebb or flood tides) as well as on the relative distance of the plume with respect to the outlet (Chen and MacDonald, 2006). The plume dynamics has been proved to be strongly tidal in the so called "near-field plume" (Jirka et al, 1981), that is immediately out of the river outlet and corresponds to the excursion length of ebb tides. The tidal effect changes during a whole tidal cycle depending on flood or ebb tides: during flood currents the tidal pumping is onshore directed and favors the ocean water entrainment into the estuary and thus the mixing of the water column; during the ebb currents the tidal pumping is offshore directed and tends to bring river freshwater seaward, thus increasing the stratification of the water column in the shelf area (Guarnieri et al, 2014). Winds affect the river plume as well: the downwelling winds favour the homogenization of water column and tend to turn the plume into an along-shore current while the upwelling winds promote the water stratification and the offshore drift (Chao, S. Y., 1987). The role of wind stress prevails on tides as the buoyant river inflow moves far from the outlet. This area is named "far field plume", and here the wind mixing removes the increased stratification due to the freshwater discharge and leads to the irreversible turning of river water into shelf water (Mac Cready 2009).

1.3 Numerical modeling the coastal water cycle

Modeling the spatial and temporal distribution of the water cycle is a challenge because water cycle processes span a wide range of spatial and temporal scales and because many human activities influence the water cycle.

Integrated meteo-hydrological modelling system are essential to improve the representation of the whole water cycle both on local and large scales pointing to the reconstruction of historical events as well as the short term forecasts of extreme events and the assess of future scenarios.

Most meteorological and climatological models still represent the surface and subsurface processes of the water cycle in a oversimplified way, by using a "column-only" land surface sub-model and without accounting for the lateral routing of

surface and subsurface water flow.

Hydrological modelling got limited success in the past due to the lack of observational datasets and surface and subsurface input data (Nickovic et at., 2010). However during the last decades, the availability of hydrological observations has improved; moreover higher-resolution data on topography, river routing, soil types and land use have become available.

Hydrology modelling covers a huge variety of approaches: from easier methods (i.e. conceptual and parametric models) to more complex wave systems (i.e. kinematic, diffusive or dynamic wave models).

As far as we know the HYdrology surface runoff PROgnostic Model,HYPROM (Nickovic et al., 2010), is currently the only hydrological modeling system with fully prognostic equations for overland water flow but it doesn't represent the subsurface physical processes as the groundwater drainage, the saturated subsurface water flow and the aquifer water storage. In this study we use the WRF-Hydro system (Gochis et al., 2013) which is based on the diffusive wave approximation for representing both the overland water flow and the river streamflow. Moreover it solves the subsurface soil physics and is 2-way coupled with NOAH-MP (Niu et al., 2011) land surface model.

The quality of meteo-hydrological modelling is a demanding issue. Precipitation forecasting is still one of the most critical task for meteorological mesoscale models since the precipitation field is the end result of many multi-scales processes interacting each other and is sensitive to topography, soil types and land use conditions. Moreover the grid spacing of mesoscale models is in the range of "gray-zone" (Moeng et al., 2007; Shin et al., 2013) resolutions for convection, where the power spectrum of the turbulence reaches its peak and thus the convective motions and the precipitation are only partially resolved.

The quality of meteorological modelling is critical for ensuring the quality of hydrological modelling as the uncertainties associated with the meteorological simulations propagate into the hydrological models (Pappenberger et al., 2005). Finally the hydrological models rely on many parameterised processes with tunable coefficients requiring a calibration procedure.

Several advances have been achieved in the coupling between hydrology and at-

mosphere models or between ocean and atmosphere models, while the link of hydrological and ocean models is still poorly investigated and the ocean models treat the river discharge in a simplified way for both short term predictions and long term scenarios (e.g. climatological discharge and zero or constant salinity at river mouths).

Moreover literature shows several modelling studies dealing with ROFI's regime and river water turning into shelf water, while only few studies have started to explore the salt ocean water entrainment into the estuarine areas and how this conditions and perhaps drive the net freshwater release at river outlets.

The ocean models neglect the energy and water balance occurring into the estuary and the exchange-flow triggered by the ocean water entrainment, which conditions the net freshwater release. Moreover the freshwater release at river outlets is usually parameterises by means of climatological discharge and zero or constant salinity. We pointed out rivers affect the coastal as well as the basin wide circulation and dynamics, thus the performance of regional ocean models is expected to be strongly dependent on a comprehensive and effective representation of the estuary dynamics and the net freshwater release.

On the whole the reliable representation of the streamflow along the river network as well as the water exchange at the estuaries are challenging tasks of the numerical modelling and are both assessed in the presented study.

1.4 Objectives and structure of the thesis

The aim of this study is to understand and to assess the effects of river freshwater inflow on the circulation and dynamics of our region of interest, the Central Mediterranean Sea, both on shelf and basin scales, over short-term as well as long-term range.

As far as we know this study provides the first investigation on river role on the Central Mediterranean overturning circulation.

On the same time we point to improve the hindcast/forecast capability of our regional hydrodynamics model both on shelf and basin scales through a consistent representation of river inflow into the Central Mediterranean Sea taking not

account all the physical processes involved in the local water cycle of specific catchments. An integrated modelling system including the atmosphere, the hydrology and the estuary dynamics has been set up upstream the regional ocean model at the Ofanto river outlet. The Estuary Box Model developed by the University of Connecticut (UCONN) jointly with the National Centre for the Atmospheric Research (NCAR) Climate Global Division and the University of Washington (UW) has been implemented for the selected case study, the Ofanto river, downstream of the meteo-hydrological chain and upstream of the regional ocean model. The model performance has been evaluated by comparison with a highly simplified approach based on Knudsen's relation (Knudsen, 1900). Finally we built up an intermediate modelling approach.

The thesis is organised as follows.

Chapter 2 describes a set of twin experiments, which either does or does not account for the river inflow respectively. Rivers are treated as surface point sources of climatological discharge and salinity. The spanned period is from the beginning of 1999 to the end of 2012 and a high resolution marine hydrodynamics model based on Nucleus for European Modeling of the Ocean code, NEMO (Madec et al, 2008), has been set. These experiments aim to point out river role on the estuarine/anti-estuarine character of the Adriatic Sea circulation, the Adriatic Dense Water Formation processes and the Central Mediterranean anti-estuarine meridional overturning circulation developing between the Adriatic basin and the open Ionian Sea. The set-up of the integrated modeling system including the atmosphere, the soil processes and the hydrology/hydraulics is described in Chapter 3. The implemented chain consists of the mesoscale meteorological model WRF-ARW (Skamarock et al., 2008), the land surface model NOAH-MP (Niu et al., 2011) and the hydrological model WRF-HYDRO (Gochis et al., 2013). The strategy we adopted consists of a dynamical downscaling approach moving from the regional scales of the atmospheric modeling to the catchment scales for the hydrology/hydraulics purposes. We chose the Ofanto river catchment and its estuary as a relocatable case study. The Ofanto is a semi-perennial river with a mean annual value at its outlet of about 15 $m^3 s^{-1}$, but may significantly increase its runoff when heavy rain events occur and eventually floods. Chapter 4

is divided into two parts. First part offers a theoretical discussion on the modelling of the estuarine dynamics. Two approaches are tested and compared: the Knudsen's relation and a steady-state and tidal-cycle averaged 2-layer box model developed by UCONN and NCAR (Garvine and Whitney, 2006). Moreover a new approach is developed and here presented. The second part of Chapter 4 focuses on the coupling of the the estuary dynamics representation with the regional ocean model. The added value of representing the water exchange into the estuaries is discussed as well as the capability of the regional ocean model to simulate the resulting buoyant river plume.

An overall summary of the performed work and the conclusions are offered in Chapter 5. The papers written during the PhD project and the talks held at the workshops I joined are listed in an additional section.

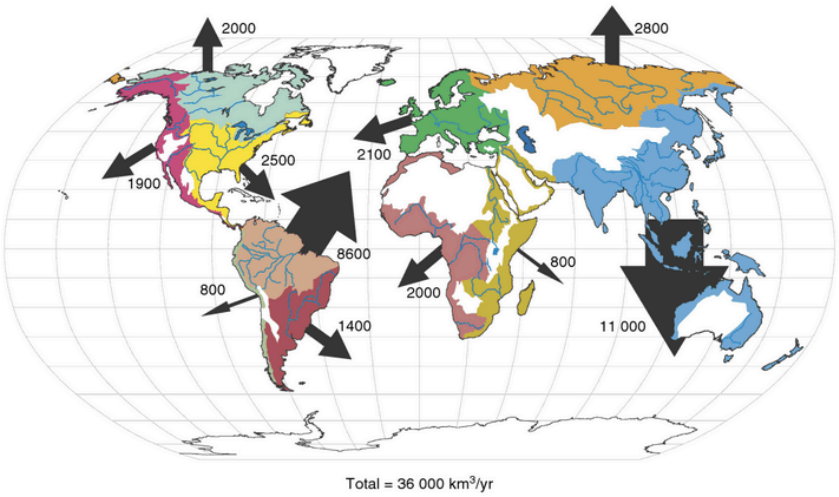

Figure 1.1: Fluvial discharge of freshwater to the global coastal ocean. Numbers are mean annual discharge (km^3/yr); the arrows are proportional to these numbers (from Milliman and Farnsworth, 2013)

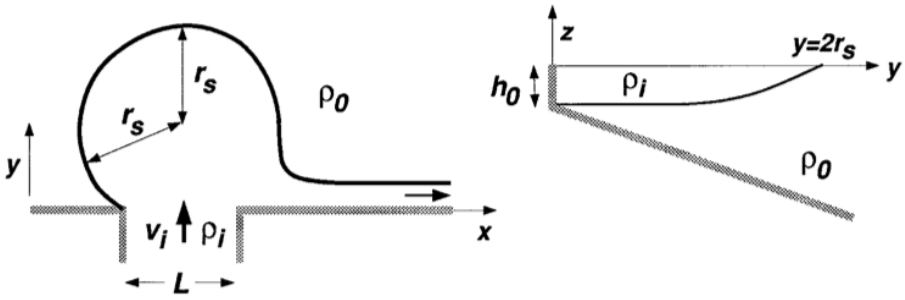

Figure 1.2: Schematic of a surface advected plume (from Yankovsky et Chapman, 1997)

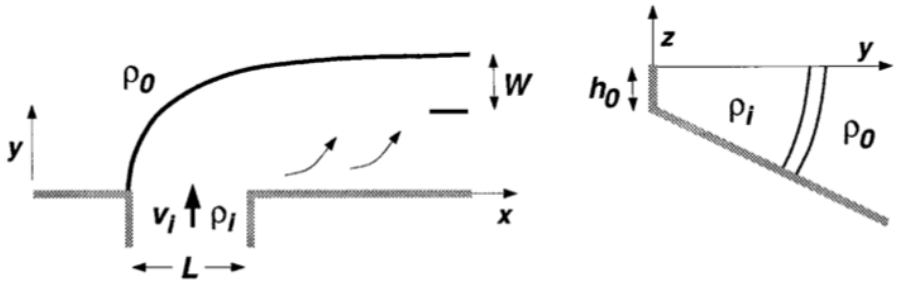

Figure 1.3: Schematic of a bottom advected plume (from Yankovsky et Chapman, 1997)

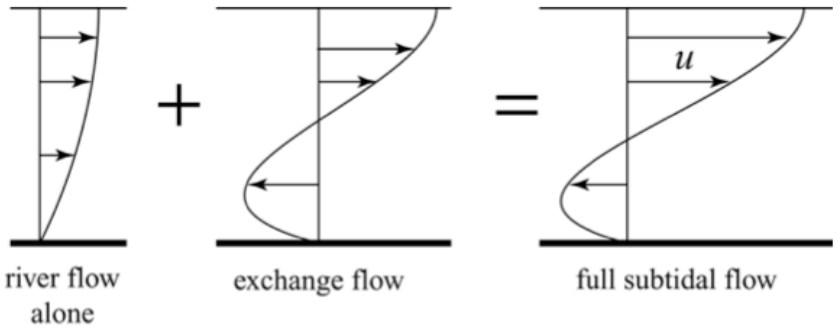

Figure 1.4: Schematic of the components of estuary vertical profile of velocity

2 River effects on the overturning circulation and dynamics of the Central Mediterranean Sea

Preamble

This chapter is a co-authored paper with N.Pinardi, P. Oddo, S.A. Ciliberti and G.Coppini, entitled "Influence of river runoff in the Central Mediterranean Sea basins" and submitted to the Ocean Dynamics.

The role of riverine freshwater inflow in the Central Mediterranean Sea is studied using a high-resolution ocean model with a complete distribution of rivers in the Adriatic and Ionian catchment areas. The impact of river runoff on the Adriatic and Ionian Sea basins is assessed by two twin experiments, with and without river inflow, from 1999 to 2012. This study underlines, for the first time, how river discharge affects the intensity of the Central Mediterranean Meridional Overturning Circulation (MOC), especially its northern downwelling branch in the Southern Adriatic. It is found that the Central Mediterranean Sea is characterized by a persistent anti-cyclonic, anti-estuarine MOC with secondary estuarine cells that strengthen in years of large river runoff due to an enhanced stratification close to the surface and a more stagnant circulation at the bottom. It is found that the Adriatic Sea is dominated by an anti-estuarine dynamics, also when large and anomalous river runoff occurs and the resulting buoyancy budget is positive or null. However rivers act on favoring lower kinetic energy circulation of the Adriatic basin and thus weaken the intensity of the antiestuarine MOC. We found rivers strongly reduce the Adriatic dense water formation, not only in the northern sub-region where the major discharge is concentrated, but also in its southern area by modifying the local water stratification. On the whole the Central Mediterranean MOC is deonstrated to be controlled by wind forcing at least as much as by buoyancy which includes river runoff.

2.1 Introduction

River discharge is one of the components of the water budget in the Mediterranean basin, together with evaporation, precipitation and the net inflow of freshwater from the Atlantic ocean through the Strait of Gibraltar and from the Black Sea through the Dardanelles Strait. Annual water losses due to evaporation exceed water gains from precipitation and river runoff resulting in a positive surface freshwater budget, defined as evaporation minus precipitation and runoff (*i.e.*$0.64m/yr$ following Pettenuzzo et al., 2010). Moreover, the net heat budget of the basin is negative (Bethoux, 1979; Pettenuzzo et al., 2010), thus the Mediterranean Sea is a "concentration basin".

The general characteristics of the Mediterranean thermohaline circulation are schematized in Figure 2.1. This circulation is characterized by inter-annual as well as multi-decadal time scales and it is driven by three major conveyor belts: the Zonal Overturning Circulation (ZOC) in the Southern Mediterranean propelled by the Gibraltar stream flow and Levantine Intermediate Water (LIW) formation processes, the Western Mediterranean Meridional Overturning Circulation (MOC) originating in the Gulf of Lion, the Central Mediterranean MOC originating in the Adriatic Sea (Figure 2.1). These overturning cells are triggered by buoyancy losses and water mass sinking which occur in the open ocean areas of the Northern Mediterranean Sea and the Levantine sub-basin. Both deep and intermediate waters form in the regions offshore the Gulf of Lions, in the Southern Adriatic and in the Northern Levantine Basin, forced by intense winter heat losses and influenced by the presence of large scale permanent cyclonic gyres driven by wind stress curl (Pinardi et al., 2006). The Aegean Sea is marked as another dense water site in Figure 2.1 (red spiral), but Roether et al. (1996) demonstrated it played a relevant role only during the Eastern Mediterranean Transient, EMT, occurred at the end of the eighties and first half of the nineties. Moreover Manca et al. (2003) have found that the Aegean Sea has stopped the production of deep waters after the occurrence of the EMT and that the Adriatic Sea has started to be again the unique site of production of the deep waters for the Eastern Mediterranean sub-basin.

The Central Mediterranean Sea area, composed of the Adriatic Sea in its northern part and the Ionian Sea in its southern extension, is one of the few Mediterranean Sea areas where river runoff is important for the coastal as well as the open sea circulation, not only in the Adriatic Sea, where most of discharge is located (i.e. about 1/3 of the whole Mediterranean river discharge following Ludwig et al., 2009), but also in the Ionian Sea because the Adriatic Sea dense waters are one of the major drivers of the Ionian abyssal circulation (Curchitser et al., 2001, Manca et al., 2002). Moreover the Southern Adriatic opean-sea convection represents the downwelling branch which drives the overturning circulation pattern in the Central Mediterranean sub-basin.

As far as we know this is the first study on river influence on the Central Mediterranean MOC, similarly to Rahmstorf's speculation (Rahmstorf, 1995) on freshwater role on the Northern Atlantic overturning circulation.

Previously Skliris et al., 2007 investigated the impact of reduced discharge of Ebro and Nile rivers on the dense water formation in the Eastern and Western Mediterranean sub-basins and Somot et al., 2006 pointed out river role on the dense water formation processes of the Mediterranean basin in a transient climate change simulation with lower river runoff. On the other hand the role of freshwater inputs (due to both rivers and precipitations) on the dynamics of a marginal sea, as the Adriatic basin, has been widely investigated in the literature. Spall (2012) demonstrates that, in marginal sea areas, an increase in surface freshwater gain can lead to a shutdown of dense water formation and sinking, and the marginal sea Meridional Overturning Circulation (MOC) switches from anti-estuarine to estuarine mode. Recently, Cessi et al. (2014) established that the estuarine/anti-estuarine character of a semi-enclosed sea with a two-layer flow at the strait is determined by both wind and buoyancy forcings. The wind forcing is normally a source of mechanical energy for the circulation, while the buoyancy forcing could be either an energy source or a sink depending on the sign of the net buoyancy flux at the surface. For estuarine basins, such as the Baltic and Black Sea, the positive buoyancy flux (dominated by precipitation and runoff exceeding evaporation), is a net energy sink for the circulation, thus producing a less vigorous meridional circulation than in the anti-estuarine basins.

The Adriatic Sea is a "dilution basin" with a negative annual freshwater budget of about $-1myr^{-1}$ (Artegiani et al., 1997), mainly due to river runoff and a negative annual heat budget. The buoyancy flux, which is a combination of the net heat and freshwater fluxes, could eventually be positive, thus determining a net sink in energy and possibly a net estuarine character of the circulation. Pinardi et al. (2006) show that, due to river runoff, the Adriatic Sea could be characterized by zero net buoyancy flux, thus producing a basin where the circulation is mainly powered by the wind stress. However, the energetics proposed by Cessi et al. (2014) cannot be applied satisfactorily to the Adriatic Sea, since the flow at Otranto is not just a two-layer flow. Thus, a comprehensive analysis of surface buoyancy and meridional transport is needed to fully establish the estuarine/anti-estuarine character of the Adriatic Sea circulation.

In order to evaluate the Central Mediterranean MOC we need to characterize the Adriatic Sea circulation and its forcings since the MOC downwelling branch starts there. Having a large freshwater budget, which makes the Adriatic basin a dilution basin as explained above, it is key to study the influence of runoff on the Adriatic Sea overturning circulation and its possible effects on the MOC. Two main questions are addressed by the present paper: is the Adriatic Sea an estuarine or anti-estuarine basin in a realistic runoff regime? How is the Central Mediterranean MOC affected by rivers? Related issues regarding how rivers affect the formation processes of Adriatic dense waters and their spread toward the Ionian Sea are also addressed.

In order to answer these questions, a high resolution general circulation model was set up, forced by realistic fluxes of water, heat and momentum. The impact of freshwater inflow on the circulation is assessed by studying a twin experiment based on a mechanistic approach: the full dynamics case is close to reality (EXP1) so that taking out just the rivers (EXP2) we can estimate their theoretical effect on the circulation.

The paper is organized as follows. Section 2 outlines the experimental design, and details the parameterization of the rivers as surface boundary conditions and the validation of the model performance. Sections 3 to 6 describe the experiments highlighting the role of the river runoff forcing. A summary and conclusions are

presented in the last section.

2.2 Experimental design

2.2.1 Model configuration and twin-experiment set-up

The numerical model used is the Nucleus for European Modelling of the Ocean (NEMO) in its latest version (Madec, 2008). It is a three-dimensional finite difference numerical model adopting the Boussinesq and hydrostatic approximations. The area covered by the model grid is the Central Mediterranean Sea from $12.2°E$ to $21.0°E$ and $30.2°N$ to $45.8°N$ with a horizontal resolution of about 2.2 km (2.5 km in the meridional direction and 1.7 to 2.2 km in the zonal direction).

Figure 2.2 shows the bathymetry of the domain, river mouth grid points and the three sub-regions into which the Adriatic Sea is conventionally subdivided on the basis of its bottom morphology: the Northern (NAd), the Middle (MAd) and the Southern Adriatic (SAd). The connection with the Ionian Sea occurs at the Otranto Strait where the sill is 800m deep, located at approximately $40°N$.

Two twin experiments were performed, with and without river discharge, spanning the period from 1 Jan 1999 to 31 Dec 2012. The time series of the kinetic energy integrated over the basin volume show the model spin up period consists of the first few months of 1999, thus the whole 1999 is assumed to represent the model spin-up and results for this year are not shown.

We later refer to the two simulations, with and without river discharge respectively, as Experiment 1 (EXP1) and Experiment 2 (EXP2).

It's worth stressing that the conceptual paradigm of the paper is to explain the role of river inflow but not to fully reproduce reality. To do this, we adopt a mechanistic approach: the full dynamics case (EXP1) is close to reality so that if we take out just the rivers (EXP2) we can estimate their theoretical effect on the circulation.

To note that this study offers the first implementation of NEMO code over the Central Mediterranean Sea area, with even a complete representation of almost

all the rivers flowing into the Central Mediterranean Sea. In this work the regional model is forced by a 1/16° resolution dynamical downscaling of the daily analysis of the operational Mediterranean forecasting System, MFS (Tonani et al., 2008; Pinardi and Coppini, 2010) which is based on the same NEMO engine and covers the entire Mediterranean basin.

We found out a tuning procedure is required in order to optimize the horizontal eddy viscosity and diffusion coefficients of our model, starting from the constant values customized for MFS configuration and considering that both models use a biharmonic operator for the horizontal mixing terms but horizontal resolutions are in the ratio 1:3.

A further difference with the mother model MFS is that TKE turbulence closure scheme is used (Mellor and Blumberg, 2004) for computing the vertical eddy viscosity and diffusivity coefficients instead of using a local Richardson number dependent formulation (Pacanowski and Philander, 1981).

All the details on the numerical model configuration are given in Appendix A.

2.2.2 River runoff parameterization and datasets

River runoff into the Mediterranean Sea is mainly concentrated in the Central Mediterranean sub-basin, whit rivers flowing into the Adriatic Sea providing almost 1/3 of the total (Struglia et al., 2004; Ludwig et al., 2009). Furthermore a strong damming occurred within the last 50 years in the Eastern and Western sub-basins involving their major freshwater sources. After the construction of the Aswan Dam in 1964, the runoff of the Nile, the river with the largest water load and drainage basin in the Mediterranean until the early sixties, was drastically reduced (by more than 90%, from 2700 m^3s^{-1} to 150 m^3s^{-1}), affecting the salt budget of the basin. The runoff of the Ebro River, one of the major rivers draining into the Western Mediterranean Basin, was also abruptly reduced (by more than 60%, from 1500 m^3s^{-1} to 400 m^3s^{-1}) due to damming in the early sixties. Finally the control of the Russian rivers draining into the Black Sea started in the fifties with the runoff decrease reaching about 60 km^3/yr at the mid-nineties (Skliris et al., 2007; Vervatis et al., 2013).

Thus currently the only major runoff sources located out of the Central Mediterranena Sea are the Rhone and the Ebro rivers flowing into the Western sub-basin. The freshwater discharge into the Central Mediterranean Sea is almost totally concentrated along the Adriatic coastlines: the Po river is the main freshwater source of the Central Mediterranean Sea and accounts for almost 30% of the Adriatic annual discharge (Cushman-Roisin et al., 2002). Besides the Po, other significant freshwater inputs are the Buna/Bojana, Vjose and Neretva along the Eastern Adriatic coast, and the Adige and Isonzo along the northern Italian coast. Moreover the Mediterranea Sea counts on a great number of very small rivers (Milliman, 2001), owing to strong topographic relief favouring the formation of small watersheds.

This study provides the first numerical representation of all the rivers draining into the Central Mediterranena Sea, there are 67 Adriatic and Ionian rivers in total, 52 flowing into the Adriatic Sea and 15 into the Ionian Sea. Model rivers are parameterized as "surface sources" of runoff and salinity at the estuary grid points while no temperature information is prescribed. Our assumption of no temperature differences between river inflow and shelf sea is generally valid as river plumes are controlled by the salinity gradient.

To note that all the other major rivers flowing into the Western and Eastern sub-basins (i.e. the Ebro, Nile and Rhone rivers) are parameterizes as monthly climatologies of runoff and salinity in the mother model MFS; the net inflow at Dardanelles Strait is also parameterized as a river with monthly climatological runoff and salinity values taken from Kourafalou and Barbopoulos (2003).

Moreover sensitivity tests carried out with MFS mother model in the shelf areas close to river outlets suggest to set salinity values equal to 15 psu for all rivers, except 17psu for the Po river due to the extensive tidal mixing occurring in the Po delta. We maintain the same choice in our model configuration. Discharge values consist of monthly climatologies for all the parameterized rivers, except daily observations for the Po river.

Monthly climatologies are applied in the middle of each month after a preliminar correction following the Killworth's procedure (1996), which produces new monthly "pseudo-values" and preserves the original monthly values when linear

daily interpolation is applied.

The Po river data, which are not climatologies but daily averages based on ARPA EMR 30 minute observations at the Pontelagoscuro station, are unequally divided into nine grid points representing the nine branches of the delta (Po di Goro, Po di Gnocca, Po di Tolle, Po di Bastimento, Po di Scirocco, Po di Bonifazi, Po di Dritta, Po di Tramontana, Po di Maistra) according to percentages in Provini et al. (1992). It is worthy to highlight that the observational dataset of the Po river is the only one available over the simulation period, but working at least with the daily observations of the Po river enabled us to capture most of the interannual variability of the riverine freshwater release in the Central Mediterranean Sea, being mainly due to the Po river. Moreover, as mentioned before, we point to explain the theoretical role of a realistic river inflow but not to fully reproduce reality, thus any weaknesses of our numerical set up and data choice don?t impact our speculation that focuses on the differences we found out by means of a mechanistic approach.

We parameterize river outlets as surface sources of runoff and salinity and we use a "natural boundary condition" (Huang, 1993), plus ad-hoc salt values prescribed at river mouths. Most of previous modeling studies represented river discharge in the Mediterranean Sea by means of the "virtual salt flux boundary condition" as Somot et al, 2006 while Kourafalou, 1996, Skliris et al., 2007 and Vervatis et al., 2013 adopted the so called "natural boundary condition". The virtual salt flux formulation or "mixed boundary condition" (Bryan, 1986) prescribes freshwater flux as additional salt flux added to the salt flux boundary condition allowing the concentration-dilution effect to be represented. This is the approach generally assumed in the ocean general circulation models with rigid lid hypothesis, eventually jointly with a restored sea surface salinity.

The natural boundary condition (Huang, 1993) prescribes freshwater flux as a volume surplus of zero-salinity water, modeled as a correction to the model's top sigma layer vertical velocity at the grid points covering the source locations. Thus a real freshwater flux is specified as the vertical velocity boundary condition for the continuity equation while the salt flux through the surface is set equal to zero. Kourafalou, 1996 was the first to extend the natural boundary condition

to the riverine freshwater flux. Moreover Beron-Vera et al. (1999) introduces a complementary non-zero salt flux at river outlets through ad-hoc salt values in the salt flux boundary condition. Indeed in this model we use the natural boundary condition for vertical velocity and a complementary non-zero salt flux. The surface boundary condition for vertical velocity reads:

$$w \mid_{z=\eta} -\frac{\partial \eta}{\partial t} + (u, v) \mid_{z=\eta} \cdot \bigtriangledown_H \eta = (E - P - \frac{R}{A}) \tag{2.1}$$

where w is the vertical velocity, η is the sea surface height, E is the evaporation rate (ms^{-1}) computed from the latent heat flux (see eq.(A.14) in Appendix A) and thus function of the ECMWF atmospheric data with 6h frequency, P is the precipitation rate (ms^{-1}) coming from CMAP (CPC, Climate Prediction Center, Merged Analysis of Precipitation) monthly climatologies, R indicates the river runoff (m^3s^{-1}) we provide at the grid points representing the outlets and A stands for the river mouth cell areas. Further details and the complete description of the numerical set up are provided in Appendix A.

The complementary salt flux boundary condition is also:

$$K_t \frac{\partial S}{\partial z} \mid_{z=\eta} = S_{z=\eta}(E - P - \frac{R}{A}) \tag{2.2}$$

where K_t is the vertical mixing coefficient for tracers and $S_{z=\eta}$ is the ocean model surface salinity except prescribed ad-hoc salt values at river mouths.

To note the inter-annual variability of the surface water (and consequently salinity) flux through the surface boundary conditions written above is driven only by variation in the evaporation flux and in Po river regimes. This is a lack of our configuration since the interannual variability of the freshwater gains of the Mediterranean basin is only due to the Po river regime and doesn't account for the precipitation variations and the other rivers regime. However there are no consequences on our theoretical purpose that is to assess how rivers affect the basin dynamics just including or not their parameterization in the model set up. Daily time series of total discharge in the model domain during the simulation period (1 Jan 1999 to 31 Dec 2012), are shown in the top panel of Figure 2.3, while the Po's daily discharge is displayed in the bottom panel. According to our discharge data, the annual average runoff rate in the Central Mediterranean

Sea is equal to $4.72 \cdot 10^3 m^3 s^{-1}$, 29.7% coming from the river Po. Moreover 94.6% due to the Adriatic rivers, and 5.4% to the Ionian rivers. Maximum values of the total daily discharge were observed in autumn 2000, autumn 2002, and autumn 2008-winter 2009. Annual mean peaks took place in 2000 ($5.28 \cdot 10^3 m^3 s^{-1}$), 2002 ($5.19 \cdot 10^3 m^3 s^{-1}$), 2009 ($5.37 \cdot 10^3 m^3 s^{-1}$), and 2010 ($5.26 \cdot 10^3 m^3 s^{-1}$).

Table 2.1 lists the adopted climatological datasets for river runoff, the time range for computing the monthly climatologies and the annual mean discharges as useful reference values.

Most of the datasets consist of observations taken at the hydrometric stations nearest to river mouths, and few of them are estimated values. Time series for the various rivers cover different periods. However, the time series of the major rivers, accounting for the most of the Central Mediterranean discharge, overlap for at least 20 yr.

All river mouths are "point sources" except for 2: Marecchia to Tronto rivers (Tronto excluded) in the Marche region and Vibrata to Fortore rivers (Fortore excluded) in the Abruzzo and Molise regions which are "diffused sources" and thus, were split among several grid points. These diffused sources and the rivers in Puglia are the only rivers of the model based on Raicich's (1996) climatologies (see Figure 2.2).

The estimated discharge into the plain between the Po and the Marecchia was divided between eight sources: Po di Volano, Reno, Lamone, Fiumi Uniti, Bevano, Savio, Rubicone, and Uso. The Bacchiglione and Agno-Gu rivers flow into the Brenta river before reaching the sea, thus their runoff was not considered. The plain between the Brenta and the Piave corresponds to the hydrographic basin ending in the "Venice Lagoon", thus the monthly flow was divided among the three main lagoon outlets: Porto di Chioggia, Porto di Malamocco, and Porto di Lido. In the plain between the Piave and the Tagliamento, the outflow was divided among 4 main rivers: Livenza, Sile, Canale Nicessolo and Canale dei Lovi. The plain between the Tagliamento and the Isonzo (Malacic and Petelin, 2009) is characterised by the rivers draining into the "Marano Lagoon". The estimated outflow of the plain rivers was divided among the main lagoon outlets: Porto di Lignano, Zellina, Porto Buso, Canale di Morgo, La Fusa, and Bocca

di Primero. (Simoncelli et al, 2011). M. Pasaric et al., (2004) analyzed a time series of monthly mean river discharges along the Croatian coast and calculated the mean annual cycle of eleven rivers: Mirna, Rasa, Rjecina, Dubracina, Zrmanja, Krka, Jadro, Zrnovnica, Cetina, Neretva, and Ombla. According to the Albanian Hydrometeorological Institute, the main Albanian rivers discharging into the Adriatic Sea are: Buna-Bojana (into which the Drin river discharges as a consequence of landslides during the 19th century and the construction of hydropower plants along the river path), Mati, Ishmi, Erzeni, Shkumbini, Semani and Vjosa. Two other Albanian rivers, the Bistrica and Pavla, discharge into the Ionian Sea. Two Greek rivers discharging into the Ionian Sea, the Thyamis and Arachtos, were extracted from Global Runoff Data Centre, GRDC, datasets. Finally eleven Italian rivers discharging into the Ionian Sea were provided by several institutions (i.e. ARPAs, CNR IRPI, GRDC, and the Autorit di Bacino Basilicata).

2.2.3 Model validation with observations

The performance of the model was evaluated by comparing simulated fields with available in situ and satellite observations. We propose a comparison with temperature and salinity profiles collected by means of two Argo profiling floats for the last three years of the simulation. Figure 2.4 shows the trajectories of the Argo floats in the Adriatic and Northern Ionian Sea, respectively. Figure 2.5 shows vertical mean profiles of RMSE and BIAS for temperature and salinity.
On the whole, the EXP1 model output is in good agreement with the observed data, comparable RMSE and BIAS values were found for another, recent model of the Adriatic Sea (Guarnieri et al., 2013). In EXP2 without rivers, water masses in the Adriatic Sea appear saltier and warmer with respect to the observed dataset. Comparing observations with EXP2, RMSE and BIAS values were double those in EXP1, thus showing the impact of river runoff on the correct reproduction of the basin water mass characteristics. Analysed and modelled sea surface temperatures are shown in Figure 2.6. Analysed SST are obtained by Optimal Interpolation of SST measurements from daily AVHRR Pathfinder dataset. The

agreement between the modeled and observed datasets is high. The full dynamics Experiment, EXP1, fits Satellite SST better that EXP2: EXP1 $RMSE = 0.78°C$ and EXP2 $RMSE = 0.81°C$.

2.3 Is the Adriatic Sea an estuarine or anti-estuarine basin?

Traditionally, estuarine and anti-estuarine circulation has been classified on the basis of the net water flux at the surface only (Sverdrup, 1947; Pickard and Emery, 1990). Estuarine and anti-estuarine circulation is also linked to the cyclonic and anti-cyclonic overturning circulation which connects the marginal sea to the open ocean. Spall (2011, 2012) analysed a marginal sea overturning circulation predicting that the freshwater input could stop the anti-estuarine circulation and the anti-cyclonic MOC. Rahmstorf (1995) speculates that increasing freshwater inflow in the Northern Atlantic may potentially reduce or even shut down the overturning circulation. Cessi et al. (2014) show that both buoyancy forcing and wind stress work are connected to the strength of the circulation and thus, also to the MOC developing between the marginal sea and the open ocean.

Following Spall (2012) we assessed the non-dimensional thermal forcing parameter, μ/ϵ, and freshwater forcing parameter, γ/ϵ. The former describes the relative balance between heat budget in the interior basin and the lateral eddy fluxes that advect warm water into the basin and the latter describes the relative balance between freshwater budget in the interior basin and the lateral eddy fluxes advecting salty water. The lateral eddy fluxes detach from the cyclonic boundary current which comes from the open ocean and encircles the marginal sea. Small values of these parameters with eventually negative values of the freshwater parameter, indicate the lateral eddy fluxes prevail on the surface cooling of the interior basin due to the atmospheric forcing and may trigger the shutdown of deep convection.

We computed the two parameters over the whole simulation period and discovered that the thermal parameter is essentially the same in both experiments, $5 \cdot 10^{-5}$

in EXP2 and $4.9 \cdot 10^{-5}$ in EXP1, while the freshwater parameter is $7 \cdot 10^{-4}$ in EXP2 and $-2 \cdot 10^{-2}$ in EXP1 (see Appendix B for details on the computation of Spall's coefficients). This means that the Adriatic Sea runoff has the potential to shut down the deep convection.

Spall (2012) also shows that the ratio $\triangle S/\triangle T$, where $\triangle T$ and $\triangle S$ are the model-diagnosed temperature and salinity non-dimensional anomalies between the interior basin and the boundary current, can be written as a function of the thermal and freshwater forcing parameters (see Appendix B for details on the computation of these values). A ratio $\triangle S/\triangle T$ less than 1 means that the general circulation is in "thermal mode", which means the heat and freshwater balance in the interior basin oppose the lateral eddy fluxes and thus the deep convection is sustained by surface cyclonic boundary current and anti-cyclonic MOC. A ratio $\triangle S/\triangle T > 1$ indicates the "haline mode" of the marginal sea circulation with heat and freshwater balance of the interior basin favoring a cold and freshwater interior opposing the lateral eddy fluxes. This implies the shut down of deep convection and inversion of the MOC. The collapse of deep convection is demonstrated to be possible also in the thermal mode case if $\triangle S/\triangle T > 0.5$.

We obtain $\triangle T = 0.35$ and $\triangle S = 0.10$ in EXP1, while $\triangle T = 0.28$ and $\triangle S = 0.03$ in EXP2. These values give a ratio $\triangle S/\triangle T = 0.28$ and 0.12 in EXP1 and EXP2, respectively. Thus the Adriatic Sea is characterized by an anti-estuarine circulation with thermally driven deep water formation processes despite a large runoff budget. Even if we focus only on the year 2002, which was characterized by one of the largest river runoffs (Fig.2.3), $\triangle S/\triangle T = 0.42$ in EXP1 and 0.29 in EXP2, meaning that the Adriatic deep water formation and the anti-estuarine circulation characterize both experiments with and without river runoff, but in EXP1 we found $\triangle S/\triangle T$ closer to 0.5. Thus a strong river runoff has the potential to shutdown deep convection and reverse the overturning circulation of the marginal sea.

In order to further assess river influences on the MOC, an analysis of both buoyancy and wind stress forcing was performed. The surface buoyancy flux per unit

area, ($m^2 s^{-3}$), is expressed according to Cessi et al. (2014) as follows:

$$Q_b = \frac{g\alpha_T}{\rho_{0w} C_w} Q - \alpha_S S_0 g(E - P - \frac{R}{A}) \tag{2.3}$$

where $\alpha_{T,S}$ are the coefficients of thermal and haline expansion respectively, ρ_{0w} is the reference sea surface water density, Q is the net heat flux, C_w is the heat capacity of sea water, S_0 is the surface salinity. Finally, $(E-P-R/A)$ is the freshwater flux with evaporation rate, E, and precipitation rate, P, in ms^{-1}, river discharge, R in $m^3 s^{-1}$, and A representing the grid area of river mouths (m^2). Furthermore the following values were assumed: $\alpha_T = 2.3 \cdot 10^{-4} {}^\circ C^{-1}$, $\alpha_S = 7.5 \cdot 10^{-4} psu^{-1}$, $C_W = 3990 Jkg^{-1} {}^\circ C^{-1}$, $S_0 = 38.7 psu$ and $\rho_{0w} = 1029 kgm^{-3}$.
The net heat flux, Q, components are computed according to bulk formulae described in Appendix A.

First, we analyse the impact of R in the water flux contained in eq.2.3. Figure 2.7 shows the seasonal time series of the surface freshwater budget, (E-P-R/A), both for the whole computational domain (the Central Mediterranean Sea) and for the Adriatic Sea alone. We followed Artegiani et al. (1997) definition of a season: winter is from January to April, spring is May and June, summer from July to October, autumn corresponds to November and December. The whole Central Mediterranean Sea has a positive freshwater budget, 0.60 myr^{-1}, while it is negative over the Adriatic Sea, -0.69 myr^{-1}. Indeed our results highlight that the Central Mediterranean Sea is a concentration basin, while the Adriatic Sea is a dilution basin with river discharge playing a crucial role in the freshwater budget.

An annual time series of Adriatic surface buoyancy flux and wind work is shown in Figure 2.8. The realistic buoyancy flux (EXP1) is generally negative, implying a net anti-estuarine forcing of the circulation, however in certain years, the values can be several times smaller in absolute value than other years, and even change sign. This is the case for 2000, 2002 and 2008 where the buoyancy flux reached small or positive values. The small or positive buoyancy budget could weaken the anti-estuarine MOC in certain years, as we will see later. To note that 2001 to 2003 are the years characterized by the most relevant river role with respect to the other forcing mechanisms of the circulation (see green pointed line

in Fig.2.8), this is consistent with the lowest surface heat losses (not shown) and the minimum dense water volumes we found in these years (see Fig.2.11), in good agreement with findings of previous studies (Oddo and Guarnieri, 2011; Gunduz et al., 2013, Pinardi et al., 2015).

The wind work ($m^3 s^{-3}$) is defined as $\frac{\tau_w \cdot u_s}{\rho_0}$, where u_s is the sea surface velocity, ρ_0 is the reference sea surface water density and τ_w is the wind stress defined in Appendix A. In order to compare the wind work with the buoyancy flux, the wind work has been normalized by the basin volume.

Figure 2.8 shows that the wind work is always positive (10^{-8} $m^2 s^{-3}$), implying a net source of mechanical energy for the Adriatic Sea and it is one order of magnitude larger than the buoyancy flux (10^{-9} $m^2 s^{-3}$) in the realistic experiment with rivers. Thus considering the two major forcings of the circulation, the Adriatic Sea results again to be an anti-estuarine basin characterized by a large wind work energy source.

The buoyancy flux of the Adriatic Sea represent an energy sink if positive, and thus tends to counterbalance the energy source due to wind work giving rise to a low kinetic energy basin circulation. This is consistent with the weaker anti-estuarine MOC and the more stagnant circulation below the Otranto sill depth (both in SAd Pit and Ionian abyss) we found out in EXP1, especially in 2002, as detailed in the next section.

2.4 How is the intensity of Central Mediterranean MOC affected by runoff?

In order to better quantify the river influence on the Central Mediterranean MOC, an inter-annual analysis of the meridional transport stream function was carried out. The literature contains ample evidence that the ocean MOC is primarily driven by wind and tidal stirring (Munk et al., 1998; Paparella et al., 2002; Marshall et al., 2012). In addition, the relationship between the dense water formation, driven by the buoyancy flux, and the strength of the overturning circulation has been highlighted in several theoretical, as well as realistic modelling

studies (Rahmstorf, 1995; Rahmstorf, 1996; Pisacane et al., 2006). Similarly, here we focus on the downwelling branch of the Central Mediterranean MOC, which develops inside the Southern Adriatic sub-basin due to the local open-ocean convection and dense water formation sustained by winter heat losses and a permanent cyclonic gyres driven by wind stress curl.

The meridional transport stream-function, Ψ, is defined as (Pedlosky, 1987):

$$\Psi(y,z) = -\int_{x_0}^{x_1}\int_{-H}^{z} \overline{v(x,y,z)}dxdz \tag{2.4}$$

with $-H < z < 0$ as the depth, x_0 and x_1 the more eastern and more western sea points, $\overline{v}$ is the time-averaged meridional velocity. The velocity field is tangent to the isopleths of Ψ, and positive Ψ values indicate anti-estuarine cells turning anti-cyclonically, while negative values indicate estuarine cells turning cyclonically.

Figure 2.9 shows the transport stream-function for EXP1 and EXP2, averaged over the whole simulation period. A large anti-estuarine cell down to a 700-800 m depth is detected in both experiments in the Northern Ionian Sea and SAd sub-region, but with different intensities. Interestingly enough many estuarine cells exists in the domain: one at the surface in the NAd, one in the deep layers of the Southern Adriatic Pit around 41-42°N, SAP, another in the Middle Adriatic Pit around 43°N, MAP, and the last in the Northern Ionian abyss.

Fig.2.9 demonstrates that, even with a realistic representation of the river runoff, the anti-estuarine character of the Central Mediterranean MOC is maintained. Indeed, in EXP1, the secondary estuarine cells of the NAd, MAd, SAd sub-regions and Northern Ionian basin are larger than in EXP2, however the anti-estuarine MOC cell still dominates.

The estuarine component of the MOC may become more evident on a seasonal basis, particularly during summer. Figure 2.10 focuses on summer 2002 and summer 2009 because these years had the largest river discharge (Fig. 2.3). In summer 2009 (Fig. 2.10 bottom panels), a well-defined surface estuarine cell characterizes the whole meridional extension of the basin with no differences between EXP1 and EXP2, which means that the wind forcing becomes a dominant contribution to the estuarine secondary cells. During this season the wind work is

maximum (Fig. 2.8 bottom panel) but the buoyancy flux is still negative (Fig.2.8 top panel) thus maintaining an anti-estuarine MOC in the Adriatic Sea. In summer 2002 (Fig. 2.10 top panels), the river influence is more significant probably due to the weaker wind forcing and the positive buoyancy forcing. In EXP1 the anti-estuarine character of the MOC is weak and restricted to 200-400 m depths, while the secondary estuarine cells are stronger. However even in this case the dominant overturning circulation is still anti-estuarine, in agreement with the Spall's (2012) freshwater and thermal forcing parameters predictions.
We conclude that the Central Mediterranean anti-estuarine MOC is a stable configuration of the local meridional overtuning circulation driven by winds and by highly variable buoyancy forcings. River runoff can affect MOC strength, thus enhancing the amplitude of the secondary estuarine cells and reducing the intensity of the large anti-estuarine cell but the anti-estuarine MOC remains the largest overturning, anti-estuarine structure of the Central Mediterranean Sea.

2.5 How do rivers influence the formation of dense water in the Adriatic Sea?

The aim here is to establish how rivers impact the dense water formation processes in the Southern Adriatic Sea and thus impact the MOC.
Figure 2.11 shows the dense water volume formed in the SAd computed as the water volume with larger potential density anomaly than the threshold value, 29.2 kgm^{-3}. EXP1 results are in agreement with previous model findings (Oddo and Guarnieri, 2011; Gunduz et al., 2013, Pinardi et al., 2015). The greatest dense water volume was formed in 2006 and 2012, while minimum dense water volumes were found in 2001 to 2003 owing to a relative high buoyancy flux (with the concomitant effect of strong river runoff and weak heat losses) and low wind work.. The dense water rate ranges from 0.03 Sv in 2001 to 1.53 Sv in 2006 and the mean annual SAd dense water rate is 0.3 Sv, a value corresponding to several previous studies (Artegiani et al., 1989 and 1997; Lascaratos, 1993; Cushman-

Roisin et al., 2002; Curchitser et al., 2001; Manca et al., 2002; Mantziafou et al., 2004 and 2008). EXP2, without river forcing, shows 20-30% larger dense water volumes than in EXP1. To explain the river impact on the open sea convection, Figure 2.12 shows seasonal $\Theta - S$ diagrams in three Adriatic sub-region zonal sections for winter 2009. In this period river runoff determines a large stratification of the water column with respect to the no-river case and the dense water mass volume formation decreases by almost 30%.

Previous studies suggest that rivers affect SAd dense water volumes because they reduce the lateral advection of NAd dense waters which are known to flow along the western shelf and slide down into the Southern Adriatic Pit near the Bari canyon (Mantziafou et al., 2004; Wang et al., 2007; Mantziafou et al., 2008). However, in our case this is not sufficient to account for the difference between the SAd dense water volumes in EXP1 and EXP2 because this difference is larger than the sum of NAd and MAd dense water volume differences.

The preconditioning factors of open-sea convection and dense water formation in the Southern Adriatic are known to be the permanent cyclonic gyre sustained by wind stress curl, the surface winter cooling and the inflow of LIW through the Otranto Strait.

Thus we conclude that river runoff primarily influences the dense water formation processes by changing the SAd vertical stratification characteristics. However these stratification changes can determine changes in the MOC characteristics only if the concomitant buoyancy forcing is positive, as shown for the 2002 case. In the 2009 case, wind stress work is large and buoyancy forcing still negative, thus balancing the large river runoff stratification effects and producing no relevant changes in the MOC.

2.6 How do rivers influence the volume of Adriatic dense water that spreads into the Northern Ionian Sea?

The Adriatic dense waters outflow through the Otranto Strait into the abyssal Ionian Sea, generally occupying the layer below the dense waters coming from the Cretan Sea and the Levantine basin (Roussenov et al., 2001; Bensi et al., 2013, Curchitser et al., 2001).

Figure reffg12 shows the seasonal potential density anomaly of the 200m layer above the seabed in both EXP1 and EXP2 and their differences with a zoom on the Ionian Sea. The maps show spring 2012 because this was the year with one of the greatest dense water volumes (Figure 2.11).

SAd dense water initially spreads into the Northern Ionian Sea following the topography and then tends to sink to the bottom of the Ionian basin due to friction and turbulent mixing thereby creating a nearly homogeneous layer below 1200m (Curchitser et al., 2001). It is well known that newly formed Adriatic dense waters fill the Ionian abyss in two-three years (Wu et al., 1996; Bensi et al., 2013). Figure 2.13 shows that the bottom boundary current forced by dense water outflow from the Otranto Strait is characterized by less dense waters that intrude offshore in EXP1 across the isobaths in the Northern Ionian open ocean area. In EXP2, the Adriatic dense water outflow is limited to a narrow band against the Italian shelf. This suggests that river runoff will have consequences on the Northern Ionian Sea water mass structure and mixing processes.

2.7 Summary, conclusions and future developments

This study enabled us to investigate the influence of river freshwater inflow on the circulation and dynamics of the Central Mediterranean Sea.

Two twin experiments, with and without river inflow, were carried out from the beginning of 1999 to the end of 2012 covering the whole Central Mediterranean

Sea with a complete distribution of rivers in the Adriatic and Ionian catchment areas.

ARGO data were used in support of numerical findings. They confirm that rivers are necessary to correctly reproduce the observed water mass characteristics and show that results of the model are in good agreement with observations in a realistic runoff regime.

We first studied the role of rivers on the estuarine/anti-estuarine character of the Adriatic Sea. The model results indicate that the Adriatic Sea is an anti-estuarine basin even when a strong river runoff occurs. The computation of Spall (2012) thermal and freshwater forcing parameters in both experiments demonstrates that river runoff cannot reverse the dominant anti-estuarine character of Adriatic circulation or shut down the deep convection in the basin interior. The inter-annual analysis of buoyancy and wind stress forcings confirms that although the Adriatic buoyancy budget is positive in years with a large river runoff, the anti-estuarine character of the Adriatic circulation is persistent and mainly driven by wind work and heat losses.

We analysed the meridional transport stream function in the Central Mediterranean Sea and detected a permanent anti-estuarine anti-cyclonic meridional overturning cell, occupying the Southern Adriatic and the open Ionian Sea, plus secondary estuarine cells in the NAd and in the SAd, MAd deep layers as well as in the Northern Ionian abyss. A key result is that the Central Mediterranean MOC is largely wind driven but large and anomalous river runoff can affect its strength, enhancing the amplitude of the secondary estuarine cells and reducing the intensity of the dominant anti-estuarine cell. We focused on the downwelling branch of the Central Mediterranean MOC, which develops in the Adriatic basin due to dense water formation processes. Rivers were demonstrated to affect the Adriatic dense water volumes. Previous studies showed that rivers reduce the dense water formation in the Northern sub-region where most discharge is located. Here we show that rivers also directly affect the vertical mixing processes in the Southern Adriatic sub-region by changing the water column stratification in the SAd and thus decreasing the dense water volumes. Finally we showed that the Adriatic dense waters overflowing the Otranto Strait are less dense in a

realistic runoff regime, thus implying a stronger turbulent mixing with the Ionian abyssal waters and a higher offshore spreading.

Future investigations will point to an advanced implementation of river discharge accounting for the ocean water entering river outlets and the exchange flow into the estuary areas. This would allow to force the ocean model in a more realistic way. In this work values of salinity at the river mouths were largely decided on an ad hoc basis. In addition better resolved wind forcing should be considered because of its importance in determining the local MOC strength.

The presented study focused on river role on the interannual-dynamics of the Central Mediterranean sub-basin which holds an antiestuarine overturning circulation cell and gets most of river release into the Mediterranean basin. However the question of teleconnections among the mediterranean sub-basins could be studied in deep to weigh river role with respect to the other forcings of the whole Mediterranean circulation, expecially for what regards the spreading of the Levantine Intermediate Waters toward the Central Mediterranean Sea. Thus we plan to perform a new twin experiment extending the model configuration to the whole Mediterranean Sea and prolonge it up to $50yr$ in order to capture the multi-decadal natural variability of the Mediterranean Sea.

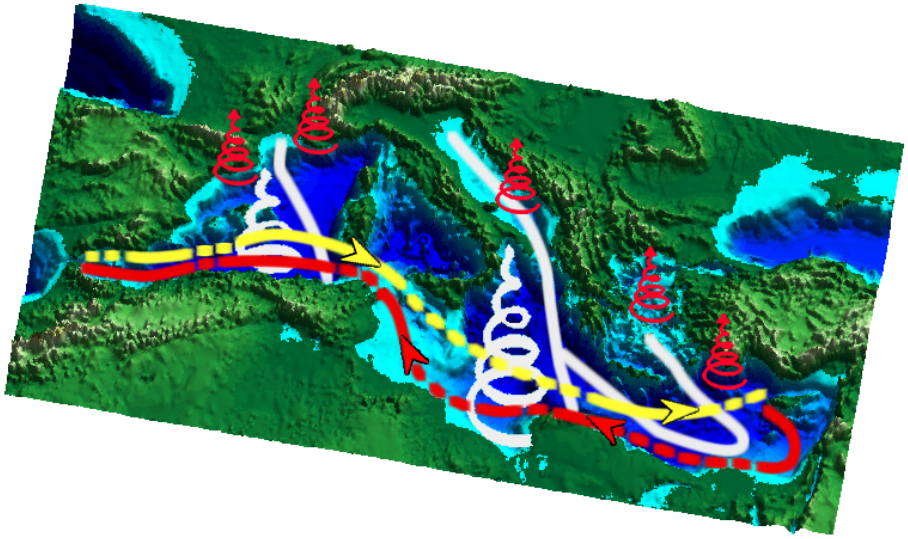

Figure 2.1: The conveyor belts of the Mediterranean Sea. The red and yellow dashed streamlines in the zonal direction stand for the zonal overturning circulation in the surface-intermediate layers that is forced by the Gibraltar stream flow and Levantine Intermediate Water (LIW) formation processes. The red spirals indicate the preferential sites for strong heat losses during wintertime and dense water formation processes. Two anti-cyclonic meridional overturning circulation patterns can be distinguished (white spirals): the Western Mediterranean MOC originating in the Gulf of Lion, and the Central Mediterranean MOC originating in the Adriatic Sea (reproduced from Pinardi et al., 2006)

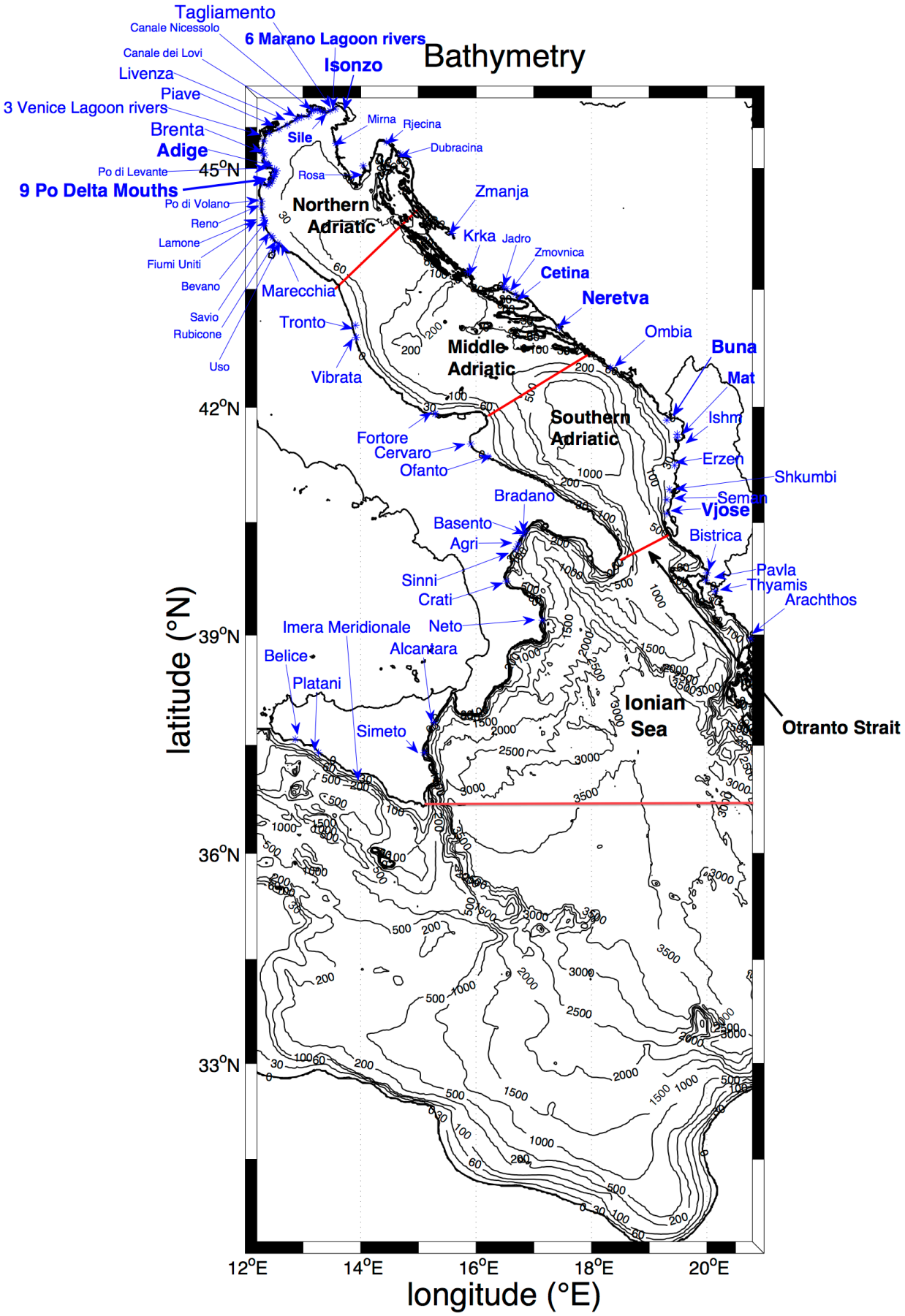

Figure 2.2: Model domain and details on areas of interest. The red lines define the three Adriatic sub-regions and the Ionian Sea. Black isolines show the bathymetry. Blue stars and arrows indicate the model river mouths

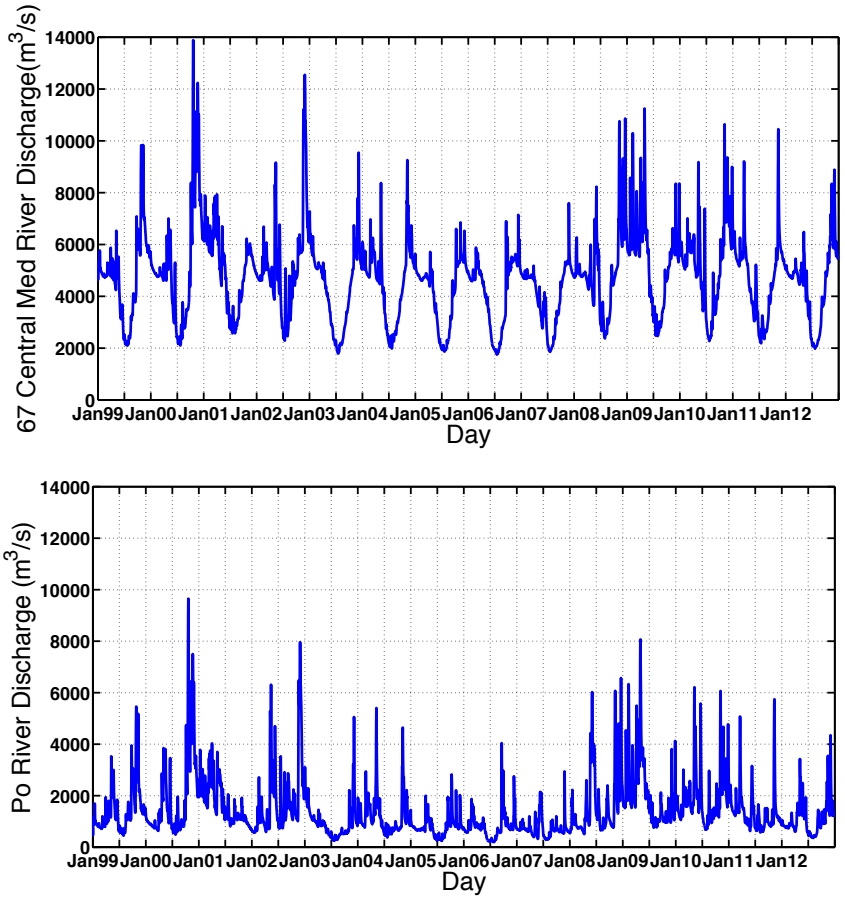

Figure 2.3: Top Panel: Daily Time Series of total river discharge during the entire simulation period, 1999-01-01 to 2012-12-31. Bottom Panel: Focus on Po river discharge based on observations

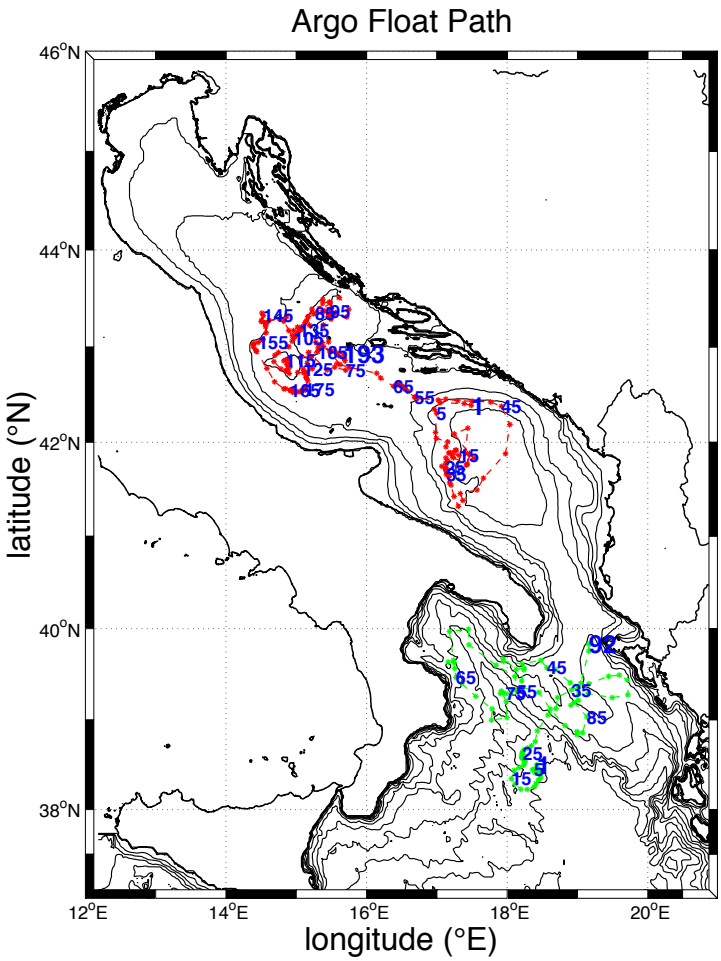

Figure 2.4: The trajectory of two Argo profiling floats over 2010-2012. Numbers indicate the ascending profiles: 193 into the Adriatic Sea and 92 into the Ionian Sea

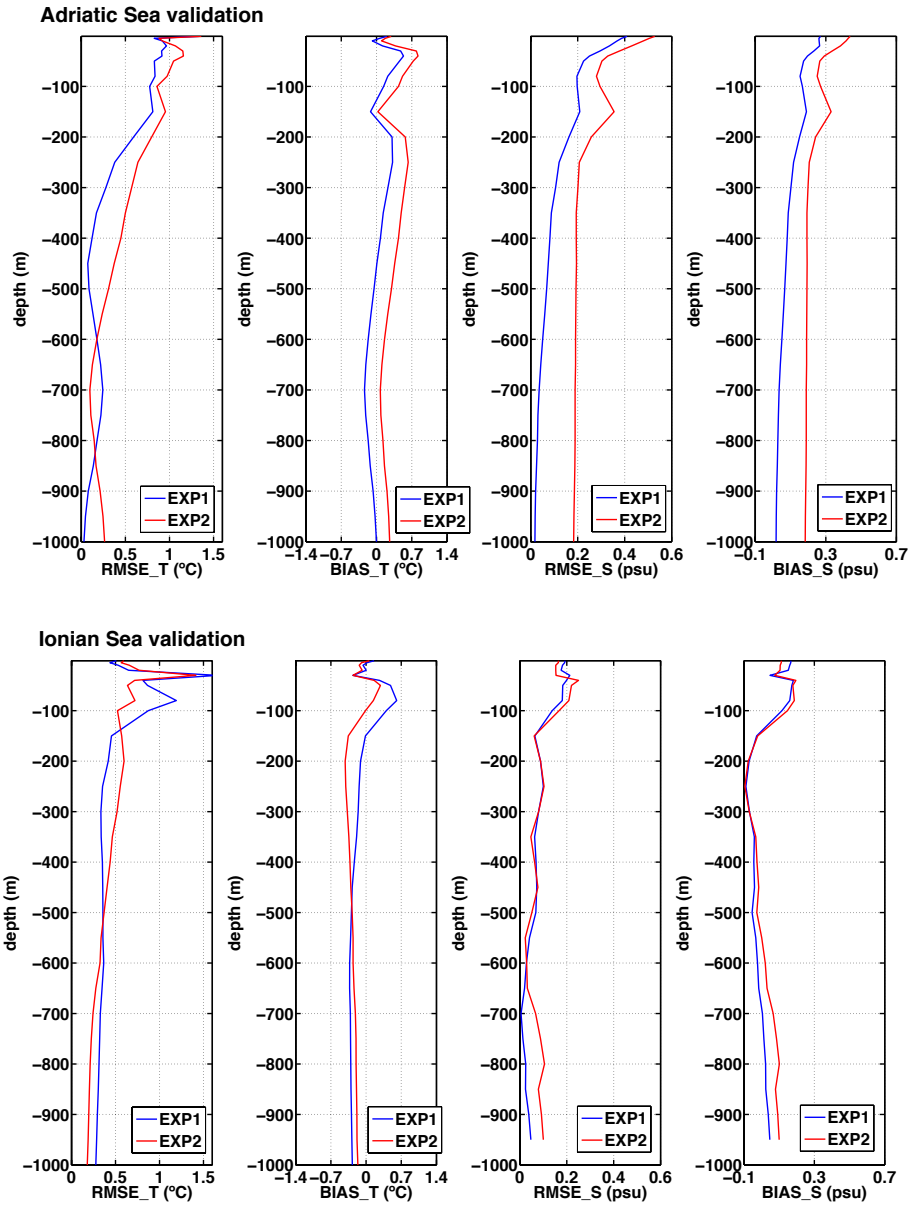

Figure 2.5: Temperature and Salinity RMSE and BIAS for the available Argo observations over 2010-2012 in EXP1 and EXP2

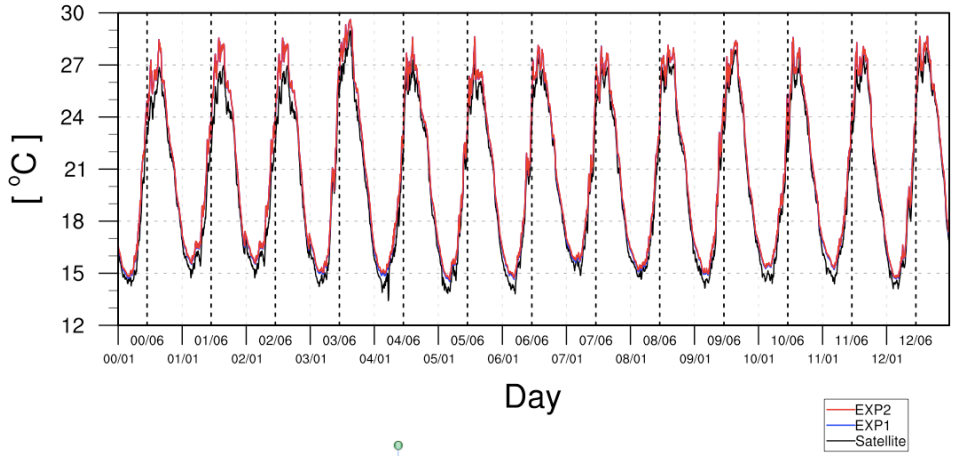

Figure 2.6: Monthly time series of satellite (black line) and modelled (red line for EXP2 and blue line for EXP1) Sea Surface Temperature. $EXP1 \quad RMSE = 0.78°C$, $EXP2 \quad RMSE = 0.81°C$

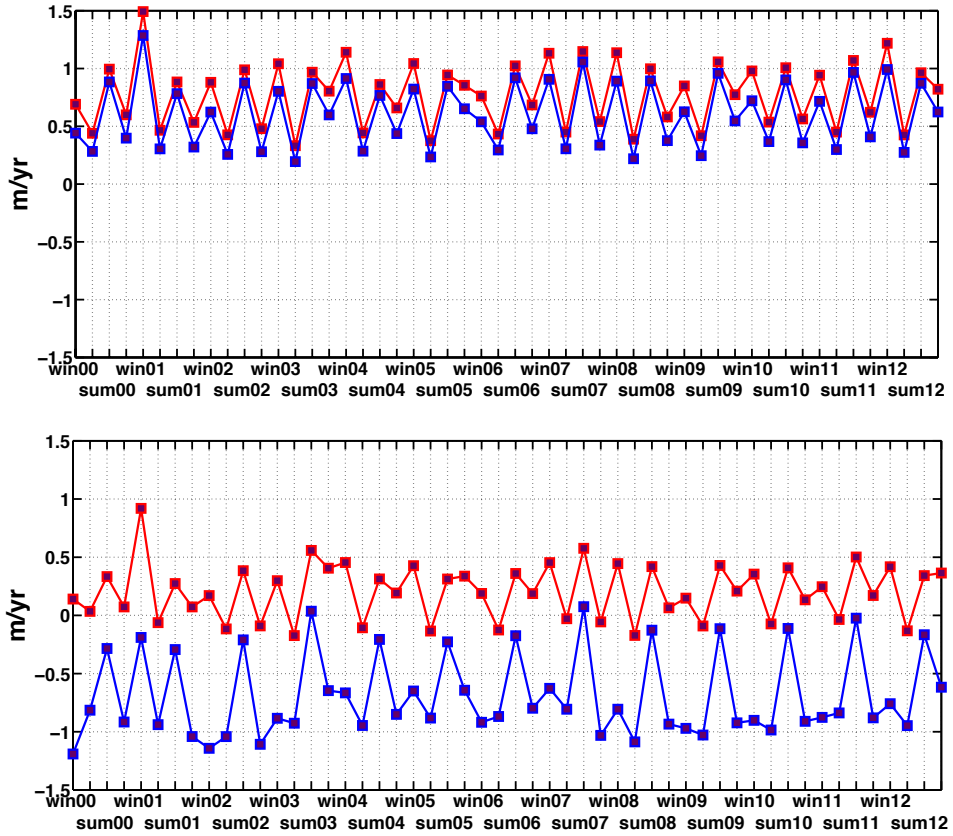

Figure 2.7: Seasonal time series of the surface freshwater budget respectively for the entire computational domain (top), and the Adriatic Sea only (bottom). The red lines are for the freshwater budget $(E - P)$ in EXP2, while the blue ones are for $(E - P - R/A)$ in EXP1

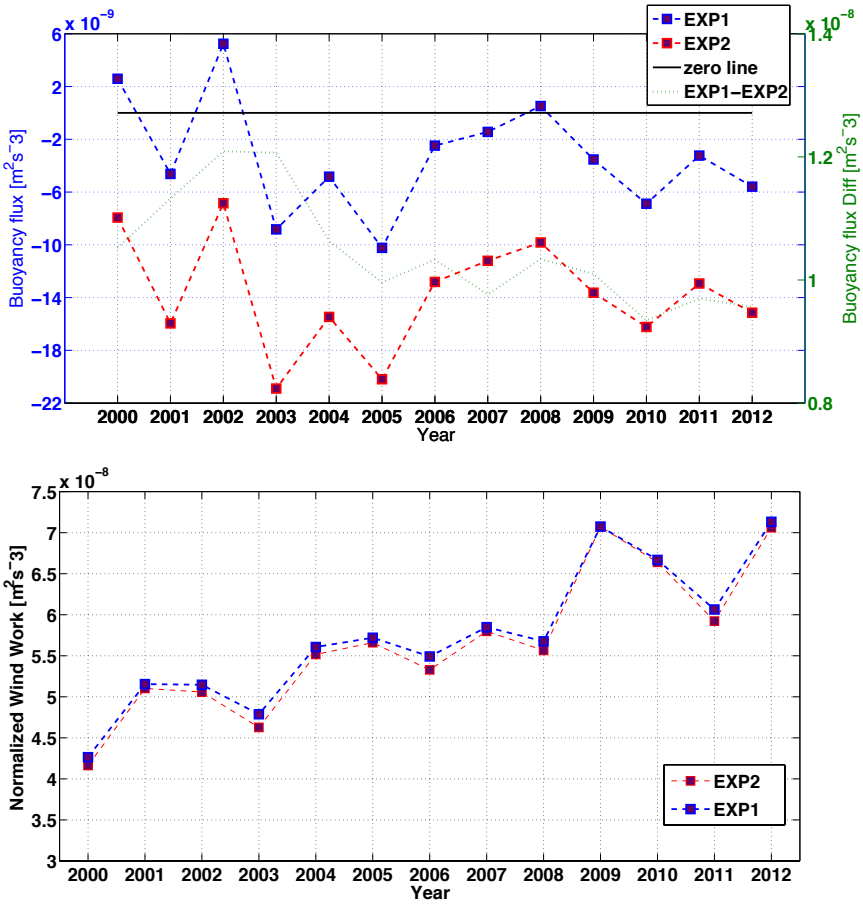

Figure 2.8: Top panel: Annual time series of buoyancy flux, $\int\int Q_b dA/A$, for EXP1 and EXP2 and the relative difference. Bottom Panel: Annual time series of normalised averaged wind work, $\frac{1}{\rho_0}\int\int \frac{\tau \cdot u_s dA}{V}$, for EXP1 and EXP2. Results are only relevant to the Adriatic Sea

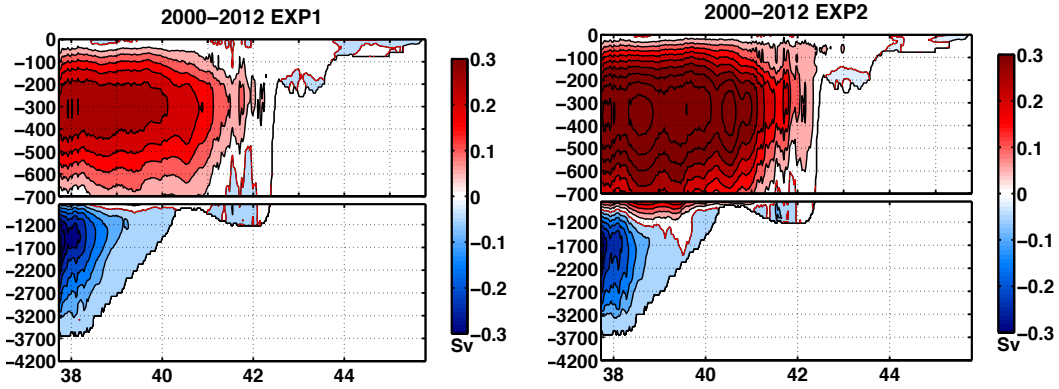

Figure 2.9: Multi-annual Meridional Transport Stream Function for the Central Mediterranean Sea

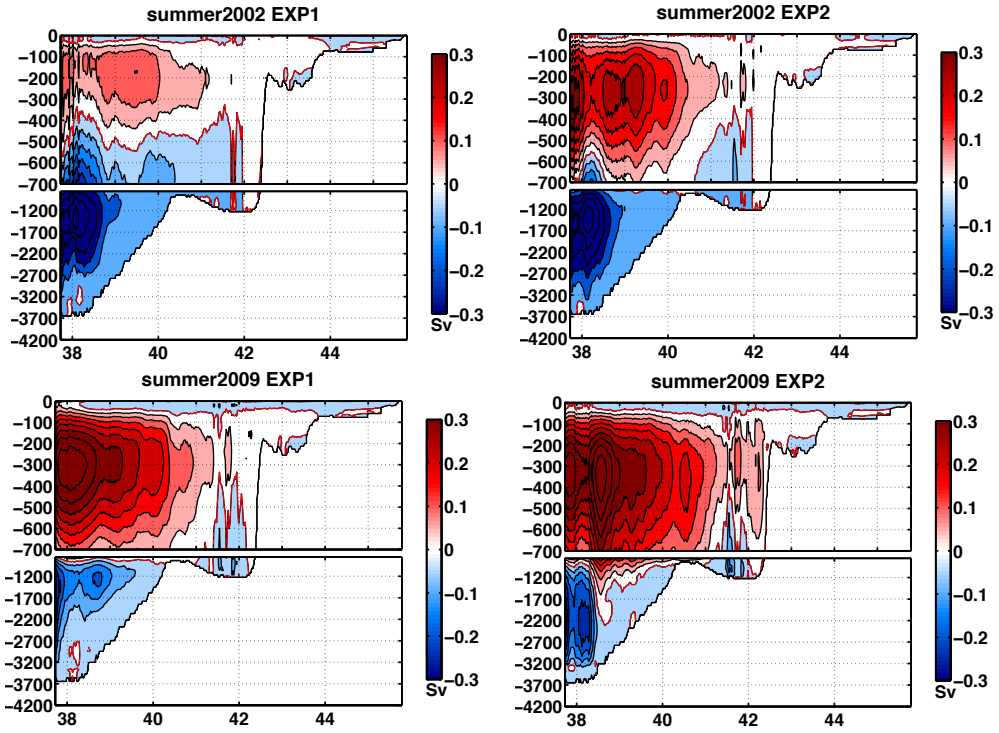

Figure 2.10: Summer 2002 (Top Panel) and Summer 2009 (Bottom Panel) Meridional Transport Stream Function for the Central Mediterranean Sea

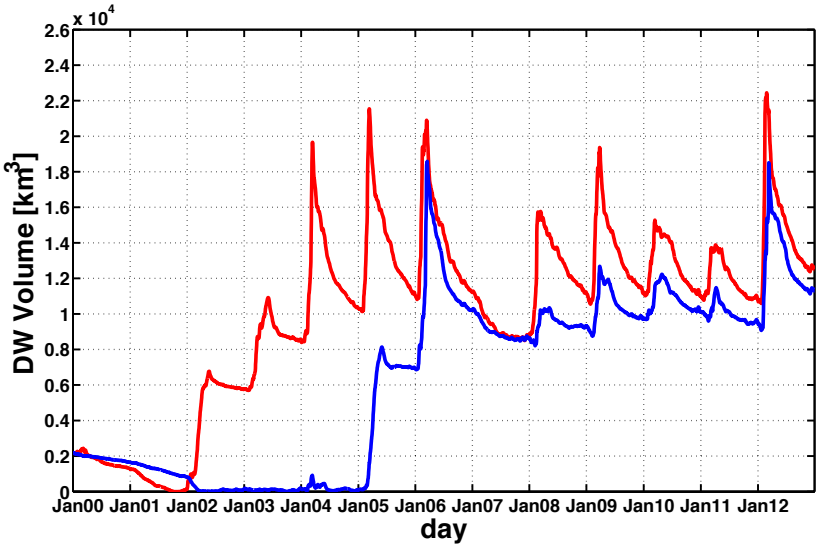

Figure 2.11: Daily averaged time series of water volumes with $\sigma_\theta > 29.2 kgm^{-3}$ in the SAd sub-region. The blue line stands for EXP1, the red line for EXP2

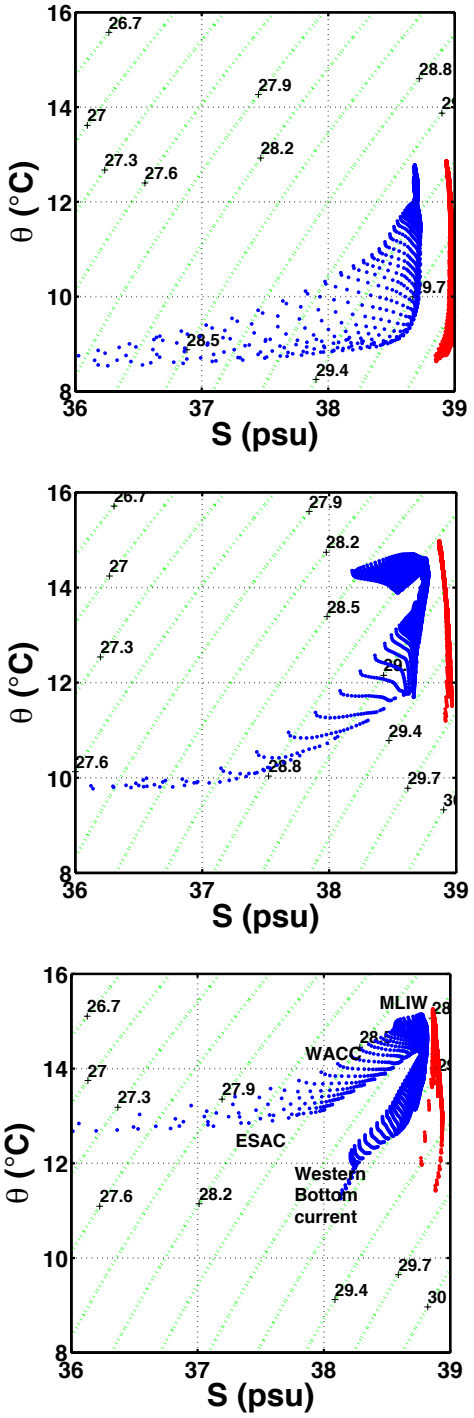

Figure 2.12: $\Theta - S$ diagram in winter 2009 for EXP1 (blue dots) and EXP2 (red dots) in three zonal sections related to NAd sub-region at 44.38N (top panel), MAd at 42.6°N (middle panel) and SAd at 41.61°N (bottom panel), respectively. The Western Adriatic Coastal Current, WACC, the Eastern Southern Adriatic Current, ESAC, the Western bottom current and the Modified Levantine Intermediate Water, MLIW, are marked in the bottom panel according to the known range of temperatures and salinities

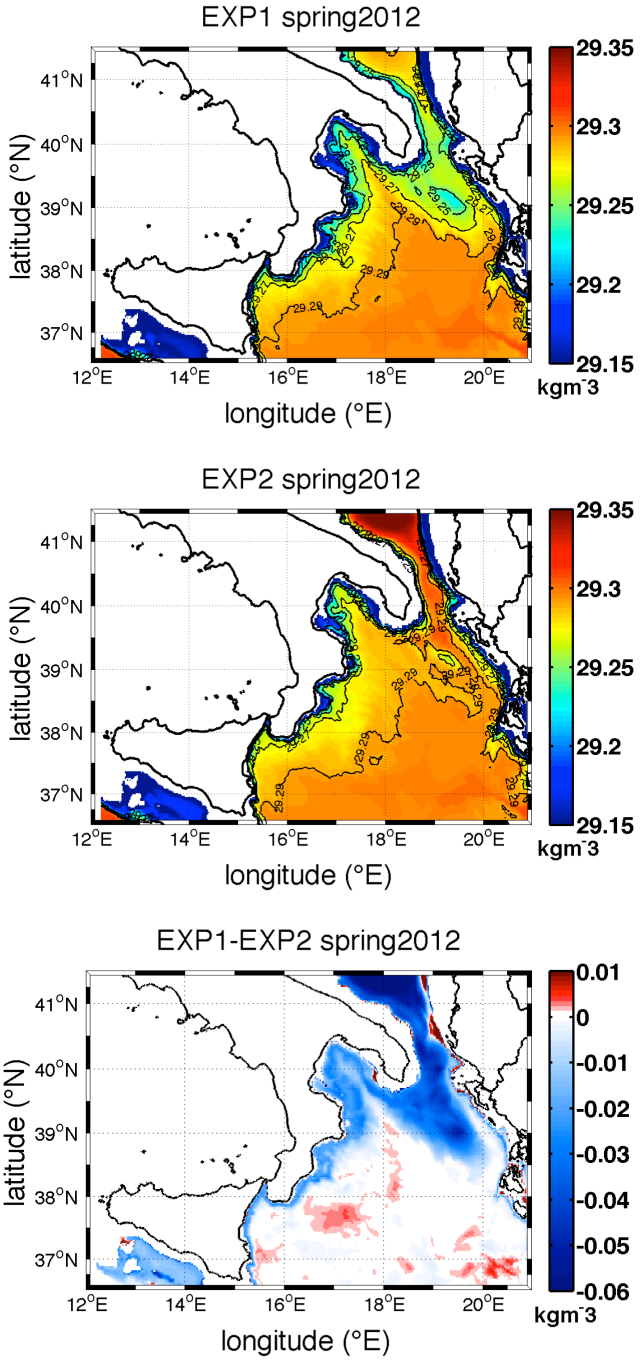

Figure 2.13: Seasonal potential density anomaly on a 200m layer above seabed and difference between EXP1 and EXP2 with zoom on the Ionian Sea

River	Dataset	Reference Period	Discharge Basin	Mean Annual Discharge (m^3s^{-1})
Adige (Italy)	GRDC	1922-1984	Adriatic Sea	223.75
Agri (Italy)	Autorita' di bacino	n.r.	Ionian Sea	9.14
Alcantara (Italy)	Piano Tutela Acque Sicilia	1980-1997	Ionian Sea	4.7
Arachthos (Greece)	GRDC	1964-1980	Ionian Sea	19.73
Basento (Italy)	CNR IRPI	1933-1971	Ionian Sea	13.23
Belice (Italy)	Piano Tutela Acque Sicilia	1980-2000	Ionian Sea	51.57
Bevano (Italy)	ARPA EMR	n.r.	Adriatic Sea	6
Bistrica (Albania)	Albanian Hydrometeorological Institute	1949-1987	Ionian Sea	32.1
Bocca di Primero (Italy)	ARPA VENETO	n.r.	Adriatic Sea	10.28
Bradano (Italy)	CNR IRPI	1929-1971	Ionian Sea	5.85
Brenta (Italy)	ARPA VENETO	n.r.	Adriatic Sea	93.17
Buna/Bojana(Albania-Montenegro)	Albanian Hydrometeorological Institute	1965-1985	Adriatic Sea	675
Canale dei Lovi (Italy)	ARPA VENETO	n.r.	Adriatic Sea	22.7
Canale di Morgo (Italy)	ARPA VENETO	n.r.	Adriatic Sea	10.28
Canale Nicessolo (Italy)	ARPA VENETO	n.r.	Adriatic Sea	22.7
Cervaro (Italy)	Raicich (1996)	n.r.	Adriatic Sea	2.92
Cetina (Croatia)	Pasaric et al (2004)	1947-2000	Adriatic Sea	88.28
Crati (Italy)	CNR IRPI	1926-1966	Ionian Sea	26.2
Dubracina (Croatia)	Pasaric et al (2004)	1947-2000	Adriatic Sea	4.14
Erzen (Albania)	Albanian Hydrometeorological Institute	1949-1992	Adriatic Sea	16.9
Fiumi Uniti (Italy)	ARPA EMR	n.r.	Adriatic Sea	12.06
Fortore (Italy)	Raicich (1996)	n.r.	Adriatic Sea	12.25
Imera Meridionale (Italy)	GRDC	1978-1980	Ionian Sea	4.26
Ishm (Albania)	Albanian Hydrometeorological Institute	1968-1992	Adriatic Sea	19.8
Isonzo (Italy)	Malacic e Petelin (2009)	1945-2000	Adriatic Sea	110.43
Jadro (Croatia)	Pasaric et al (2004)	1947-2000	Adriatic Sea	7.18
Krka (Croatia)	Pasaric et al (2004)	1947-2000	Adriatic Sea	56.51
La Fosa (Italy)	ARPA VENETO	n.r.	Adriatic Sea	10.28
Lamone (Italy)	ARPA EMR	n.r.	Adriatic Sea	12.06
Livenza (Italy)	ARPA VENETO	n.r.	Adriatic Sea	88.33
Marecchia to Tronto, Tronto excluded (Italy)	Raicich (1996)	1956-1965	Adriatic Sea	121.92
Mat (Albania)	Albanian Hydrometeorological Institute	1951-1986	Adriatic Sea	87.4
Mirna (Croatia)	Pasaric et al (2004)	1947-2000	Adriatic Sea	7.91
Neretva (Croatia)	Pasaric et al (2004)	1947-2000	Adriatic Sea	366.86
Neto (Italy)	ARPA CAL	n.r.	Ionian Sea	6.22
Ofanto (Italy)	Raicich (1996)	n.r.	Adriatic Sea	14.92
Ombla (Croatia)	Pasaric et al (2004)	1947-2000	Adriatic Sea	27
Pavla (Albania)	Albanian Hydrometeorological Institute	1951-1991	Ionian Sea	6.69
Piave (Italy)	ARPA VENETO	n.r.	Adriatic Sea	54.33
Platani (Italy)	GRDC	1978-1980	Ionian Sea	2.37
Po di Levante (Italy)	ARPA EMR	n.r.	Adriatic Sea	21.67
Po di Volano (Italy)	ARPA EMR	n.r.	Adriatic Sea	6
Pto Buso (Italy)	ARPA VENETO	n.r.	Adriatic Sea	10.28
Pto di Chioggia (Italy)	ARPA VENETO	n.r.	Adriatic Sea	17.27
Pto di Lido (Italy)	ARPA VENETO	n.r.	Adriatic Sea	17.27
Pto di Malamocco (Italy)	ARPA VENETO	n.r.	Adriatic Sea	17.27
Pto Lignano (Italy)	ARPA VENETO	n.r.	Adriatic Sea	10.28
Rasa (Croatia)	Pasaric et al (2004)	1947-2000	Adriatic Sea	1.58
Reno (Italy)	ARPA EMR	n.r.	Adriatic Sea	49.33
Rjecina (Croatia)	Pasaric et al (2004)	1947-2000	Adriatic Sea	7.22
Rubicone (Italy)	ARPA EMR	n.r.	Adriatic Sea	6
Savio (Italy)	ARPA EMR	n.r.	Adriatic Sea	12.06
Seman (Albania)	Albanian Hydrometeorological Institute	1948-1987	Adriatic Sea	86
Shkumbi (Albania)	Albanian Hydrometeorological Institute	1948-1991	Adriatic Sea	58.7
Sile (Italy)	ARPA VENETO	n.r.	Adriatic Sea	52.92
Simeto (Italy)	GRDC	1978-1980	Ionian Sea	3.31
Sinni (Italy)	CNR IRPI	1937-1976	Ionian Sea	20.58
Tagliamento (Italy)	ARPA VENETO	n.r.	Adriatic Sea	96.92
Thyamis (Greece)	GRDC	1963-1978	Ionian Sea	51.39
Tronto (Italy)	Raicich (1996)	1956-1965	Adriatic Sea	17.92
Uso (Italy)	ARPA EMR	n.r.	Adriatic Sea	6
Vibrata to Fortore+Pescara+Sangro +Trigno+Biferno (Italy)	Raicich (1996)	1956-1965	Adriatic Sea	190
Vjiose (Albania)	Albanian Hydrometeorological Institute	1948-1987	Adriatic Sea	189
Zellina (Italy)	ARPA VENETO	n.r.	Adriatic Sea	10.28
Zrmanja (Croatia)	Pasaric et al (2004)	1947-2000	Adriatic Sea	40.10
Zrnovnica (Croatia)	Pasaric et al (2004)	1947-2000	Adriatic Sea	1.76

Table 2.1: River runoff climatological values adopted for the Adriatic and Ionian rivers, time period for the climatologies and mean annual discharge values. Some of the datasets consist of observations taken at hydrometric stations and some are estimated values. To note that Po di Levante and Po di Volano are point sources different from the 9 branches of the Po delta. Po river runoff values are not included in this Table since daily averaged observations are assumed at each branch of the delta

Parameter	EXP1	EXP2
μ/ϵ	$5 * 10^{-5}$	$4.9 * 10^{-5}$
γ/ϵ	$-2 * 10^{-2}$	$+7 * 10^{-4}$
$\triangle T$	0.35	0.28
$\triangle S$	0.10	0.03
$\triangle S/\triangle T$	0.28	0.12

Table 2.2: Summary of the key parameters of the Twin Experiment. The model-diagnosed quantities are the thermal forcing parameter μ/ϵ, the freshwater forcing parameter γ/ϵ, the temperature anomaly of the convective water mass $\triangle T$ and the salinity anomaly of the convective water mass $\triangle S$

3 The local water cycle of river catchments. Modeling the meteorological and hydrological processes

Preamble

This chapter is a co-authored paper with N. Pinardi, J. Tribbia, D. Gochis, A. Navarra, G. Coppini, T. Vukicevic, and D. Shea, entitled "A meteo-hydrological modeling study for flood events in the Ofanto river catchment" and submitted to the Natural Hazards and Earth System Sciences.

A meteo-hydrological modelling system has been set up over the Central Mediterranean Sea with a focus on the Ofanto river catchment, and we evaluate the capability of this integrated system to simulate the local water cycle.

The modeling chain consists of the mesoscale meteorological model Weather Research and Forecasting WRF (Skamarock et al., 2008), the Land Surface Model NOAH-MP (Niu et al., 2011) and the hydrological model WRF-Hydro (Gochis et al., 2013). NOAH-MP is coupled in two-way mode with WRF and WRF-Hydro.

Two simulations have been carried out over winter 2011 and autumn 2013. The final goal is a reliable meteo-hydrological reconstruction of the severe historical events which hit the Southern Italy during the selected time ranges with heavy rainfall and flooding of the river.

Several sensitivity tests have been performed and we assess which tunable parameters, numerical choices and forcing data most impact the model performance. The simulated precipitation has been validated by comparison with raingauge stations in the Ofanto basin and corrected by a simple method of successive corrections. WRF capability to reproduce heavy rain events is sensitive to the initialisation time and we found that a spin-up of about 1.5 days is needed. The Ofanto hydrograph is correctly reproduced by the model, and the simulated runoff errors are shown by comparison with Cafiero station observations.

The calibration points out that two parameters should be set carefully: the

infiltration coefficient should be treated as seasonally dependent and the aquifer discharge coefficients as soil type dependent.

3.1 Introduction

Severe weather events associated with heavy rainfall and river floods have increased during the last decades in many regions around the world including the Mediterranean area (Barredo, 2007). Moreover longterm projections show intensity and occurrence of extreme events are expected to grow (Groisman et al., 2004 and 2005). Thus the meteo-hydrological short term forecasts are expected to be released with sufficient accuracy for warning purposes and long term predictions are required for management and resilience activities.

For these reasons the scientific community started to dedicate a great effort for increasing the performance of high resolution meteorological and hydrological models as well as coupling them.

Modeling the spatial and temporal distribution of the water cycle is a challenge because water cycle includes several processes which span a wide range of spatial and temporal scales and interact each other.

Most meteorological and climatological models still represent the surface and subsurface processes of the water cycle in a oversimplified way, just using a land surface sub-model which represents the soil processes on a 1-dimensional column. The added value of the hydrological modeling is the capability to laterally route both the surface and subsurface water flows and to describe how they interact each other. Hydrology modelling covers a huge variety of approaches: from simple empirical models to more complex wave systems (i.e. kinematic, diffusive and dynamic wave models).

As far as we know the HYdrology surface runoff PROgnostic Model,HYPROM (Nickovic et al., 2010), is currently the only hydrological modeling system with fully prognostic equations for the overland water flow but it doesn't represent the subsurface physical processes as the groundwater drainage, the saturated subsurface water flow and the aquifer water storage. In this study we use the

WRF-Hydro system (Gochis et al., 2013) which is based on a diffusive wave approximation for representing both the overland water flow and the river streamflow. Moreover it solves the subsurface soil physics and is 2-way coupled with NOAH-MP (Niu et al., 2011) land surface model.

The quality of meteo-hydrological modelling is still a demanding issue. Precipitation forecasting is one of the most critical task for meteorological mesoscale models since the precipitation field is the end result of many multi-scales and interacting processes and is sensitive to topography, soil types and land use conditions. The grid spacing of mesoscale meteorological models is in the range of "gray-zone" (Moeng et al., 2007; Shin et al., 2013) resolutions for convection, where the power spectrum of the turbulence reaches its peak and thus the convective motions and the precipitation are only partially resolved. The quality of meteorological modelling is then critical for ensuring the quality of hydrological modelling as the uncertainties associated with the meteorological simulations propagate into the hydrological models (Pappenberger et al., 2005). An additional source of uncertainties is due to the parameterisation of many physical processes involved in the water cycle (e.g. the water infiltration through the soil column, the groundwater drainage, the aquifer water storage, ...). This means there are many tunable coefficients which need to be calibrated.

The aim of this study is to evaluate the capability of our integrated modeling system to simulate the local water cycle of the Ofanto river catchment, flowing through the Southern Italy which is a region frequently subject to flash flood events. A meteo-hydrological modelling chain has been set up and 2 simulations have been carried out over winter 2011 and autumn 2013. Several rainfall events as well as dry periods characterise the Southern Italy during the selected time ranges. The strongest weather storms occurred on 1 March 2011 and 1 December 2013 with serious damages in the Southern Italy and flooding of the Ofanto river. The final goal of this work is the meteo-hydrological reconstruction of the selected historical ranges as much reliable as possible.The paper is organised as follows. Section 2 describes the study area. The meteorological and hydrological models and the experimental set-up are presented in Section 3. Section 4 offers the discussion of the modelling results. Conclusions are drawn in Section 5.

3.2 The study area

The basin of the Ofanto river, flowing through the Southern Italy and ending into the Adriatic Sea, has been chosen as a relocatable case study in order to test the meteo-hydrological modeling chain we implemented over the Central Mediterranean area (left picture of Figure (4.2))with a focus on the Southern Italy (right picture of Figure (4.2)). The Ofanto river is a semi-perennial river, whose discharge is close to zero during the dry season but may significantly increase when heavy rain events occur and eventually cause the river flooding. The mean annual discharge at its outlet is around $15m^3s^{-1}$, minimum monthly climatology is $2.27m^3s^{-1}$ in August while it reaches its monthly peak, $35m^3s^{-1}$, in January. The local annual mean rainfall is about 720 mm/year; the annual mean temperature is around $14°C$ (Romano et al., 2009). The watershed area (Fig.(4.3)), covering Campania, Basilicata and Puglia regions in the Southern Italy, is about $2790km^2$ with a mean slope of 8% and its total length is around $170km$ making it the second longest river of the Southern Italy (see top-right panel of Fig.(4.3)). The river source is located south of Torella dei Lombardi, a small village near Avellino at 715 m above the sea level. This is no the only source of the river, few tributaries with lower water volume ensure a constant runoff avoiding the bed to become dry. The Ofanto basin consists of two distinct geological areas: the NorthEastern and the SouthWestern part. The NorthEastern part, representing the downstream reach of the river, is a flat area which includes the flooding area of the river; the SouthWestern part, representing the upstream reach of the river, is mainly mountain/hilly owing to the Appennino range and includes the Vulture volcanic massif (see top-left panel of Fig.(4.3)). This volcanic massif constrains the river to deflect northward drawing a big bend, which tends to erode the slopes of Vulture massif. The sediments, mostly volcanic, carried by the river are released into the sea and concur to create a shallow and sandy coast filling the Gulf of Manfredonia (Romano et al., 2009). Finally the predominant soil type category in the upstream reach is “loam” according to the United States Geological Survey, USGS, dataset data while “clay loam” category prevails in the downstream reach (see bottom-right panel of

Fig.(4.3)). The Ofanto basin is characterized by a karst aquifer in the upstream sub-basin and a porous aquifer in the downstream one, the latter favouring the salt water intrusion from the Adriatic Sea.

This case study is challenging for meteo-hydrological modeling purposes. For what concerns the hydrological purposes, river basins usually show a "rain-runoff" response time which varies from some days for large and/or flat catchments up to few hours for catchment with small sizes (i.e. the Ofanto basin) or complex topography making the forecast highly demanding in the second case. For what concerns the meteorological purposes, the Mediterranean weather storms have been widely investigated and the literature shows they are often characterised by heavy rain, strong wind shear and deep lows which develop as consequences of both the complex orography (e.g. the Alps and Atlas mountains counteract the westerlies and favour the cyclogenesis) and the warm Mediterranean basin (Laviola et al., 2010; Buzzi and Tibaldi 1978). The Ofanto catchment in particular is located in the Southern Italy which is well know as a region frequently subject to flash flood events (Lin et al., 2001, Delrieu et al., 2005, Davolio et al. (2008), Laviola et al., 2011, Miglietta et al., 2008, Moscatello et al., 2008) owing to the simultaneous occurrence of different preconditioning factors: the warm Mediterranean Sea, especially in its Southern part, which feeds the lower layers of the troposphere with heat and moisture as it cools after the summer peak of heat content, the synoptic southerly winds carrying warm-moist air, the complex topography of the Italian Peninsula close to the coastline.

3.3 The experimental set-up of the meteo-hydrological modeling system

A meteo-hydrological modelling system has been implemented to study the local water cycle in the Ofanto basin. The model chain consists of the meteorological mesoscale model Weather Research and Forecasting WRF (Skamarock et al.,

2008), the Land Surface Model NOAH-MP (Niu et al., 2011) and the hydrological model WRF-Hydro (Gochis et al., 2013). NOAH-MP is included in WRF and WRHydro system as sub-model and coupled in two-way mode with both of them. The coupling between WRF and WRF-Hydro system is 1-way mode. The several modules of the models and how they face each other are shown in Figure 4.4. A detailed description of the equations and parameterisations relevant for the discussion of our results is provide in the next paragraphs.

Two simulations have been performed spanning January-March 2011 (hereafter "Experiment 1") and November-December 2013 (hereafter "Experiment 2"). The selected time windows include several rainfall events of different intensity, two of them occurred on 1 March 2011 and 1 December 2013, hereafter referred as "Event 1" and "Event 2", are characterised by the flooding of the Ofanto river. The main features of both Experiments are summarises in Table 3.1.

Figure 3.4 shows the concatenation procedure we adopted for both experiments: a chain of 72h long simulations is carried out and the reinitialization option is chosen for WRF, since we rely on ECMWF 16km analyses to build initial and boundary conditions, while restart option is adopted for WRF-Hydro. Several studies carried out with regional climate models on seasonal and sub-seasonal scale highlighted the benefits of a simulation with frequent reinitialisation with respect to a standard continuous simulation (Lucas-Picher et al., 2013). First of all the reinitialisation mitigates the problems of systematic errors and improves the accuracy in reproducing the local scale precipitation (Qian et al., 2003). We aware this method should evolve in a more rigorous approach based on chains of successive 72 hours long simulations and overlapping of these chains with delayed start-time, e.g. 24 hours (or less): this would allow to neglect the first 24 hours of each 72h simulation as the spin-up period as well as the last 24 hours which are usually affected by the drift of the model results.

3.3.1 Advanced Research WRF meteorological model

The WRF model (version 3.6.1) is a fully compressible and non-hydrostatic mesoscale meteorological model widely used for research studies (mainly the Advanced Research WRF solver core, WRF-ARW, developed at the National Center for Atmospheric Research NCAR and used in this study) as well as operational systems. The basic equations consists of a set of prognostic equations for the conserved state variables (i.e. the volume mass, the velocity components, the virtual potential temperature and the mixing ratios) and a non conserved state variable i.e. the geopotential. Moreover there are two diagnostic equations for the full pressure and the dry inverse density. The model uses a following terrain dry hydrostatic pressure vertical coordinate, we chose 58 unevenly spaced levels and we set the top of the model at 50hPa. Two domains nested in two-way mode are considered: a coarse domain covering the Central Mediterranean area with a horizontal resolution of 6km and a inner domain over the Southern Italy with 2km horizontal resolution (domains are depicted in Figure 4.2). The analyses fields by ECMWF-IFS (European Centre for Medium-Range Weather Forecasts -Integrated Forecasting System) with 16km horizontal resolution and 6h frequency are adopted as WRF initial and boundary conditions.

A set of sensitivity tests (not shown) pointed out the terrestrial datasets, i.e. the topography elevation and the land use categories, strongly affect the air-land fluxes and the near surface atmospheric fields. Thus the default USGS datasets with 800m resolution for topography and land use have been upgraded with higher resolution and more recent data: Corine 250m Land Use categories and EUDEM 30m topography data both released by European Environmental Agency (EEA), SRTM 90m topography data by NOAA.

Moreover different numerical schemes for the parameterised physical processes have been tested and and compared by evaluating how they affect the simulation of the near surface atmospheric fields. The final model configuration uses RRTMG scheme (Iacono et al., 2008) for long-wave and short-wave radiation, Monin-Obukhov scheme (Monin et al., 1954) is adopted for the surface sub-layer of the Planetary Boundary Layer, PBL, and YUS (Yonsei University scheme)

non local K-profile scheme (Hong et al., 2006) for PBL mixed sub-layer. The cumulus-convection parameterization is based on Kain-Fritsch scheme (Kain et al., 1993) in the coarse domain while no convection scheme, thus the convection is assumed to be explicitly solved, in the inner domain. The mycrophysics is based on Double-Moment 6-classes Thompson's scheme (Thompson et al., 2004) for both domains.

Table 3.2 summaries all the chosen terrestrial datasets and parameterisation schemes.

3.3.2 NOAH-MP land surface model

A standard "column-only" land surface model, NOAH-Multi Physics (Niu et al., 2011) is coupled in two-way mode with both WRF-ARW and WRF-Hydro systems. The model solves the surface and subsurface soil processes with 4 soil layers up to 1m below the ground level (layer thicknesses are 0-10cm, 10-30cm, 30-60cm, 60-100cm). A multilayer snowpack is also modelled. Basic equations are the prognostic equations for the soil moisture content (Richards' equation) and the temperature of each soil layer plus a diagnostic equation for the soil surface water budget. Moreover a set of parameterisations schemes are used to compute the surface energy flux components (Niu et al, 2011), the groundwater drainage at the bottom of the deepest soil layer and the partitioning of the soil surface water (sum of rainfall, dewfall and snowmelt reduced by the evaporation rate) into infiltration rate and surface runoff (Niu et al., 2007). The parameterisation of infiltration rate, surface runoff and groundwater drainage are key issues for the hydrological modelling performed by WRF-Hydro and are affected by the calibration of soil texture and moisture coefficients.

The infiltration rate, I (units of ms^{-1}), is computed as:

$$I = min(\dot{H_{sfc}}, F_{frz} I_{MAX}) \tag{3.1}$$

and the surface runoff (units of ms^{-1}) is parameterised as follows:

$$R = max(0, \dot{H_{sfc}} - F_{frz} I_{MAX}) \tag{3.2}$$

where $\dot{H_{sfc}}$ is the current surface water rate (units of ms^{-1}) given by the sum of water input (i.e. rainfall, dewfall, snowmelt and the stored surface water) minus the evaporation rate and is computed by the surface water budget equation. F_{frz} is the fractional impermeable area as a function of soil ice content of the surface layer, I_{MAX} is the maximum soil infiltration capacity (units of ms^{-1}) dependent on soil texture and moisture.

The NOAH-MP model parameterises I_{MAX} as an empirical function of 4 tunable soil coefficients (all with units of m^3/m^3): the maximum surface moisture content SMC_{MAX}, the minimum surface moisture content the plant requires not to wilt or below which the transpiration ceases SMC_{WLT}, the surface infiltration coefficient $REFKDT$ and the saturation of soil hydraulic conductivity $REFDK$.

The empirical formula is given below:

$$I_{MAX} = H_{max}\frac{C_{inf}}{H_{max} + C_{inf}}/\Delta t \tag{3.3}$$

where the maximum surface water level (units of m) is given by:

$H_{max} = max(0, \dot{H_{sfc}}\Delta t)$

and the infiltration capacity, C_{inf} (units of m), at the upper soil layer (k=1) is computed following the exponential formula below:

$$\begin{aligned} C_{inf}(k=1) = [\sum_{k=1}^{N} \Delta z(k=1)(SMC_{MAX} - SMC_{WLT})(1.0+ \\ -\frac{(SMC(k=1) - SMC_{WLT})}{(SMC_{MAX} - SMC_{WLT})})] \cdot (1 - e^{-\frac{SMC_{MAX} \cdot REFKDT}{REFDK}\Delta t_1}) \end{aligned} \tag{3.4}$$

where $\Delta z(k=1)$ is the thickness of the upper soil layer (with $k = 1 : N$ and $N = 4$), Δt_1 is the model time step converted to the ratio of a day thus given by $\Delta t_1 = \Delta t/86400$, $SMC(k=1)$ is the soil moisture content (units of m^3/m^3) of the NOAH-MP upper layer, solved from Richards' equation. Finally the tunable parameters SMC_{MAX}, SMC_{WLT} are soil type dependent while $REFKDT$ and $REFDK$ are prescribed as unique values.

We found the computation of groundwater drainage is also a crucial step since this is assumed to be the recharge flow which feeds the unconfined aquifer below the soil column.

The groundwater drainage is assumed to be a free gravitational drainage, Q_{bot}

(units of mms^{-1}), thus formulated as function of the current soil moisture content in the deepest soil layer:

$$Q_{bot} = SLOPE \cdot DKSAT \cdot [max(0.01, SMC(k=4)/SMC_{MAX})]^{2 \cdot B+3} \cdot (1 - F_{frz}) \tag{3.5}$$

where $SMC(k = 4)$ is the soil moisture content (units of m^3/m^3) of the NOAH-MP deepest layer (k=4), solved from Richards' equation. $DKSAT$ and B are soil type dependent coefficients, the first is the saturated soil hydraulic conductivity (units of mms^{-1}), the second is a non-dimensional value accounting for soil texture. Finally $SLOPE$ is a coefficients between 0.1-1.0 modifying the gravitational free drainage out of the bottom layer depending on the surface slope categories of each grid cell: 9 slope classes are prescribed with different range of surface percent slope following Zobler's method (1986).

3.3.3 WRF-Hydro hydrological model

In this study, WRF-Hydro version 2 (Gochis et al., 2013) has been implemented over WRF inner domain. Preliminarily, a detailed terrain routing grid is computed by a GIS system over the domain, we chose a resolution equal to 200m that is 10-times higher than the one of NOAH-MP spatial grid. This terrain routing grid contains the data layers required to describe the surface and subsurface water routing. The data layers are the topography (see top left picture of Figure 4.3), the flow-direction grid, the flow accumulation grid (see top right picture of Figure 4.3), the watershed/aquifer grid (see bottom left picture of Figure 4.3) and the catchment grid. The flow-direction grid specifies the direction in which each surface cell drains by determining which neighbouring cell is the lowest. The flow-accumulation grid records the number of cells that drain into an individual grid cell. The watershed grid is constructed by identifying the grid points exceeding a minimum threshold value of flow accumulation and they are assumed to be the river network points. The aquifer grid is assumed to identically match the watershed grid and sub-basins may be defined as the areas upstream the monitoring points set along the river network. We select 4 monitoring points

(three gauge stations and the outlet) along the Ofanto river as detailed in the bottom left panel of Figure 4.3 and thus the watershed, or equally the aquifer, is divided into 4 sub-basins. The catchment grid is finally defined following the Strahler's method (1952): an increasing index is assigned to the watershed grid points in order to distinguish the branches and identify a hierarchy of tributaries. WRF-Hydro model has been designed to integrate the "column only" NOAH-MP model with several physics modules which describe the lateral routing of surface and subsurface water flows and how they interact each other.

The WRF-Hydro system includes 4 routing modules which represent the saturated subsurface flow, the 2d overland water flow, the aquifer recharge/discharge and the 1d channel streamflow (Figure 4.4).

The saturated subsurface flow module is activated when a supersaturation of the water column occurs at soil layer k, meaning that $SMC(k) > SMC_{MAX}$, and the saturated lateral flow is assumed to follow the topography down gradient neighbour.

The overland water flow occurs when the surface water level of specific grid cells exceed a fixed retention depth which is assumed to depend on the surface slope. The overland water flow is represented by the 2d shallow water equations that are applied under the diffusive wave hypothesis, meaning that the inertia term of the momentum equation is neglected. Moreover the shear stresses in the momentum equation are negligible. Under all these hypotheses the shallow water governing equations read:

$$\frac{\partial h}{\partial x} - S_{fx} + S_{ox} = 0 \tag{3.6}$$

$$\frac{\partial h}{\partial y} - S_{fy} + S_{oy} = 0 \tag{3.7}$$

$$\frac{\partial h}{\partial t} + \frac{\partial q_x}{\partial x} + \frac{\partial q_y}{\partial y} = i_e \tag{3.8}$$

where the unknowns are the water column thickness $h = h(x, y, t)$ (units of m) defined as the free surface elevation minus the bottom topography $h = \tilde{h} - h_{bot}$, and the unit discharges (units of $m^2 s^{-1}$) in the x- and y- directions, i.e. $q_x = h(x, y, t)u(x, y, t)$ and $q_y = h(x, y, t)v(x, y, t)$. The sink/source term of the continuity equation, i_e, is the surface runoff parameterised by NOAH-MP

(as detailed in eq.(3.2)). Moreover $S_{fx} = \frac{\nu}{g}\frac{\partial^2 u}{\partial x^2}$ and $S_{fy} = \frac{\nu}{g}\frac{\partial^2 v}{\partial y^2}$ are the non-dimensional friction slope terms (where ν is the kinematic viscosity coefficient with units of L^2T^{-1}) and $S_{ox} = \frac{\partial h_{bot}}{\partial x}$ and $S_{oy} = \frac{\partial h_{bot}}{\partial y}$ are the non-dimensional terrain slope terms. Finally $\frac{\partial h}{\partial x}$ and $\frac{\partial h}{\partial y}$ are the non-dimensional pressure slope terms.

The S_{fx} and S_{fy} terms are computed by analytically solving the momentum equation where h is assumed to be the overland water level provided by NOAH-MP water budget equation. The Manning's empirical formula provide the units discharges q_x and q_y as follows:

$$q_x = \frac{\sqrt{|S_{fx}|}h^{5/3}sign(S_{fx})}{n} \tag{3.9}$$

$$q_y = \frac{\sqrt{|S_{fy}|}h^{5/3}sign(S_{fy})}{n} \tag{3.10}$$

where $h(x, y, t)$ is the unknown of the continuity equation (3.8) and the surface roughness coefficient, $n(x, y)$ (units of $sm^{-1/3}$), is a tunable parameter defined as function of the land use categories. The unit discharges q_x and q_y are then replaced in the continuity equation and $h = h(x, y, t)$ is numerically solved with the Courant constraint ensuring the stability of numerical solution.

The diffusive wave equations allow for backwater effects and waterflow on adverse slopes, this represents an added value with respect to the widely used kinematic wave models which neglect the pressure slope terms.

The channel streamflow is computed on a pixel-by-pixel basis along the river network grid. The river network has a trapezoidal geometry, its parameters (side slope, bottom width and roughness coefficients) are "a priori" defined as function of Strahler's stream order. The river streamflow is activated if river network points intercept the 2d overland waterflow. The governing equations are based on the same assumptions of 2d overland waterflow including the diffusive wave hypothesis and are written as follows:

$$\frac{\partial A}{\partial t} + \frac{\partial Q}{\partial x} = q_{lat} \tag{3.11}$$

$$\frac{\partial h}{\partial x} = -S_0 + S_f \tag{3.12}$$

where the unknowns are the volume flow rate $Q = Q(x,t)$ and the wetted area $A = A(x,t)$. The channel water level $z(x,t)$is derived from A by considering the trapezoidal shape of the channel section: $A(x,t) = (L_{bot} + \alpha z(x,t))z(x,t)$ where L_{bot} and α are the bottom width and the side slope of the channel cross section.Similarly to the 2d shallow water equations, S_f is the friction slope term, S_0 is the terrain slope term and $\frac{\partial h}{\partial x}$ is the pressure slope term with h assumed as the water level solved by 2d continuity equation (3.8). Finally q_{lat} is the lateral flow (units of $m^2 s^{-1}$) in (positive) or out (negative) of the channel and is supplied by the surrounding overland water flow and the aquifer recharge as follows:

$$q_{lat}(x,y,t) = \sqrt{q_x(x,y,t)^2 + q_y(x,y,t)^2} + \frac{Q_{out}}{S_{catch}} h(x,y,t) \tag{3.13}$$

with q_x and q_y are computed by the 2d momentum equation (3.6-3.7) and by taking into account the only overland computational grid points bordering the river points, in the second term on the RHS of (3.13) Q_{out} is the aquifer discharge and S_{catch} is the catchment area. To note that for a specific watershed a conceptual unconfined aquifer is located below the bottom layer of NOAH-MP with an horizontal extension matching the catchment area thus the aquifer discharge may directly feed the river streamflow (equation 3.14 below). The aquifer model is forced in 1way mode by NOAH-MP groundwater drainage and feeds in turn the shallow water system for the river streamflow. The inflowing volume flux into the aquifer is represented by the groundwater drainage at the deepest soil layer, Q_{bot} given by eq.(3.5). The aquifer discharge, Q_{out}, is computed at each model time step and for each sub-region of the catchment as an empirical exponential function of the NOAH-MP groundwater drainage Q_{bot} and then the the following minimum value is assumed:

$$Q_{out} = min(C(e^{\frac{\alpha \cdot z}{z_{max}}} - 1), z \cdot S_{catch}/dt) \tag{3.14}$$

where z is the current conceptual water depth of the aquifer given by the sum of the groundwater drainage and the stored aquifer water $z = z + Q_{bot}dt$. Tunable parameters are the initial value of the aquifer water depth z_{ini} (units of mm), the maximum value of the aquifer water depth, the exponential law coefficient α, the volume capacity of the aquifer C (units of m^3/s). To note the aquifer bucket

is divided into sub-basins according to the number of monitoring points selected along the river network. For our case study, we selected 4 monitoring points along the Ofanto network and thus the river aquifer consists of four sub-regions located upstream of each monitoring point as shown in the bottom-left panel of Fig.4.3. The solving strategy is the same adopted for 2d shallow water (eq.3.6-3.8) with eq.3.12 analytically solved to get S_f which is replaced in the Manning's formula for 1d channel to derive Q as empirical function of A. The discharge Q is then replaced in eq.3.11 which is numerically solved and provides the wetted area A. The Manning formula for 1d channel is:

$$Q = \frac{A^{5/3}\sqrt{|S_f|}sign(S_f)}{P^{2/3}n} \tag{3.15}$$

where P is the wetted perimeter computed as function of h as given by eq.(3.8), and n is the tuneable coefficient for channel roughness and is defined as function of the Strahler's stream order of each branch.

3.4 Analysis of the modeling results

The discussion of the modelling results focuses on two fields: the precipitation and the river streamflow. We show the validation of both fields and the calibration of tunable coefficients involved in the parameterisation schemes of WRF-Hydro. Critical issues as the predictability limits of the precipitation field and the required spin-up of meteorological simulations are pointed out. The added value of modelling both the surface and subsurface runoff, the water storage in the aquifer and the river routing is stressed too.

3.4.1 Mesoscale meteorological features

Figure 4.5 and Figure 4.6 provide the mesoscale maps of the two severe weather events, Event 1 and Event 2, which occurred during the chosen simulation periods.

The mesoscale analysis proves the WRF capability to capture the weather storms

which hit the Southern Italy. Maps of 500hPa geopotential point out how the upper level features affect the lower level cyclogenesis. WRF maps for Event 1 show a strong trough of low pressure at 500hPa centered over the Tirrenian Sea (top panel of Figure 4.5) which is due to a cold front (not shown) progressing eastward. At lower levels strong synoptic winds, coming from the SouthEast and blowing over the warm Mediterranean Sea, reach the Italian Peninsula (bottom panel of Figure 4.5) and turn into a weak cyclonic pattern centred over the Tirrenian Sea. Maps of 500hPa geopotential for Event 2 show a weak trough in the upper troposphere which covers the Western Mediterranean Sea and Atlas region (top panel Figure 4.6), with a small deeper core south of Sicily, and corresponds to a strong cyclonic circulation at lower level (bottom panel Figure 4.6). This cyclone is triggered by the combination between southerly winds carring warm-moist air and reaching the the Southern Italy and a colder wind developing downslope the Balkans.

These mesoscale convective systems triggered Event 1 and Event 2 over the Southern Italy with heavy local rainfall and flooding on the major rivers. As detailed in the Reports by Puglia Civil Protection, anomalous rainfalls hit the Puglia region during both events. A precipitation peak of 186.9 mm/day was recorded on March 1^{st} 2011 (Event 1) at Quasano station exceeding its historical maximum value of 116mm/day reached in 2010. On December 1^{st} 2013 (Event 2) another anomalous amount of precipitation was recorded with 189.6 mm/day (77% fallen in only 12 hours) reached at Bovino station with respect to a historical maximum value of 135.6mm recorded in 2003. Many other gauge stations reached their absolute maximum rainfall during Event 2 as Quasano, Orsara di Puglia, Cassano Murge, Orto di Zolfo and Castel del Monte.The Ofanto river flooded few days after both events and the recorded water level at Cafiero gauge station reached 4.62 m on 6^{th} March 2011 and 6.48 m on 7^{th} December 2013, close to the historical maximum value of 6.8 m recorded on November 11, 1929. The Cafiero station was damaged after Event 2 because of the flood thus the maximum value reached could be higher. Another high water level characterises Experiment 1 on 19 February 2011 with 5.32 m as the maximum value gauged at Cafiero station.

3.4.2 The Precipitation field

3.4.2.1 Validation of the results

A comprehensive analysis of the simulated precipitation in the Ofanto basin is carried out by means of 27 rain gauge stations which cover the whole simulation periods with 30-minute frequency (the stations are marked in Fig.4.3-top left panel). To note that a quality control of the observations has been performed and one station is removed from the validation of Experiment 2. Figure 3.7 shows the validation of modelled precipitation by considering for both experiments the stations with the best and worse statistics. Overall the WRF model captures fairly well the localisation, the amount and the timing of the rainfall. The averaged statistical indices are calculated on daily basis (which is usually adopted for validation of the precipitation forecasts) and summarise in Table 3.3. Experiment 2 shows a better correlation than Experiment 1, a lower NRMSE (computed as the root mean square difference divided by the standard deviation) and higher BIAS (computed as model minus observation value). This is an expected result since the Experiment 2 is characterised by a first period (i.e. november 2013) of continuous rainfall and a second period almost dry while several shorter rain events succeed one another during Experiment 1 making hard the simulation of the single events.

3.4.2.2 The sensitivity to the Initialization Time

The full prediction of localisation, amount and timing of rainfall is well know as a tricky issue for the mesoscale models owing to the meso-β and meso-γ scales involved in these events. In our experiments the horizontal resolution of WRF inner domain is 2 km thus we are exactly in the "gray-zone" resolutions for convection, where the power spectrum of the turbulence reaches its peak. This means the WRF model is not able to fully reproduce the convective motions and consequently the rainfall events with local scale features. Moreover the concatenation procedure we chose consists of a chain of WRF simulations 72 hours long with reinitialisation option and may suffer a initialisation time particularly close or far from the occurrence of peak events: in the first case the model is unable to

develop the mesoscale features required to trigger the local weather pattern, in the second case the numerical drift may affect the hindcast results (Fiori et al, 2014). Figures 3.8 highlights the sensitivity of the simulated precipitation to the initialization time: left panel shows the observed 24h cumulated precipitation as recorder by gauge stations on February 18^{th} 2011 at 14:00 UTC, the middle and right panels show the model findings with different initialization times. We found the simulation initialized 38 hours before the recorded rain peak (right panel) exhibits a pattern more similar to the available observations (left panel) with respect to the one initialized 14 hours before (middle panel) Similarly, for the rain peak recorded at 12:00 UTC on December 1^{st} 2013 the adopted concatenation procedure includes a WRF simulation starting 12h before the peak, thus a new simulation with a lead-time of 36 hours has been overlapped. Thus we argue a spin-up period of at least 24 hours is needed. Moreover we plan to adopt a different concatenation procedure in the future implementations of our meteo-hydrological system with the overlap of more chains consisting of 72h long runs with delayed start time. This would allow to discard the first 24 hours and the last 24 hours of each 3 days run and to hold only the central 24 hours which are expected to be the most reliable ones.

3.4.2.3 The correction of the precipitation field

We followed the Barnes (1964) "method of successive corrections" which enables to reduce the spatial shift of the modelled precipitation and to avoid the uncertainties associated with the WRF precipitation propagate into the WRF-Hydro simulations. We used the rain-gauge stations available in the Ofanto watershed with 30-minutes time frequency. The following formula is adopted for the correction of the precipitation field:

$$\varphi(i,j) = \varphi_b(i,j) + \frac{\sum_{i=1}^{N_d} w_i E_i}{\sum_{i=1}^{N_d} w_i} \tag{3.16}$$

where φ_b is the "first guess" that is the precipitation field as simulated by WRF at (i,j) model grid point, φ is the corrected precipitation field, N_d is the number

of gauge stations available in the Ofanto catchment ($N_d = 27$ in Experiment 1 and 23 in Experiment 2), $E_i = O_i - \varphi_b^i$ are the error field defined as the difference between O_i representing the observed precipitation at i^{th} gauge and φ_b^i which is the first guess bilinearly interpolated at i^{th} gauge. The weights, w_i, are computed as follows:

$$w_i = exp\big(-4\frac{R_i^2}{D^2}\big) \tag{3.17}$$

where D is the radius of influence of the observations set equal to 25km in our study, and R_i is the distance of each model grid points with the i^{th} observation. The enhancement of the representation of the precipitation field by means of Barnes' method is stressed in Figure 3.9 for Experiment 1 and Figure 3.10 for Experiment 2. These figures focus on the rainfall peak events of March 1^{st} 2011 (Event 1) during Experiment 1 and December 1^{st} 2013 (Event 2) during Experiment 2. In both Figures the left picture shows the background field that is the precipitation field as simulated by WRF, the middle panel shows the in situ observation used for applying the Barnes' scheme and the right picture provides the corrected precipitation field. Barnes' method is proved to overcome the WRF shortcomings in the spatial localisation and amount of simulated precipitation.

3.4.3 The river streamflow

3.4.3.1 Validation of the results

We used the observed data of water level at Cafiero station to validate the modelled river streamflow. Figure 3.11 shows the observed and modelled hydrograph of the Ofanto river during Experiment 1 by considering the final set up of WRF-Hydro and by using the simulated precipitation (top panel) or the assimilated one (bottom panel). Similarly Figure 3.12 refers to Experiment 2. To note that the gap in the observe time series is due to the river flooding.

In both Experiments working with modelled precipitation we tend to overestimate the river water level. This overestimation is reduced by means of assimilated precipitation (eq.3.16) and thus the runoff peaks are better captured. Moreover the

timing and the amount of the precipitation as simulated by WRF, is expected to affect the volume and the shape of the hydrograph and thus we adopt the strategy of overlapped WRF runs (see fig.3.8) when time lags in the reconstruction of hydrograph are found. To note that even the overlapping strategy doesn't allow to better reproduce the peak on November 23^{th} 2013 during Experiment 2. This peak is not captured especially when the corrected precipitation is adopted and this shortcoming will be further investigated.
On the whole the final configuration of the meteo-hydrological modelling chain including an appropriate calibration shows a satisfying performance when the precipitation uncertainties are low. The WRF-Hydro system is capable to reasonably simulate the Ofanto hydrograph and to correctly reproduce the main peaks event s as well as the plateaus. We found the calibration of the infiltration rate and the aquifer recharge-discharge are crucial to improve the model performance as detailed in the next paragraph.

3.4.3.2 Sensitivity to NOAH-MP and WRF-Hydro tunable parameters: performed calibration and aquifer set-up

A manual calibration is employed with the aim of identifying the most relevant parameters and roughly calibrating them. We trust a manual calibration is less powerful than a more sophisticated procedure based on a statistical approach but on the other hand this simple approach avoids the uncertainties arising from the tuning of highly correlated parameters.
Preliminary we focused on the tunable parameters of the land surface model which control the total water volume.
Several tests have been carried out to point out the role of the tuneable coefficients and finally we found out 3 parameters playing a key role in the Ofanto catchment: the slope coefficient of Class 2, the infiltration coefficient $REFKDT$ and the maximum soil moisture content SMC_{MAX} of "Clay-Loam" soil type (all have units of m^3/m^3) . They directly affect the surface water budget equation and the soil moisture equation of NOAH-MP through the parameterisations of infiltration capacity (eq.3.4) and groundwater drainage (eq.3.5). Moreover they

indirectly condition the WRF-Hydro overland water flow through the source term (eq. 3.2) of shallow water system and the aquifer discharge law (eq.3.14) through the groundwater drainage. The tuned values of the parameters are listed in Table 3.4.

The $SLOPE$ coefficients modify the gravitational drainage out of the bottom layer of NOAH-MP and are function of the surface percent slope. The slope classes which characterise the Ofanto basin are class 1 (i.e. 0-8% slope and coefficient equal to 0.1), class 2 (i.e. 8-30% slope and coefficient equal to 0.6), class 4 (i.e. 0-30% slope and and coefficient equal to 0.35) and class 6 (i.e. 8-30% and ¿30% slope and coefficient equal to 0.8) with the steepest class, Class 6, located in the upstream sub-region of the basin and the others in the downstream part. Class 2, which affects a small portion of the basin in the southern part of the Ofanto low valley, prescribes a relative high value of $SLOPE$ coefficient equal to 0.6, but the tuned value has been reduced to 0.2. We reduced the slope coefficient of Class 2 making it closer to the values which characterise the low valley of the Ofanto river and we speculate this means the $SLOPE$ coefficients should be assumed to be function not only of the surface slope but also of the soil types. The seasonality of the soil physical processes is also pointed out by additional sensitivity tests on the tunable parameters: we found out two of them, i.e. the infiltration coefficient and the maximum soil moisture content of "Clay-Loam" soil type, are seasonally dependent and thus different values are assumed in the two Experiments. In winter season, the soil is expected to be wetter than in autumn and the soil porosity lower, this implies the values of REFKDT and SMC_{MAX} are fixed as lower in Experiment 1 than in Experiment 2.

After this first phase of calibration we focused on the parameters controlling the hydrograph shape. The Manning's 2d and 1d roughness coefficients play a crucial role in the computation of discharge as they are involved in the empirical formula for computing the unit discharges q_x and q_y (eq.3.9-3.10) of 2d water flow as well as the channel streamflow discharge Q (eq.3.15). The 2d roughness coefficients are indexed using the Land Use Categories and the 1d coefficients are assigned on the basis of Strahler's stream order. We upgraded the computation of the 2d roughness coefficients by replacing the default USGS Land Use Categories with

the higher resolution and updated Corine data (EEA dataset) and we refined the computation of Strahler's order and thus the 1d roughness coefficients by adopting the higher resolution and updated EUDEM topography data (EEA dataset) . The calibration of WRF-Hydro aquifer is manually performed too, and tuned values of aquifer coefficients are uniquely defined and listed Table 3.5. We guess the aquifer discharge is controlled by the soil texture which affect the soil hydraulic conductivity, thus we distinguish between the upstream sub-basin (sub-basin 1) and the low valley of the Ofanto (sub-basin 2, 3 and 4) following the basin partition described in bottom left panel of Fig.4.3. The low valley "Clay Loam" soil type is much less pervious than the upstream "Loam" soil type, thus the low valley is characterised by a lower hydraulic conductivity and tend to counteract the upward aquifer discharge. This means we set the values of the aquifer initial water depth z_{ini}, the exponential law coefficient α and the volume capacity C as lower in the downstream sub-basins 2, 3 and 4 with respect to the upstream sub-basin 1, while z_{max} is higher.

Figure 3.13 points out the key role of representing the aquifer discharge. The comparison of the modelled time series of Fig.3.13 (aquifer switched off) with Fig.3.11-bottom panel (aquifer switched on) demonstrates the aquifer affects the baseflow and thus the plateaus among the peak discharges.

3.4.4 WRF-Hydro simulated river runoff versus NOAH-MP parameterized surface runoff

We highlight the added value of coupling the land surface model NOAH-MP with a hydrology/hydraulics model as WRF-Hydro in Figure 3.14. The "column only" land surface model NOAH-MP parameterises the surface runoff through eq. (3.2) and this is inadequate to represent the Ofanto hydrograph as stressed in the related timeseries of Fig.3.14. WRF-Hydro system realistically routes the river streamflow as well as the subsurface waterflow and aquifer storage which eventually feeds the river network. Overall we found out the integrated modelling system including atmosphere, land surface, hydrology and hydraulics components is able to reproduce the local water cycle of the Ofanto basin and thus the Ofanto

river hydrograph.

3.5 Conclusions

The goal of this work is a realistic reconstruction of meteo-hydrological events for a specific river basin. We aimed to point out the strenghts of our meteo-hydrological modelling system as well as its shortcomings.

We chose the catchment of a semi-perennial river, i.e. the Ofanto river, as our case study. This is a demanding case study since it is a small-size catchment with short "rain-runoff" response time and is located in the Southern Italy, a region frequently subject to flash flood events. We simulated the local water cycle during two time windows characterized by the occurrence of severe weather events with flooding of the river.

Model findings and their comparison with available in situ observations confirm the importance to represent the local water cycle by means of an integrated modelling system which includes the atmosphere, the hydrology and the hydraulics and which is able to explicitly solve the subsurface and surface runoff, the aquifer water storage and the river routing.

The final set-up of the WRF model has been achieved by several sensitivity tests in order to select the most effective parameterisation schemes and input forcings. Overall the localisation, the amount and the timing of the rainfall is captured fairly well as stressed by the statistical indices. The Barnes correction method enabled to increase the quality of modelled precipitation field and to avoid the related uncertainties propagate into WRF-Hydro simulations. The Ofanto hydrograph, including both peak events and plateaus, has been reproduced during the two simulation periods. We found out the representation of the aquifer recharge/discharge and the parameterisation of the infiltration rate and surface runoff are key issues for improving the model performance. Moreover the aquifer recharge/discharge law enables to take into account the aquifer water storage which may directly feed the river network. Thus a great effort has been devoted to the calibration of the tunable coefficients involved in the parameterisation schemes of both NOAH-MP and WRF-Hydro. The coefficients

of the aquifer recharge/discharge law have been calibrated as soil type dependent while the coefficients for infiltration rate and soil moisture content are found to be seasonal dependent. The performed calibration seems to indicate the SLOPE coefficients should be prescribed as function of soil types as well as the surface slope. Finally the roughness coefficients involved in the shallow water equations for 2d overland water flow and 1d channel streamflow are respectively prescribed as function of the land use categories and the topography data and thus we benefited from working with higher resolution and upgraded terrestrial data.

The comparison of the Ofanto hydrograph reproduced by WRF-Hydro and the surface runoff simulated by NOAH-MP, highlights a "column only" land surface model is definitely inadequate for the hydrological purposes and the coupling with a hydrological model is needed.

The critical issues we faced in this study are also pointed out. We experienced the predictability limits of the precipitation field and the required spin-up of the meteorological forecasts. Our model resolution is in the "gray-zone" for convection and thus the precipitation is expected to be only partially solved. Furthermore the WRF capability to reproduce the heavy rain events is strongly sensitive to the initialization time: the model could be unable to develop the mesoscale features of a weather pattern if it is too close to the initialization time, on the other hand the numerical drift may imply the model cannot capture the event if too far from the initialization time. We found a spin-up period of about 1.5 day is needed to capture the local heavy rainfall.

As a future development we plan to adopt a more robust concatenation procedure of re-initialised WRF simulations: an ensemble of chains of 72-hours simulations with delayed start-time. We also point to a more powerful approach for correcting the precipitation field, based on the data assimilation technique. Finally a future effort could be devoted to fully prognostically solve the WRF-Hydro shallow water system instead of the current diffusive wave approximation.

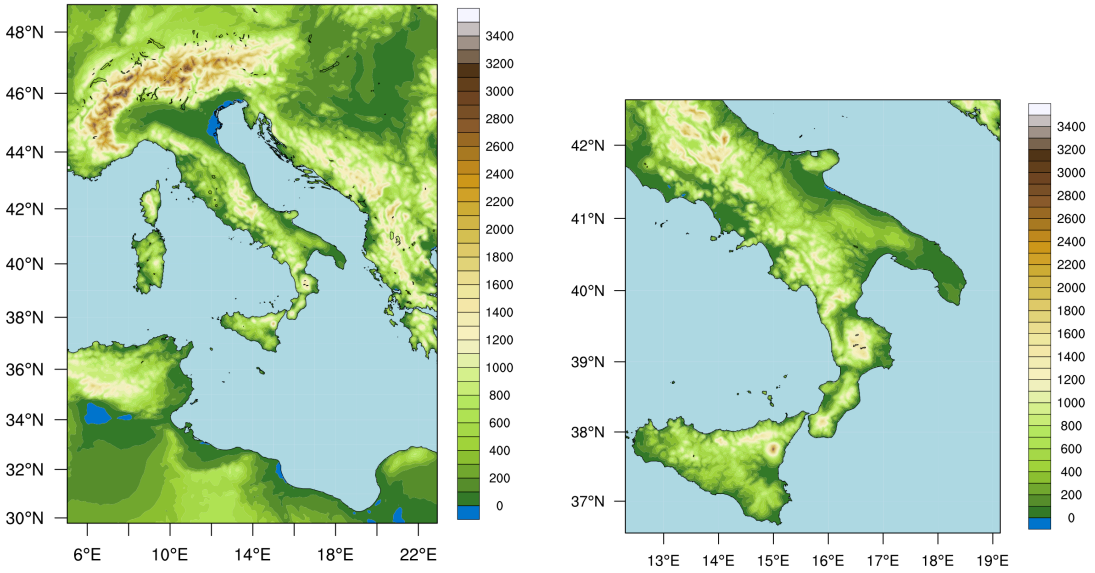

Figure 3.1: The study area. Left panel: WRF coarse domain (EEA-SRTM topography dataset). Right panel: WRF inner and WRF-Hydro domain (EEA-Eudem topography dataset)

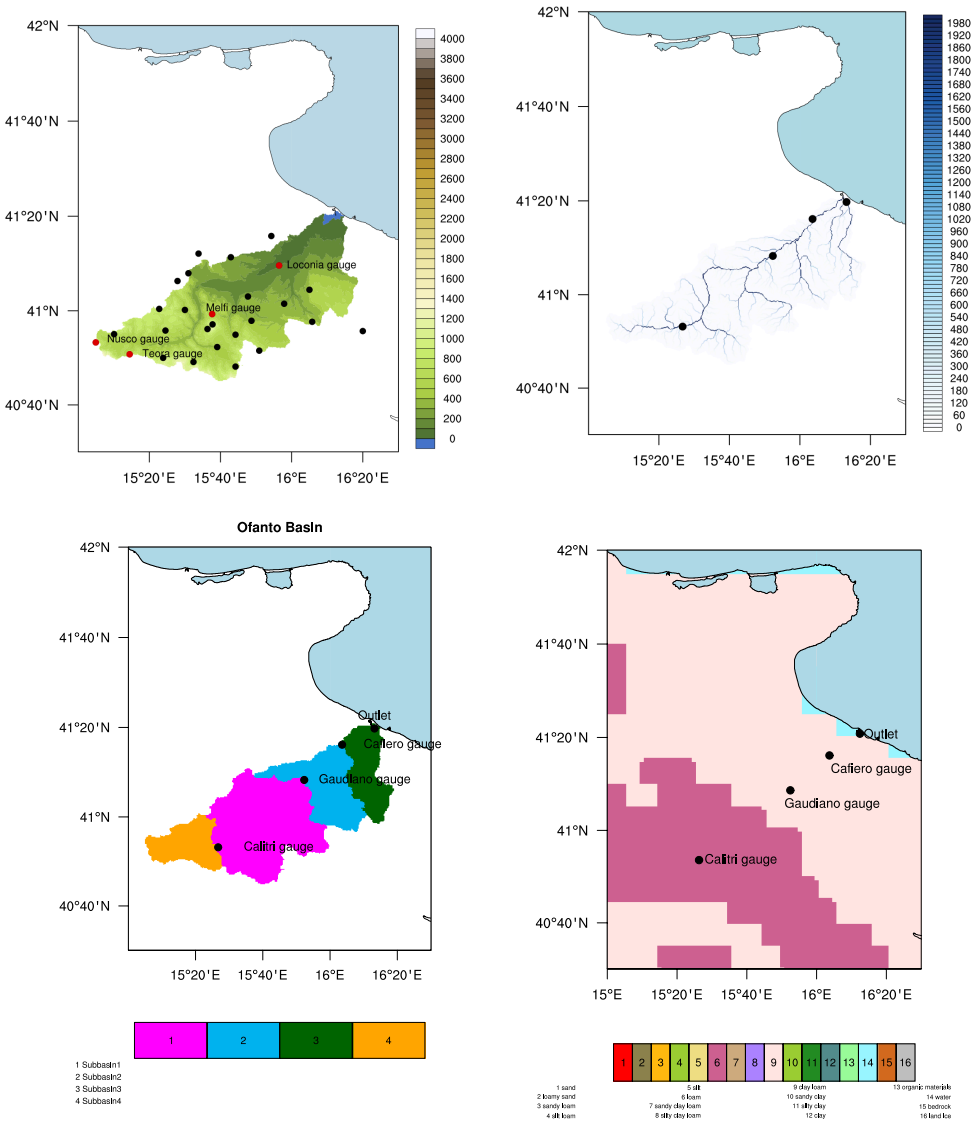

Figure 3.2: The Ofanto river Catchment. Top left panel: Topography height (units of m) and location of 27 rain-gauge stations in the catchment. Top right panel: Flow Accumulation grid defined by the number of grid cells which drain into an individual cell along the river network grid. Bottom left panel: The whole basin and the 4 sub-basins (coloured zones) defined as the areas upstream of the selected monitoring points (black dots). Bottom right panel: USGS Soil Type Categories in the region of the Ofanto basin.

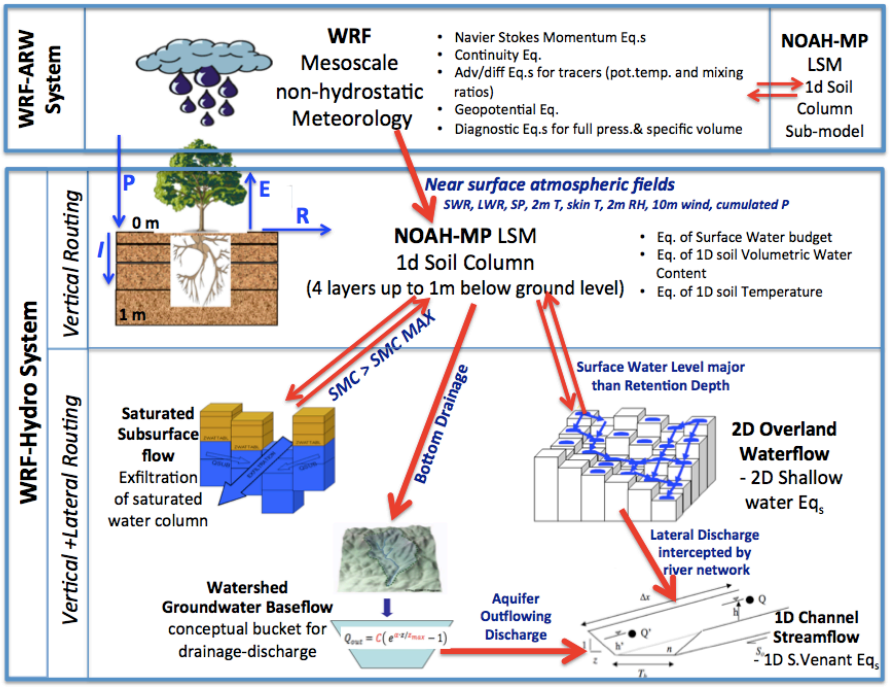

Figure 3.3: The meteo-hydrological modeling chain

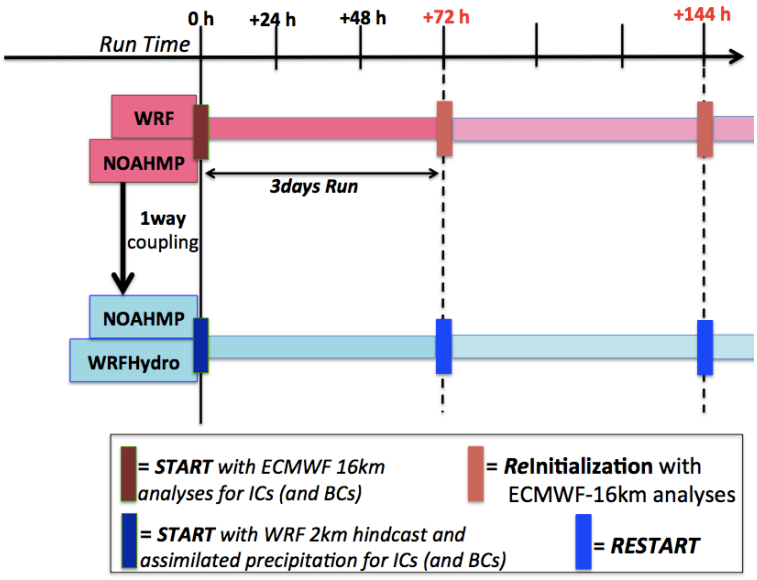

Figure 3.4: The concatenation procedure of the simulations

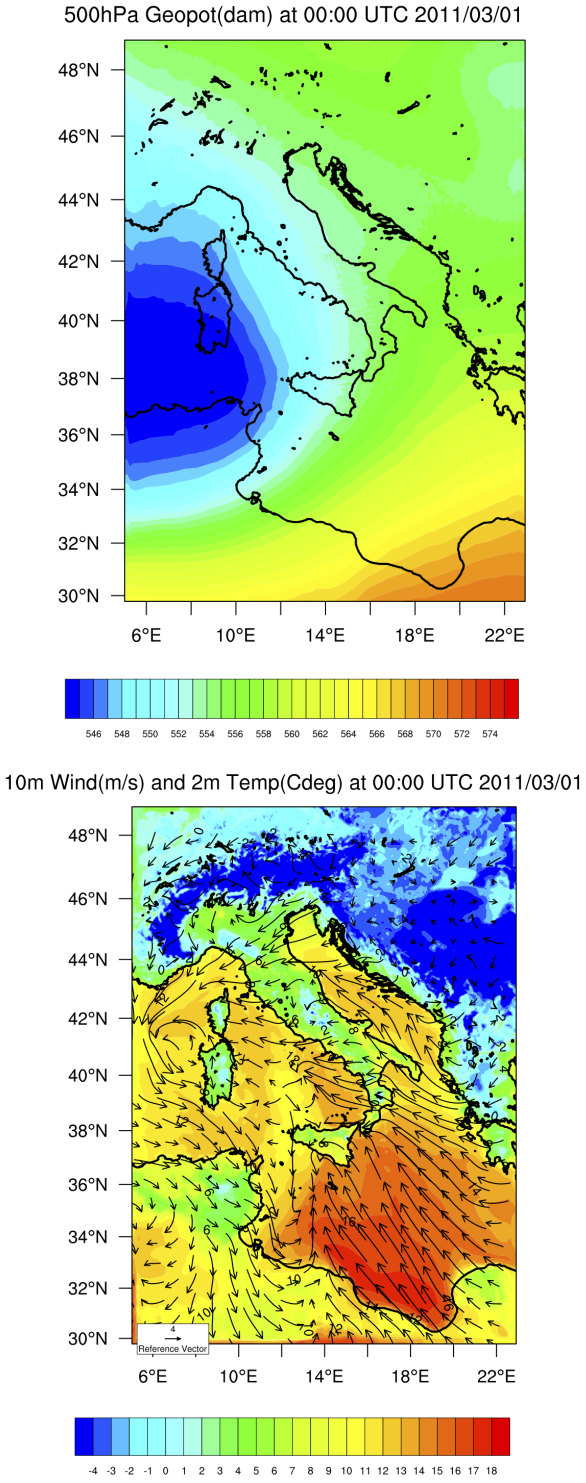

Figure 3.5: Mesoscale maps during the weather storm on 1 March 2011 (Event 1). Top panel: WRF (domain1) Geopotential height (in m/10, colours) at 500hPa. Bottom panel: WRF (domain1) 2m Temperature (in Cdeg, colours) and 10m wind (in m/s, black arrows).

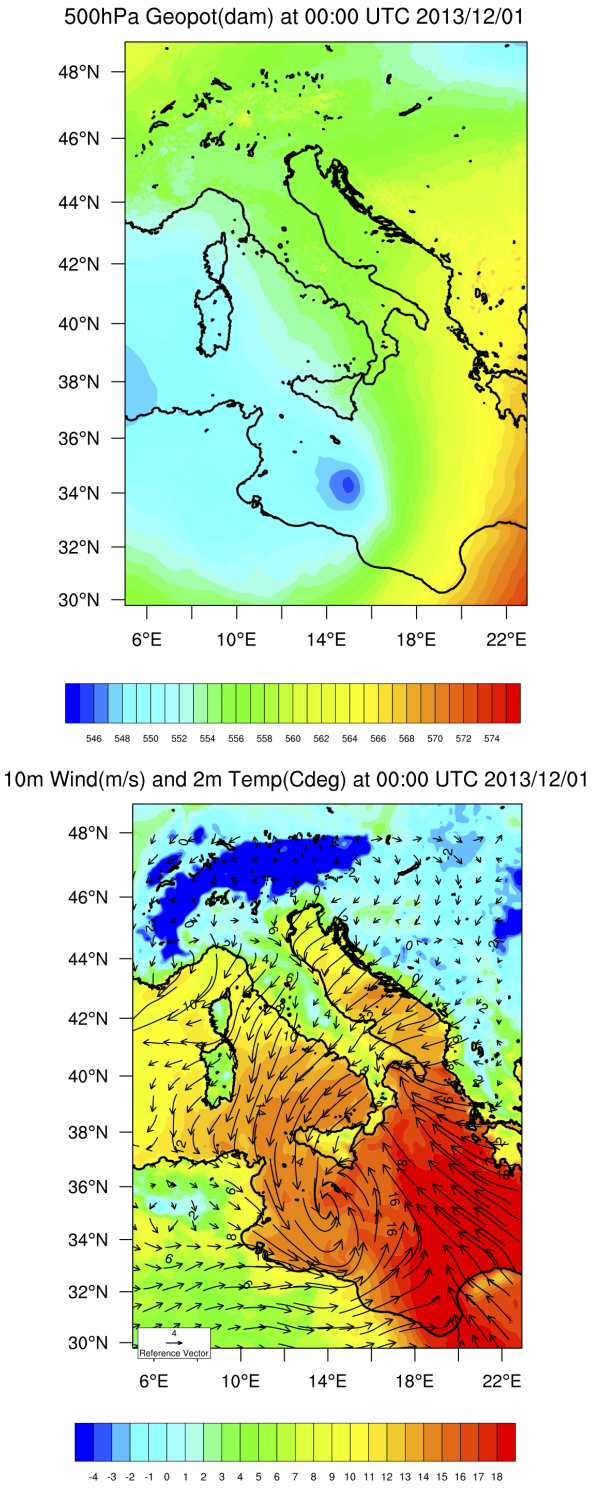

Figure 3.6: Mesoscale maps during the weather storm on 1 December 2013 (Event 2). Top panel: WRF (domain1) Geopotential height (in m/10, colours) at 500hPa. Bottom panel: WRF (domain1) 2m Temperature (in Cdeg, colours) and 10m wind (in m/s, black arrows)

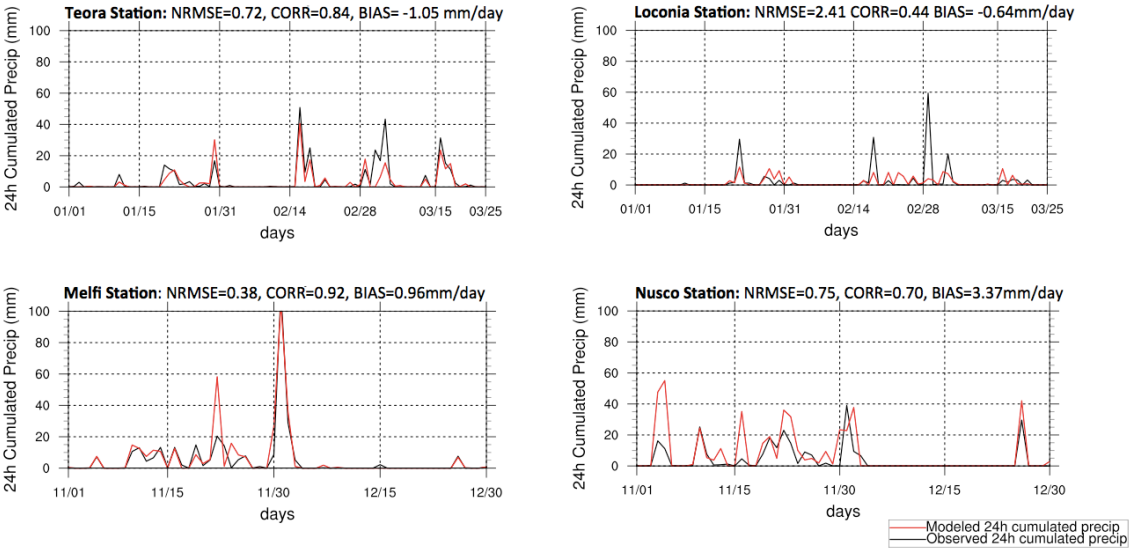

Figure 3.7: Validation of the hourly modeled precipitation through the entire simulation period in the Ofanto basin. Top Panels: observed and modelled time series at the stations with the best (left) and the worse (right) WRF performance for Experiment 1. Bottom Panels: observed and modelled time series at the stations with the best (left) and the worse (right) WRF performance for Experiment 2

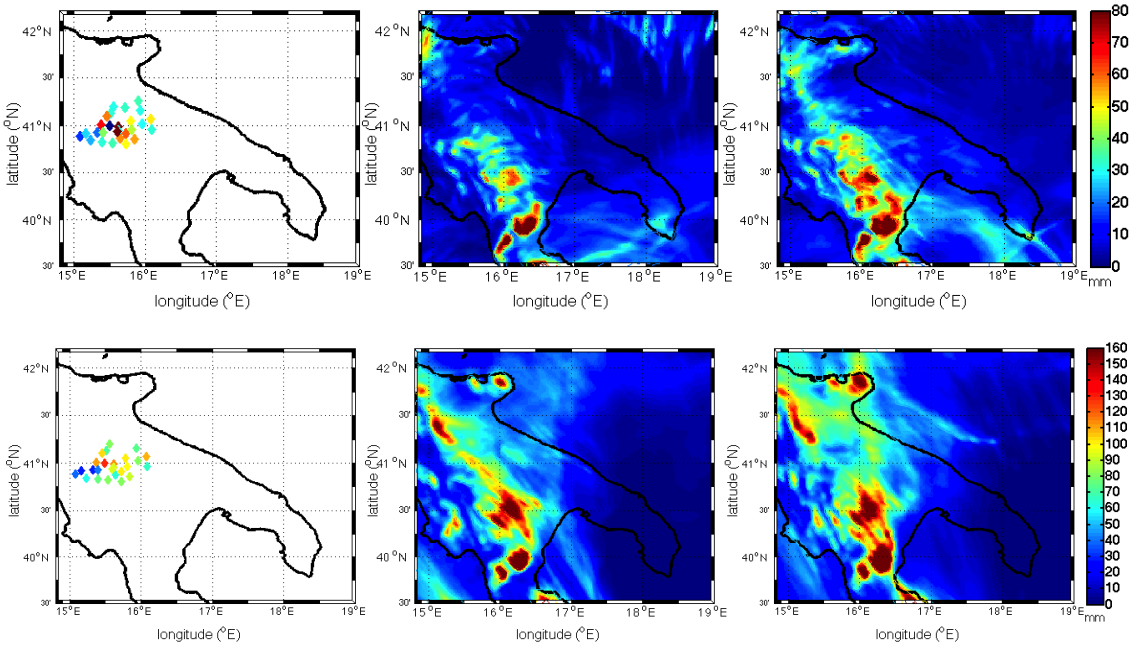

Figure 3.8: Upper panels: Comparison of 24h cumulated precipitation on 2011/02/18 as recorded by 27 gauge-stations (left panel), modelled by WRF with start time 14h before the rain peak (middle panel) and modelled by WRF with start time 38h before the rain peak (right panel). Lower panels: Comparison of 24h cumulated precipitation on 2013/12/01 as recorded by 25 gauge-stations (left panel), modelled by WRF with start time 12h before the rain peak (middle panel) and modelled by WRF with start time 36h before the rain peak (right panel)

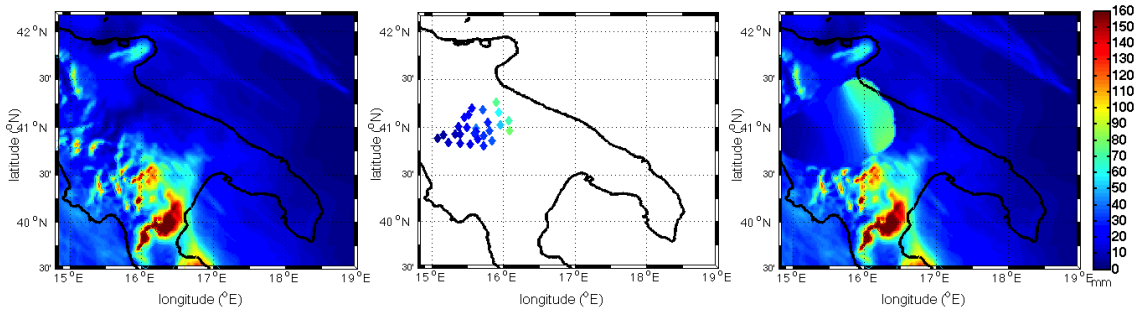

Figure 3.9: Maps of 24h cumulated precipitations (in mm/day, colours) during the peak event on March, 1^{st} 2011. Left panel: model findings (left), Middle panel: 27 observed spots used for applying the Barnes method, Right panel: model findings corrected with Barnes scheme

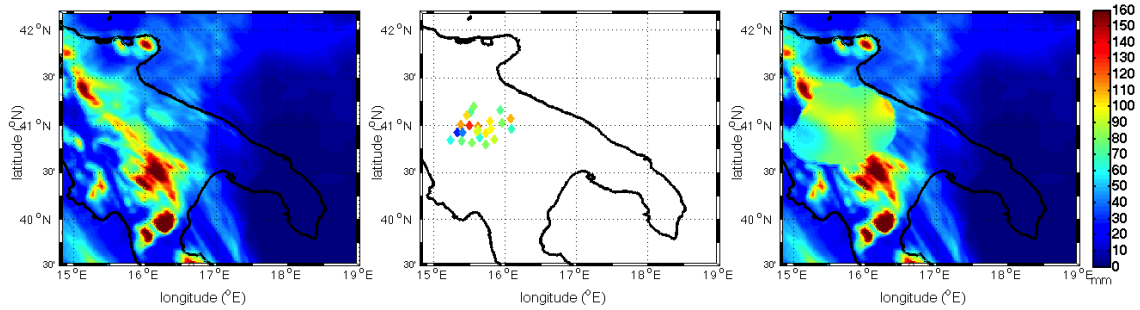

Figure 3.10: Maps of 24h cumulated precipitations (in mm/day, colours) during the peak event on December, 1^{st} 2013. Left panel: model findings (left), Middle panel: 23 observed spots used for applying the Barnes method, Right panel: model findings corrected with Barnes scheme

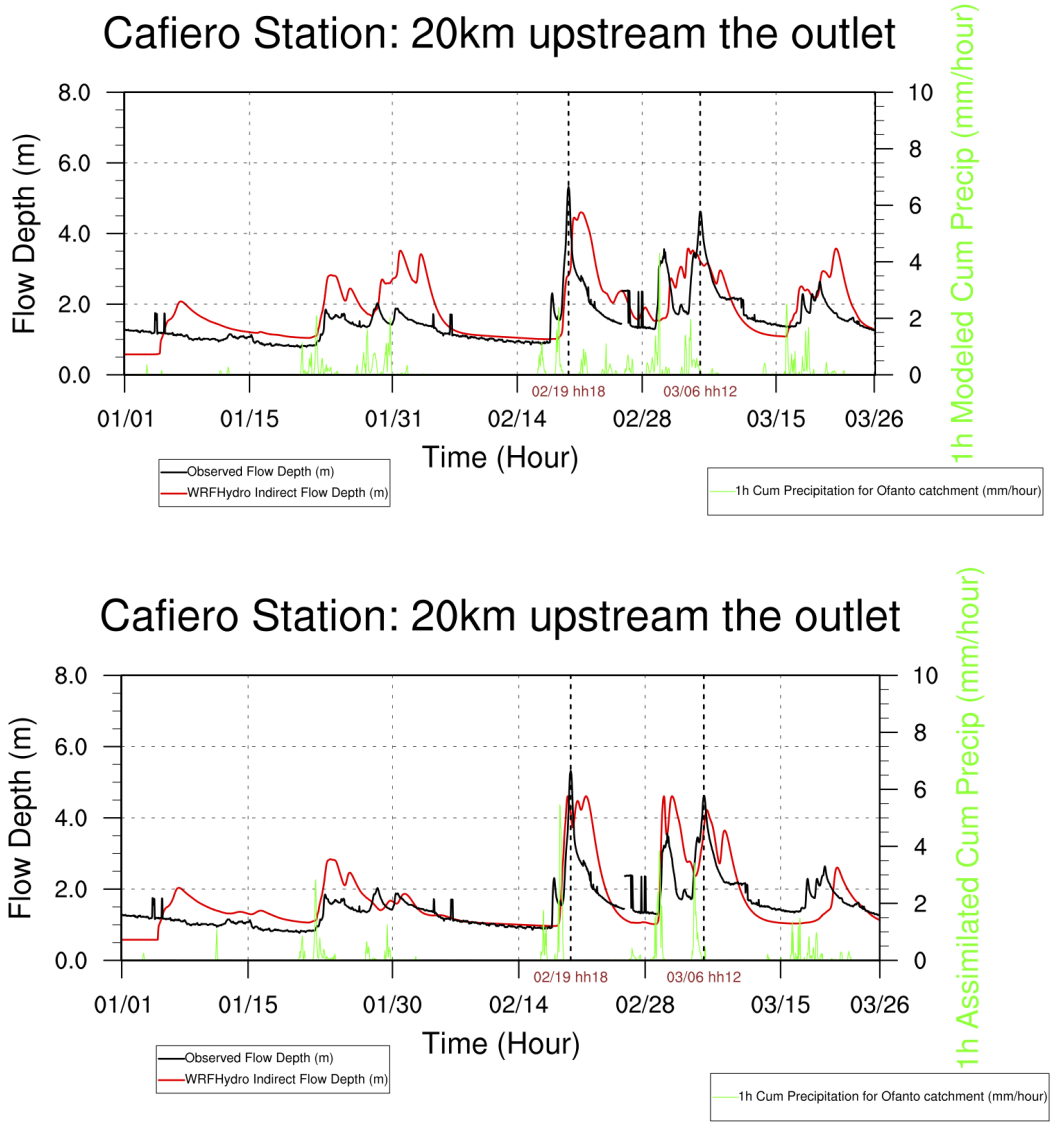

Figure 3.11: Validation of Ofanto discharge for Experiment 1 at Cafiero Station. Top panel: modelled precipitation, aquifer switched on, calibration of NOAH and WRF-Hydro coefficients (discharge RMSE =0.75m , CORR=0.66). Bottom panel: assimilated precipitation, aquifer switched on, calibration of NOAH and WRF-Hydro coefficients (discharge RMSE = 0.65m, CORR=0.74)

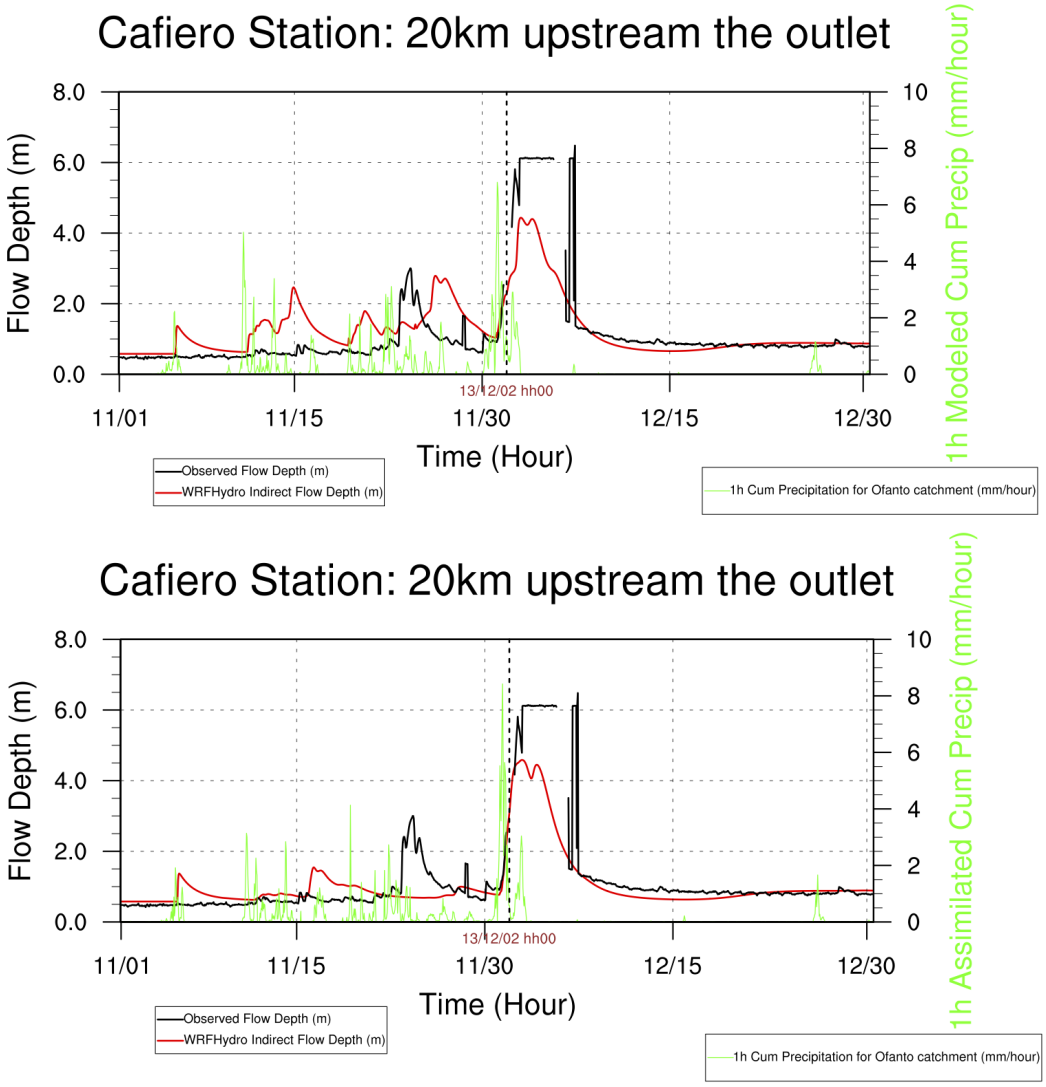

Figure 3.12: Validation of Ofanto discharge for Experiment 2 at Cafiero Station. Top panel: modelled precipitation, aquifer switched on, calibration of NOAH and WRF-Hydro coefficients (discharge RMSE= 0.82m, CORR=0.81). Bottom panel: assimilated precipitation, aquifer switched on, calibration of NOAH and WRF-Hydro coefficients (discharge RMSE=0.74m, CORR=0.88)

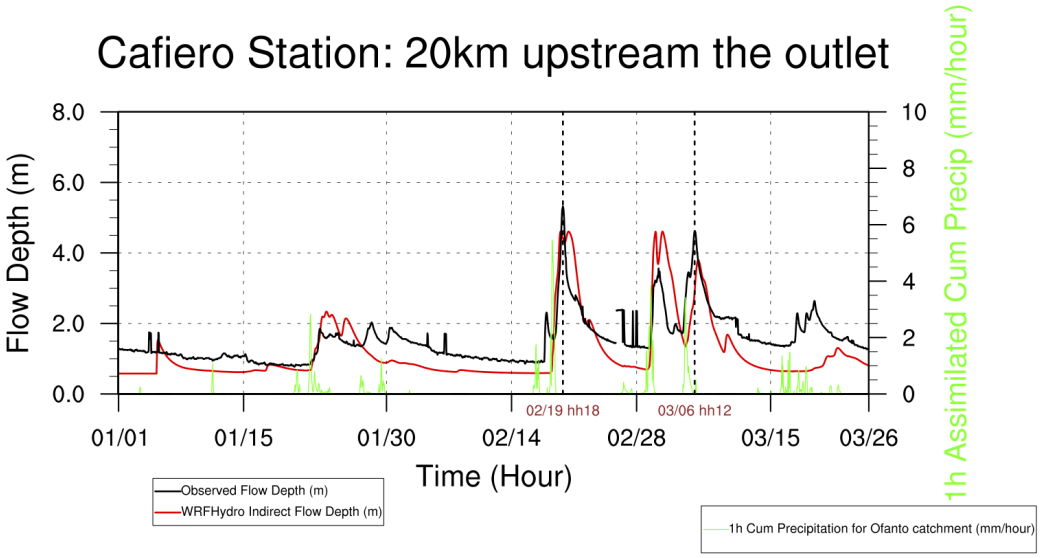

Figure 3.13: Validation of Ofanto discharge for Experiment 1 at Cafiero Station working with assimilated precipitation, calibration of NOAH and WRF-Hydro coefficients but aquifer switched off (discharge RMSE= 0.69m, CORR=0.77)

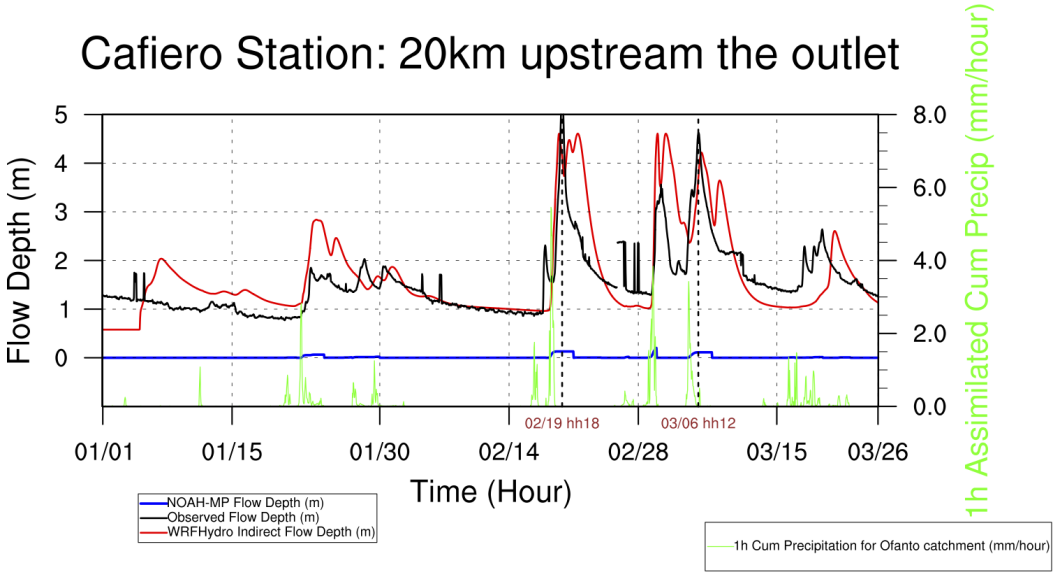

Figure 3.14: Comparison of Ofanto discharge for Experiment 1 at Cafiero Station as provided by the best WRF-Hydro set-up (discharge RMSE= 0.65 m, CORR=0.74) and by NOAH-MP (discharge RMSE= 1.68 m, CORR=0.61)

Experiment	Time Window	Date of severe Events	Start time of WRF 72h Run for Events 1-2	Max recorded value of 24h cumulated precipitation
Experiment 1	Jan-Mar 2011	1 March 2011 (Event 1)	27 February 2011 00 UTC	186.9 mm/day
Experiment 2	Nov-Dec 2013	1 December 2013 (Event 2)	1 December 2013 00 UTC	189.6 mm/day

Table 3.1: Details on the Experiments

WRF ARW SET-UP	DOMAIN 1	DOMAIN 2
Topography	SRTM 90m	EUDEM 30m
Land Use categories	USGS 800m + Corine 250m (Europe)	Corine 250m
Radiation	RRTMG (2008)	RRTMG (2008)
PBL surface sub-layer	Monin-Obukhov (1954)	Monin-Obukhov (1954)
PBL mixed sub-layer	YUS (2006)	YUS (2006)
Convection	Kain-Fritsch (1993)	Explicit
Microphysics	Thompson (2004)	Thompson (2004)

Table 3.2: Terrestrial datasets and parameterization settings adopted over WRF Domain 1 (6 km grid spacing) and Domain 2 (2 km grid spacing)

Statistical index of precipitation	Experiment 1	Experiment 2
$NRMSE_{ave}$	1.15	0.59
$BIAS_{ave}$ (mm/day)	+0.11	+0.45
$CORR_{ave}$	0.70	0.86

Table 3.3: Statistical indices for validation of modeled precipitation by comparison with rain-gauge stations in the Ofanto basin during the entire simulation period

Tuned Coefficient	Experiment 1	Experiment 2
SLOPE - Class 2	0.2	0.2
REFKDT (m^3/m^3)	0.1	0.7
SMCMAX - ClayLoam (m^3/m^3)	0.232	0.465

Table 3.4: Tuned coefficients of WRF-Hydro/NOAH-MP for both Experiments

Tuned Coefficient	Sub-basin1	Sub-basins 2-3-4
$Z_{ini}(mm)$	0.0450	0.0036
$Z_{max}(mm)$	2.00	5.55
α	1.861	0.861
C ($m^3 s^{-1}$)	0.014	0.0014

Table 3.5: Tuned coefficients of WRF-Hydro-aquifer model for each Ofanto river sub-basin

4 The physical regime of $ROFI_S$

Preamble

This chapter is a co-authored paper with N. Pinardi, J. Tribbia, F. Bryan, Y. Tseng, Q. Sun and G. Coppini, entitled "Estuarine dynamics for ocean modeling: the case study of the Ofanto estuary" and to be submitted to the Journal of Physical Oceanography.

The regional ocean models generally treat the riverine freshwater release in a oversimplified way by means of climatological runoff, based on gauges located far from river outlets, and zero or at most constant salinity values corresponding to the runoff. Thus the water exchange into the estuaries, owing to to the ocean water entrainment, is not taken into account. We consider the highly stratified estuary of the Ofanto river as case study and we aim to describe the main physical processes involved in the water and energy balance of the estuary.

Three approaches of estuarine dynamics are tested and compared: the simple Knudsen's relation, an upgraded version of the Knudsen's relation we developed with the addition of tides, and an estuary box model developed by the University of Connecticut and the National Center for Atmospheric Research. A set of sensitivity experiments has been performed in the ROFI of the Ofanto river by forcing the regional ocean model with the runoff and salinity computed by the different approaches of the estuarine dynamics. We found that the added value of better representing the estuarine dynamics and its effect on the coastal dynamics becomes particularly clear during the upwelling wind regime in the Puglia region. The UCONN-NCAR model is the only one which is capable to represent a well defined river plume during upwelling wind. On the other hand, the estuary model based on the Knudsen's relation with the addition of tides is the most rigorous one from the theoretical point of view, thus future efforts will be devoted to the development of this new approach.

4.1 Introduction

Several modelling and theoretical studies have pointed out rivers play a crucial role on the overturning circulation of both shelf area (Simpson et al, 1993; Kourafalou et al, 1996; Kourafalou, 1999; Schiller and Kourafalou, 2010) and open ocean (Rahmstorf, 1995; Skliris et al., 2007; Somot et al., 2006; Spall, 2012). The investigations carried out on the shelf areas adjacent to estuaries, the so called Regions Of Freshwater Influence (i.e. $ROFI_s$), highlighted the riverine freshwater discharge generated baroclinic dynamics by promoting the water column stratification and the offshore drift (Chapman and Beardsley, 1989; Garvine, 1999). The resulting dynamical structure is the "buoyant river plume" which consists of an offshore cyclostrophic bulge which turns anticyclonically plus a coastal alongshore current due to the geostrophic adjustment.

A key issue which is still poorly investigated is that the net freshwater release at river mouth is a non-zero salinity outflow (MacCready and Geyer, 2010) as consequence of the ocean water entering the river mouth. The tidal pumping plays the predominant role in the exchange of fresher water leaving the estuary (ebb tide) and saltier ocean water entering the estuary (flood tide).

The regional ocean models based on finite difference grids cannot solve the estuary dynamics due to their numerical constraints. Moreover they are usually forced at river outlets by freshwater volume fluxes based on climatologies and zero at most constant salinity values. We point to overcome this shortcoming and introduce a reasonable river discharge into regional ocean models, thus different approaches of estuary dynamics are here evaluated: the simplest method based on Knudsen's relation (Knudsen, 1900), an upgraded method we developed for including the tidal pumping into the Knudsen's relation and finally a 2-layer steady state estuary box model developed by UCONN and NCAR (Garvine and Whitney, 2006; MacCready and Geyer, 2010). The different methods are described in Section2 and their application to a case study, i.e. the estuary of the Ofanto river, is presented in Section 3. Section 4 deals with the coupling of the estuary dynamics methods with a regional ocean model. Summary and conclusions are provided in Section 5.

4.2 Estuarine dynamics: the theory

The estuary region is here assumed to be a two-layer rectangular box as drawn in Figure 4.1. The two layers have constant thickness $H/2$, length L_x, width L_y and vertically uniform features. The estuary mouth is defined as the origin of the x-axis which is positive toward the ocean. The origin of the z-axis is at the bottom of the box and upward oriented. We define the estuary head as the last point along the river network moving downstream with salinity still equal to zero, thus not affected by the ocean water entrainment. We assume the heat flux, the freshwater flux and the wind stress at the top surface and the infiltration at the bottom are negligible at the scales of the estuary box. Thus the horizontal boundaries at the top and the bottom are closed. The vertical boundary at the estuary mouth is open through both layers while the vertical boundary at the estuary head is open only through the upper layer.

The drawing of a two layer estuary box design is fully consistent with estuaries classified as "highly stratified estuaries" (Fischer et al., 1979), a deeper study should be devoted to the cases of "well-mixed estuaries".

The Knudsen's relation The Knudsen's relation describes the estuarine circulation by means of 2 diagnostic equations: the volume conservation equation (units of m^3/s) and the salt conservation equation (units of $psu * m^3/s$).

The volume conservation equation is given by:

$$Q_{ul}^{ebm} = Q_{river} + Q_{ll}^{ocean} \tag{4.1}$$

The salt conservation equation is equal to:

$$S_{ul}^{ebm} Q_{ul}^{ebm} = S_{ll}^{ocean} Q_{ll}^{ocean} \tag{4.2}$$

The subscript "*river*" stands for the riverine variable at the head, the subscript "*ll*" indicates the lower layer variables and the subscript "*ul*" the upper layer variables. The outflowing volume flux of estuarine water through the upper layer, Q_{ul}^{ebm}, and the salinity of outflowing water, S_{ul}^{ebm}, are the unknowns while the river volume flux at the estuary head, Q_{river}, the salinity of inflowing ocean water through the lower layer, S_{ll}^{ocean}, and the volume flux of inflowing ocean water,

Q_{ll}^{ocean}, are provided as input forcings. The sketch of the input forcings and unknowns is given in Figure 4.2.

The volume conservation of eq.(4.1) is derived starting from the continuity equation for incompressible fluid while the salt conservation of eq.(4.2) is constructed starting from the advection/diffusion equation for salinity.

The estuary length, L_x is the only tunable coefficient. This is not involved in the model equations but enables to define the estuary head where Q_{river} is provided. Knudsen's relation is definitely a coarse approach which describes only three physical processes: the riverine discharge inflowing at the estuary head, the ocean water flux inflowing at the estuary mouth through the lower layer, the estuarine water flux outflowing at the mouth through the upper layer.

4.2.1 The development of new approach: the Knudsen's relation upgraded with the tidal effect

We upgrade the Knudsen's relation by including the tidal pumping term into the conservation equations (4.1)-(4.2). Additional input forcings with respect to Knudsen's relation are the ocean water mean salinity $\overline{S}_{ocean}$, the level h and the temporal gradient $\frac{\partial h}{\partial t}$ at the estuary outlet. The details of the model are drawn in Figure 4.3.

The conservation equations read:

$$Q_{ul}^{ebm} = Q_{river} + Q_{ll}^{ocean} + HL_xL_y\big(\frac{\partial h}{\partial t}\big)/h \tag{4.3}$$

$$S_{ul}^{ebm}Q_{ul}^{ebm} = S_{ll}^{ocean}Q_{ll}^{ocean} + H\overline{S}_{ocean}L_xL_y\big(\frac{\partial h}{\partial t}\big)/h \tag{4.4}$$

We demonstrated the eq.(4.3) starting from the continuity equation for incompressible fluid:

$$\bigtriangledown \cdot \vec{u} = 0 \tag{4.5}$$

We consider the volume integral in order to apply the divergence theorem:

$$\int\int\int_V \bigtriangledown \cdot (\vec{u}) = \int\int_S \vec{u} \cdot dS\hat{n} = 0 \tag{4.6}$$

In our set-up, the faces of the estuary box are closed except the two cross sections in the direction of river streamflow, $i.e. \hat{n} = \hat{x}$, and thus we consider only the fluxes through these boundaries at the estuary head and mouth:

$$\int_{H/2}^{H}\int_{dy} \vec{u}_{ul}^{ebm} \cdot \hat{n} dz dy - \int_{H/2}^{H}\int_{dy} \vec{u}_{river} \cdot \hat{n} dz dy + \\ - \int_{0}^{H/2}\int_{dy} \vec{u}_{ll}^{ocean} \cdot \hat{n} dz dy - \int_{0}^{H}\int_{dy} \vec{u}_{ocean}^{baro} \cdot \hat{n} dz dy \Big|_{x=0} = 0 \tag{4.7}$$

where $\vec{u}_{ocean}^{baro} = \vec{u}_{ocean}^{baro}(x, y, t)$ is the barotropic ocean velocity we consider at the estuary mouth, $x = 0$. This is essentially due to tides, thus $\vec{u}_{ocean}^{baro} \cdot \hat{n} = u_{tide}$ is the horizontal component in the streamflow direction $\hat{x}$, which is positive defined if offshore oriented following the x-axis orientation. By considering the geometry of the estuary box we get:

$$Q_{ul}^{ebm} - Q_{river} - Q_{ll}^{ocean} - H \int_{dy} u_{tide} dy \Big|_{x=0} = 0 \tag{4.8}$$

The last term on the LHS of eq.(4.8) is computed starting from the equation for the sea surface height:

$$\frac{\partial h}{\partial t} + \bigtriangledown_H \cdot (h\vec{u}_{baro}) = \cancel{P + R - E} \tag{4.9}$$

where $h(x, y, t) = H + \eta(x, y, t)$ is the sea surface height, moreover the surface freshwater flux is neglected over the estuary area.

The surface integral over the estuary horizontal area reads:

$$\int\int \frac{\partial h}{\partial t} dx dy + \int\int \bigtriangledown_H \cdot (h\vec{u}_{baro}) dx dy = 0 \tag{4.10}$$

By applying the Green's theorem:

$$\int\int \bigtriangledown_H \cdot (h\vec{u}_{baro}) dx dy = \oint h\vec{u}_{baro} \cdot \hat{n} dl \tag{4.11}$$

By replacing (4.11) into (4.10) we get:

$$\int_0^{L_y}\int_0^{-L_x} \frac{\partial h}{\partial t} dx dy + \oint (h u_{tide} dy - h v_{tide} dx) = 0 \tag{4.12}$$

We consider the estuary motion is one-dimensional thus at the estuary head we get $v_{tide} = 0$ and $h = h(t)$. The equation (4.12) can be rewritten as follows:

$$\int_0^{L_y} u_{tide} dy \Big|_{x=0} = -(-L_x) L_y (\frac{\partial h}{\partial t})/h \tag{4.13}$$

By replacing eq.(4.13) in eq.(4.8), we finally get eq.(4.3).

The salt conservation of eq.(4.4) can be constructed starting from the advection/diffusion equation for salinity:

$$\cancel{\frac{\partial S}{\partial t}} + \bigtriangledown \cdot (\vec{u}S) = \cancel{K_{S_H} \bigtriangledown^2 S} + K_{S_V} \frac{\partial^2 S}{\partial^2 z} \tag{4.14}$$

where K_{S_H} and K_{S_V} are the horizontal and vertical diffusive coefficients (units of $m^2 s^{-1}$).

The local variation term is null since the fluid is steady and we neglect the horizontal mixing term. The volume integral reads:

$$\int\int\int_V \bigtriangledown \cdot (\vec{u}S) = \cancel{\int\int\int_V K_{S_V} \frac{\partial^2 S}{\partial^2 z}} \tag{4.15}$$

where the hypothesis of zero surface freshwater flux, $E - P - R$, at the estuary top surface implies the volume integrated vertical mixing term is null.

We apply the divergence theorem as done for the volume conservation in eq.(4.6), thus obtaining:

$$\begin{aligned} &\int_{H/2}^{H}\int_{dy} u_{ul}^{ebm} S_{ul}^{ebm} \cdot \hat{n} dz dy - \cancel{\int_{H/2}^{H}\int_{dy} \vec{u}_{river} S_{river} \cdot \hat{n} dz dy} + \\ &- \int_0^{H/2}\int_{dy} \vec{u}_{ll}^{ocean} S_{ll}^{ocean} \cdot \hat{n} dz dy - \int_0^{H}\int_{dy} \overline{S}_{ocean} \vec{u}_{ocean}^{baro} \cdot \hat{n} dz dy \Big|_{x=0} = 0 \end{aligned} \tag{4.16}$$

where the second term on the LHS is null owing to $S_{river} = 0$. By replacing the volume fluxes Q_{ul}^{ebm} and Q_{ll}^{ocean} and $\vec{u}_{ocean}^{baro} \cdot \hat{n} = u_{tide}$ we get:

$$S_{ul}^{ebm} Q_{ul}^{ebm} - S_{ll}^{ocean} Q_{ll}^{ocean} - H \overline{S}_{ocean} \int_{dy} u_{tide} dy \Big|_{x=0} = 0 \tag{4.17}$$

and by writing the last term on the LHS as demonstrated in eq.(4.13) we finally get eq.(4.4).

4.2.2 The UCONN-NCAR estuary box model

A 2-layer steady state estuary box model has been developed by UCONN and NCAR and is based on the assumptions of rigid lid, steady fluid and hydrostatic equilibrium. The described physical processes are the riverine water inflow at

the estuary head, the ocean water inflow the lower layer at the estuary mouth, the estuarine water outflow the upper layer at the mouth, the tidal pumping over a whole tidal cycle including both flood tide (inflowing ocean water) and ebb tide (outflowing estuarine water), the tidal mixing at the bottom and the shear mixing at layer interface. A sketch of the model is given in Figure 4.4.
The numerical core consists of three steady-state and tidal cycle-averaged equations for water mass conservation (kg/s), salt mass conservation (kg*psu/s) and potential energy flux conservation (J/s), plus a linear state equation of the sea water.

$$\rho_{ll}^{ocean} Q_{ll}^{ocean} + (\rho_{ll}^{ocean} - \rho_{ul}^{ebm}) m_{tides} Q_{ul}^{tides}/2 + \rho_{river} Q_{river} - \rho_{ul}^{ebm} Q_{ul}^{ebm} = 0 \quad (4.18)$$

$$S_{ll}^{ocean} \rho_{ll}^{ocean} Q_{ll}^{ocean} + (S_{ll}^{ocean} \rho_{ll}^{ocean} - S_{ul}^{ebm} \rho_{ul}^{ebm}) m_{tides} Q_{ul}^{tides}/2 - S_{ul}^{ebm} \rho_{ul}^{ebm} Q_{ul}^{ebm} = 0 \quad (4.19)$$

$$PEF_{ll} + PEF_{tp} + PEF_{river} + PEF_{tm} + PEF_{sm} - PEF_{ul} = 0 \quad (4.20)$$

The subscripts "tp" and "tm" mean tidal pumping and tidal mixing respectively. The subscript "sm" represents the shear mixing term. Q_{ul}^{tides} is the tidal volume flux over the ebb tide through the upper layer, m_{tides} is the ratio between the areas of advected volumes during ebb or flood tide.
A simplified linear equation of sea water state computes the density from the salinity and is given by:

$$\rho = \rho_0 (1 + k_s S) \quad (4.21)$$

where $k_s = 7.7 * 10^{-4} psu^{-1}$ (Garvine, 1999) and $\rho_0 = 1000 kg/m^3$ is the fresh-water reference density, thus $\rho_{river} = \rho_0$ while $\rho_{ll}^{ocean} = \rho_0 (1 + k_s S_{ll}^{ocean})$ and $\rho_{ul}^{ebm} = \rho_0 (1 + k_s S_{ul}^{ebm})$.
The outflowing volume flux of estuarine water through the upper layer, Q_{ul}^{ebm}, the salinity of outflowing water, S_{ul}^{ebm} and the volume flux of inflowing ocean water

through the lower layer, Q_{ll}^{ocean}, are the model unknowns while the river volume flux at the estuary head, Q_{river} and the salinity of inflowing ocean water through the lower layer, S_{ll}^{ocean} are provided as input forcings.

Moreover this model includes several tunable coefficients: the estuary length, L_x, the tidal period, T, the tidal amplitude a_{tide}, the bottom drag coefficient, C_d, the tidal mixing efficiency, ϵ, the shear mixing efficiency, γ, and the entrainment constant at layer interface, α.

The tidal pumping implies a net increase of water mass, salt mass and potential energy flux into the estuary over a whole tidal cycle. In details the model assumes the volumes advected through the mouth during flood tide and ebb tide are equal, but the flood tide effect prevails on the ebb tide one owing to the density difference between the advected volumes (see the positive second term on the LHS of eq_s(4.18)-(4.19)-(4.20)). The tidal volume flux over the ebb tide through the upper layer, Q_{ul}^{tides}, is computed by solving a 1d linearised shallow water system in the entrainment zone off the estuary, thus we get $Q_{ul}^{tides} = L_y \frac{H}{2} \frac{2u_{tide}}{\pi} = L_y \frac{H}{2} \frac{2a_{tide}\sqrt{gH}}{H\pi} = \frac{L_Y L_T H/2}{T}$ where T is the tidal period and L_T is the length of the ebb tide excursion. The water mass flux resealed during ebb is given by $WM_{ebb} = \rho_{ul}^{ebm} Q_{ul}^{tides}$, the water mass flux gained during flood is computed starting from Q_{ul}^{tides} with an empirical approach.

The equations for water mass conservation (4.18) is derived from the continuity differential equation with the hypothesis of steady fluid.

The salt mass conservation equation (4.19) is written as the water mass conservation simply multiplying each term by the salinity of the water masses. We believe this is a limit of the model since the salt conservation equation should be strictly derived from the advection/diffusion equation for salinity and this is the main reason why we decide to write the new set of equations (4.3)-(4.4).

The steady-state potential energy flux conservation equation (4.20) is written under the hydrostatic hypothesis which enables to get the gravitational potential energy per unit area (unit of J/m^2) as $PE = \int_0^H \rho g z dz = \frac{1}{2}\rho g H^2$. The potential energy flux for the process i, PEF_i (units of Js^{-1}), is thus given by $PEF_i = \frac{PE}{H} Q = \frac{1}{2}\rho g H Q_i$.

Further details on the computation of Q_{ul}^{tides}, PEF_{tp}, PEF_{tm} and PEF_{sm} on

empirical basis are provided in Qiang, S., et al., A Box Model for Representing Estuarine Physical Processes in Earth System Models, private communication. Figure 4.5 summarises the main features of the estuary dynamics approaches we tested. By comparing the approaches from a theoretical point of view, the UCONN-NCAR model is capable to solve the highest number of physical processes including also the tidal mixing and the shear mixing. On the other hand the model we developed on the basis of Knudsen's relation with the addition of the tidal pumping consists of fully justified equations. Moreover the inflowing volume flux of ocean water through the bottom is an input forcing instead of an unknown as in UCONN-NCAR model and this is expected to be a more realistic approach. Finally no tunable coefficients are involved in the equations, thus reducing the uncertainties associated with the calibration of these coefficients. For these reasons we argue the estuary model based on Knudsen's relation with the addition of tides is the most rigorous from the theoretical point of view. The next step is to compare the performance of the different approaches in a real case study.

4.3 Application: the estuarine dynamics of the Ofanto river

We chose the estuary of the Ofanto river as case study. The main features of the Ofanto basin are detailed in Chapter 3. We selected the time window over January-March 2011 which is characterised by high discharge of the river and 2 flooding events well captured by our meteo-hydrological chain (Chapter 3). We estimated the Ofanto estuary "flow ratio", defined as the tidal velocity over the river streamflow velocity (Fischer et al. 1979), over the simulation period:

$$flow\ ratio = \overline{u}_{tide}/\overline{u}_{river} = 0.01 \tag{4.22}$$

where the tidal velocity at the river mouth, $\overline{u}_{tide}$, is given by OTPS (Oregon State University Tidal Prediction Software, Egbert and Erofeeva, 2002) and the river streamflow velocity at the estuary head, $\overline{u}_{river}$, is provided by WRF-Hydro. Following Fischer (1979), a flow ratio minor than 0.1 suggests the estuary is

a "sharply stratified" estuary. A fully stratified estuary is expected to release the volume flux through the upper layer and satisfies the Richardson's number criteria, thus cannot become unstratified and a high mixing is proved to be at most an intermittent process occurring in the late ebb-tide phase (Geyer and Smith, 1987). This means the 2-layer estuary box is fully consistent with the Ofanto estuary.

The geometry of the Ofanto estuary has been set up. The estuary width, $L_y = 25m$, has been measured by Google Earth. The estuary height, $H = 5m$, has been assumed equal to the minimum depth of our regional ocean model bathymetry. The estuary length, $L_x = 1km$, is based on comparisons with other case studies (Tseng et al., 2016 in revision) since we cannot rely on in-situ observations. For what concern the only UCONN-NCAR model, the tidal characteristics at the mouth, T and a_{tide}, have been extracted from Guarnieri et al, 2013 according to the tide-gauge station offshore of Bari. The coefficients C_d and α are set to literature-based values and the efficiencies ϵ and γ are still equal to the default values.

We coupled the estuary box model with WRF-Hydro model (details are in Chapter 3) at the head and with NEMO ocean model (details are in Chapter 2) and OTPS at the outlet. All the couplings are in 1-way mode. Thus Q_{river} is provided by the WRF-Hydro model, $\overline{S}_{ocean}$, S_{ll}^{ocean} and Q_{ll}^{ocean} (with the only exception of UCONN-NCAR model assuming Q_{ll}^{ocean} as an unknown) are passed by NEMO, h is provided by OTPS. The frequency of input forcings is hourly.

To note that Q_{ll}^{ocean} is computed as $Q_{ll}^{ocean} = u_{ll}^{ocean} * L_y * H$ where u_{ll}^{ocean} is the weighted average of ocean velocity values at the NEMO grid points closest to the lower layer at the river outlet and is assumed zero if seaward oriented. Similarly h is provided by OTPS by selecting the model grid point closest to the river mouth, $\frac{\partial h}{\partial t}$ is then computed from h and put equal to zero if negative, $\frac{\partial h}{\partial t} < 0$.

Figure 4.6 show the results of the performed experiments by the different estuary dynamics approaches. The green time-series of both panels in Fig.4.6 show the Ofanto monthly climatological discharge (Raicich, 1996) and the constant salinity value (i.e. 15 psu) we currently adopt to force out regional ocean model. This is definitely an oversimplified and unrealistic way to force the ocean at the

river outlets.

The results suggest the Knudsen's relation is clearly the coarsest approach: the salinity of outflowing estuarine water often drops to zero (blue time series of bottom panel in Fig.4.6), this could eventually occur over few hours corresponding to the late ebb tide phase but this is definitely unreasonable over several days. The approach we developed by including the tidal pumping into the Knudsen's relation overcomes this deficiency.

The tidal pumping is proved to strongly affect the computation of both salinity and volume flux of the outflowing estuarine water at the estuary mouth. The UCONN-NCAR estuary box model shows the highest values of both salinity and volume flux of the outflowing water. In particular the outflowing volume flux computed by Knudsen and Knudsen+tides approaches doesn't significantly differ from the same field provided by WRF-Hydro at the estuary head, while UCONN-NCAR model shows much higher outflowing volume flux especially during the peak events with subsequent plateaus. We conclude the key forcing mechanism is the tidal pumping which implies the high vertical mixing we observe in the UCONN-NCAR model.

4.4 The coupling with the ocean: the coastal dynamics off the Ofanto estuary

The literature includes several studies which treat the riverine freshwater release into the ocean models as "virtual salt flux boundary condition", also called "mixed boundary condition" (Bryan, 1986): the freshwater flux is prescribed as an additional salt flux which is added to the salt flux boundary condition allowing the concentration-dilution effect to be represented. This is the approach generally assumed in the General Circulation Models, GCM_s, with rigid lid hypothesis. A new approach called "natural boundary condition" (Huang, 1993) fits the free surface ocean models by prescribing the freshwater flux as a volume surplus of zero-salinity water, modeled as a correction to the model's top layer vertical ve-

locity at the grid points covering the source locations. Thus a real freshwater flux is specified through the vertical velocity boundary condition (eq.4.23). Moreover Beron-Vera et al. (1999) introduces a complementary non-zero salt flux at river outlets through ad-hoc salt values in the salt flux boundary condition (eq.4.24). We follow the latter approach, thus rivers are represented as surface point sources of runoff and salinity which affect the ocean model as natural boundary conditions and with ad-hoc salt values at mouths.

The surface boundary condition of our regional ocean model for vertical velocity reads:

$$w \mid_{z=\eta} -\frac{\partial \eta}{\partial t} + (u, v) \mid_{z=\eta} \cdot \bigtriangledown_H \eta = (E - P - \frac{R}{A}) \tag{4.23}$$

The surface boundary condition for salt flux reads:

$$K_t \frac{\partial S}{\partial z} \mid_{z=\eta} = S_{z=\eta}(E - P - \frac{R}{A}) \tag{4.24}$$

where K_t is the vertical mixing coefficient for traces, η is the sea surface elevation, $S_{z=\eta}$ is the surface salinity solved by the ocean model except prescribed ad-hoc salt values at river mouths, E is the evaporation rate (units of ms^{-1}), P is the precipitation rate (units of ms^{-1}), R indicates the river runoff (units of m^3s^{-1}) provided at the model grid points representing river outlets and A stands for the area of river mouth cells.

To note that the other surface boundary conditions of our ocean model for the heat flux and the momentum flux (Appendix A) are also indirectly and slightly affected by river parameterisation since rivers locally lower the sea surface temperature and introduce surface velocity. As detailed in Chapter 2, in the current set-up of our regional ocean model river runoff consists of monthly climatologies for all rivers except daily observations for the Po river and salinity is assumed equal to 15 psu for all rivers and 17 psu for the only Po river, both values are chosen on the basis of sensitivity tests with the latter due to the extensive tidal mixing occurring in the Po delta.

In this study on the estuarine dynamics, we force the ocean model at the Ofanto mouth with the results of the different approaches we tested for representing the estuary dynamics. Doing this a set of sensitivity tests of coastal dynamics off the Ofanto estuary has been carried out. Experiment 1, called "Climatological

runoff", prescribes the Ofanto river freshwater release by means of monthly climatological discharge and constant salinity (15 psu). Experiment 2, called "EBM", predicts the Ofanto freshwater release by using the discharge and salinity time series provided by the UCONN-NCAR model, Experiment 3 called "Knudsen" works with Knudsen's relation results of discharge and salinity. Experiment 4 called "Knudsen+tides" uses the river freshwater release predicted by the new approach we developed by using Knudsen's relation with tides. Finally Experiment 5 called "Explicit Estuary" is based on the Ofanto estuary explicitly solved by NEMO mesh mask. The explicit estuary is forced at the grid cell representing the head of the estuary by the WRF-Hydro discharge and by zero salinity. To note the WRF-Hydro discharge over the simulation period has been validated by comparison with the available observations at Cafiero station (Figure 11 of Chapter 3) and shows a high level of agreement. Thus this experiment is assumed as our benchmark for evaluating the performance of the estuary dynamics approaches.

Figures 4.7-4.8-4.9 show the daily results of the coastal dynamics experiments on February, 19^{th} 2011, when a downwelling favourable wind regime along the western Adriatic coast, i.e. Tramontana, prevails. Similarly Figures 4.10-4.11-4.12 show the same daily results on March, 3^{rd} 2011 when the Scirocco wind blows, promoting the upwelling along the western Adriatic coast. These figures zoom over the coastal region off the Ofanto estuary and the selected fields are the sea surface salinity, the cross shore section of salinity and the surface currents. Figures 4.9 and 4.12 highlight the surface currents are driven by the large scale wind on February, 19^{th} while small-scale patterns prevail on March, 3^{rd}. We found the added value of representing the estuarine dynamics and its impact on the coastal dynamics is clear during upwelling favorable wind regime. Upwelling wind acts in the same direction of the freshwater release by promoting strong offshore spreading and vertical stratification (Chao, S. Y., 1987; Kourafalou et al., 1996).

We aware UCONN-NCAR estuary box model is partially derived on an empirical basis especially for what regards the computation of the tidal pumping term, moreover the salt conservation equation is not rigorously justified. On the other hand this is the only model among the tested ones which is capable to represent a

well defined river plume as compared to the Explicit Estuary approach assumed as our benchmark.

The minimum theoretical value of the plume offshore expansion following Yankowsky and Chapman (1997) reads:

$$y_s = \frac{2\ (3g'H + v_i^2)}{(2g'H + v_i^2)^{1/2}\ f} \tag{4.25}$$

where $g' = g\frac{|\rho_i - \rho_0|}{\rho_0}$ is the reduced gravity based on the density anomaly of the outflowing water, $\rho_i - \rho_0$, with respect to a constant reference density, $\rho_0 = 1000\ kg/m^3$. Moreover H is the mouth depth, v_i is the outflowing velocity, f is the Coriolis parameter.

We apply the eq.(4.25) to the Ofanto plume on daily basis on March 3^{rd} and we get $y_s = 17km$, with $v_i = 0.77m/s$ and $\rho_i = 1001kg/m^3$ computed by using the time series of Q_{ul}^{ebm} and S_{ul}^{ebm} computed by the UCONN-NCAR estuary model. The offshore expansion of the river plume in the top right panel of Fig.4.11 is about $y_s = 14\ km$. Thus there is a good agreement between the theoretical offshore distance of the Ofanto plume and the one simulated by our regional ocean model.

4.5 Summary and concluding remarks

The net freshwater release at river mouths is a non-zero salinity outflow owing to the salt ocean water entrainment and the consequent water exchange into the estuary area. A shortcoming of the regional ocean models is they usually treat the riverine freshwater release in a oversimplified way by means of climatological runoff, mainly based on gauges located far from river outlets, and zero or at most constant salinity.

However rives are known to strongly affect the coastal as well as the open sea overturning circulation thus the main objective of this work is to develop a realistic representation of the riverine freshwater release into our regional ocean model based on finite difference NEMO code.

The modelling of the estuarine dynamics is a challenging topic and is still poorly

investigated.

We tested different approaches for representing the estuarine dynamics: the knudsen's relation which consists of two conservation equations, a new version of the knudsen's relation we developed by including the tidal pumping process and a more complex estuary box model developed by UCONN and NCAR consisting of three conservation equations and representing also the tidal mixing and the shear mixing processes. In all the approaches, we assume the estuary area is a two-layer box with ocean water entering through the lower layer and estuarine water outflowing through the upper layer at the estuary mouth. This is a rigorous approach for well stratified estuary while may be lacking for highly mixed estuaries. The sharply stratified estuary of the Ofanto river has been selected as first case study and the simulations are carried out on January to March 2011, which is a time range characterised by severe weather events with flooding of the river. The estuary box is coupled in 1-way mode with WRF-Hydro model at the estuary head and NEMO ocean model at the estuary mouth.

The Knudsen's relation is proved to be a too simple approach: the salinity of outflowing estuary water often drops to zero, this may actually occurs only over few hours corresponding to the late ebb tide phase but is unreasonable over several days. A new approach we developed by including the tidal pumping process into the Knudsen's relation overcomes this deficiency. We found the tidal pumping strongly affects the resulting salinity of the outflowing estuarine water by promoting an intense mixing into the estuary.

The UCONN-NCAR estuary box model shows the highest values of both salinity and volume flux of the outflowing water. In particular the outflowing volume flux as computed by Knudsen's relation and Knudsen's relation with tides doesn't significantly differ from the same field provided by WRF-Hydro at the estuary head, while UCONN-NCAR model shows much higher outflowing volume flux especially during the peak events.

On the other hand the UCONN-NCAR estuary box model is partially derived on an empirical basis especially for what regards the tidal pumping term and includes several tunable coefficients. Moreover the salt conservation equation

is not rigorously justified. For these reasons we argue the estuary model based on Knudsen's relation with the addition of tides is the most rigorous from the theoretical point of view. A set of coastal dynamics experiments has been carried out in the shelf area off the Ofanto estuary. The ocean model has been forced at the Ofanto outlet with the results of the different approaches we tested for representing the estuarine dynamics: climatological discharge and constant salinity in Experiment 1, the discharge and salinity computed by the Knudsen's relation in Experiment 2, the results of Knudsen's relation with tides in Experiment 3, the UCONN-NCAR findings in Experiment 4. Finally in Experiment 5 the Ofanto estuary is explicitly solved by NEMO mesh mask and forced by zero salinity and the WRF-Hydro time series of discharge at the estuary head.

The added value of representing the estuarine dynamics and its effect on the coastal dynamics becomes particularly clear during the upwelling wind regime. Upwelling favourable winds act in the same direction of the freshwater release by promoting the vertical stratification and the surface offshore spreading, this results in a well defined buoyancy river plume. The coastal dynamics experiment forced by UCONN-NCAR model is the only one which is capable to reproduce a well defined river plume. Moreover this is the closest experiment to the Explicit Estuary approach, which is assumed as our benchmark.

Finally we found a perfect agreement between the theoretical offshore distance of the Ofanto plume we computed following Yankowsky and Chapman (1997) and that one simulated by our regional ocean model. This supports the strength of working with the "natural boundary condition" for representing river release into the ocean.

Future effort will be devoted to a full validation of the estuarine dynamics approaches by selecting time windows with available in-situ and satellite observations. Moreover we plan to assume as the next case study a river with a highly-mixed estuary and flowing into the Norther Adriatic sub-basin where the tidal pumping plays a strong role.

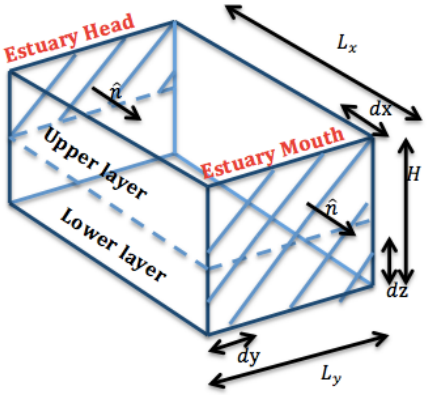

Figure 4.1: The estuary box. Shaded areas are the open boundaries

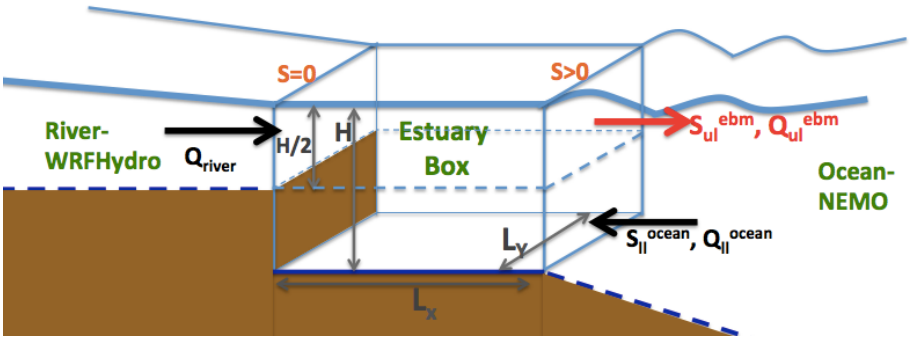

Figure 4.2: Schematic of Knudsen's model, boundaries and water masses involved. Black variables are the input forcings, red variables are the unknowns

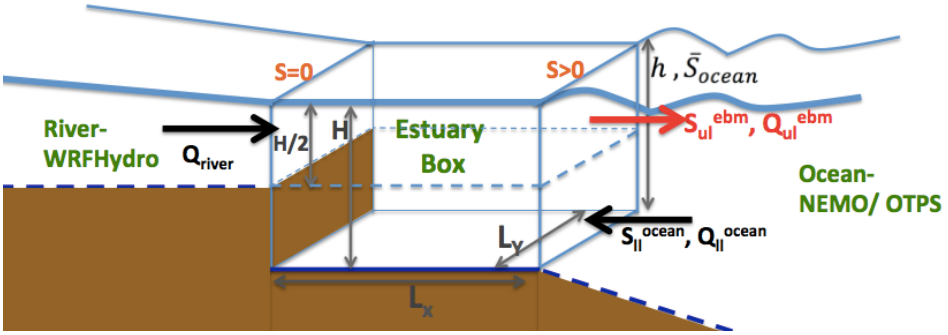

Figure 4.3: Schematic of Knudsen's model with tidal effect added, boundaries and water masses involved. Black variables are the input forcings, red variables are the unknowns

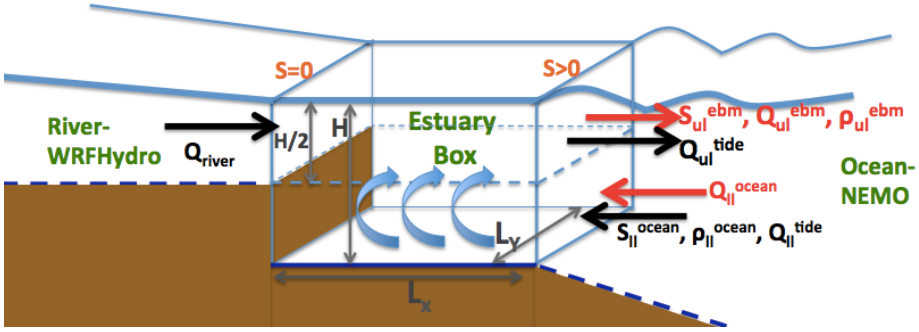

Figure 4.4: Schematic of UCONN-NCAR model with tidal effect added, boundaries and water masses involved. Black variables are the input forcings, red variables are the unknowns

Set-Up	Hypothesis	Physical Processes	Input Variables	Unknowns	Tunable Coefficients
UCONN-NCAR EBM	• Steady fluid (2-layer box) • **Hydrostatic flow** • Rigid lid	• Inflowing river freshwater • Inflowing ocean salt water • Outflowing estuarine water • **Tidal pumping** • **Tidal mixing** • **Shear mixing** ➢ 3 Conservative Equations	• Salinity of inflowing ocean water through lower layer • Volume flux of inflowing river water	• Salinity of outflowing estuarine water • Volume flux of outflowing estuarine water • **Volume flux of inflowing ocean water through lower layer**	• Estuary length • **Tidal period** • **Tidal amplitude** • **Bottom drag coeff** • **Entrainment coeff** • **Tidal mixing coeff** • **Shear mixing coeff**
Knudsen's relation	• **Quasi-Incompressible fluid** • Rigid lid	• Inflowing river freshwater • Inflowing ocean salt water • Outflowing estuarine water ➢ 2 Conservative Equations	• Salinity of inflowing ocean water through lower layer • **Volume flux of inflowing ocean water through lower layer** • Volume flux of inflowing river water	• Salinity of outflowing estuarine water • Volume flux of outflowing estuarine water	• Estuary length*
Knudsen's relation +tides	• **Quasi-Incompressible fluid**	• Inflowing river freshwater • Inflowing ocean salt water • Outflowing estuarine water • **Tidal pumping** ➢ 2 Conservative Equations	• Salinity of inflowing ocean water through lower layer • Volume flux of inflowing ocean water through lower layer • Volume flux of inflowing river water • Ocean SSH and Salinity at river mouth	• Salinity of outflowing estuarine water • Volume flux of outflowing estuarine water	• Estuary length*

(*) not involved into equations but just for locating Estuary Head

Figure 4.5: Features of the tested approaches for representing the estuarine dynamics

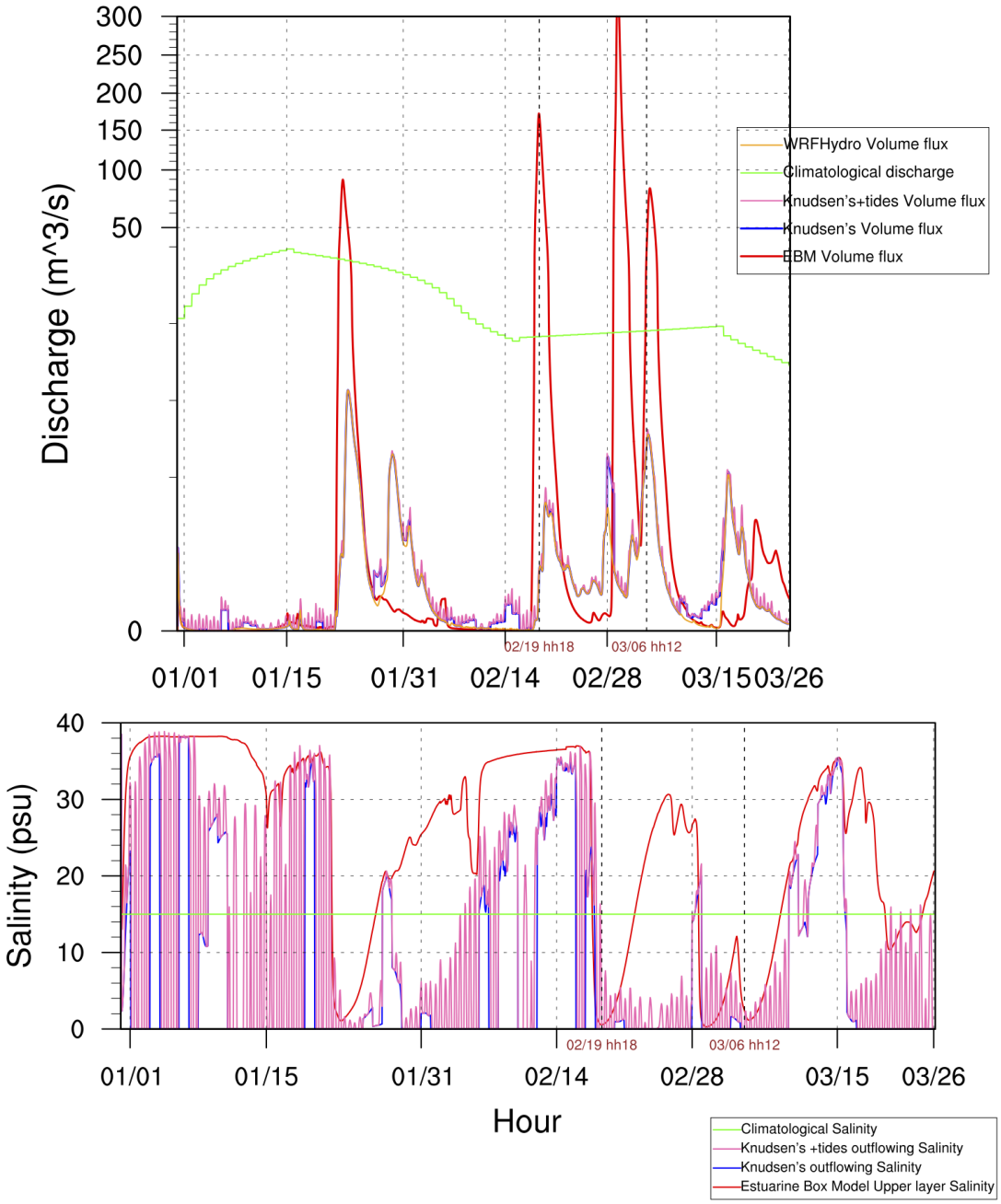

Figure 4.6: Discharge (upper panel) and salinity (lower panel) at the Ofanto river outlet as simulated by the different methods

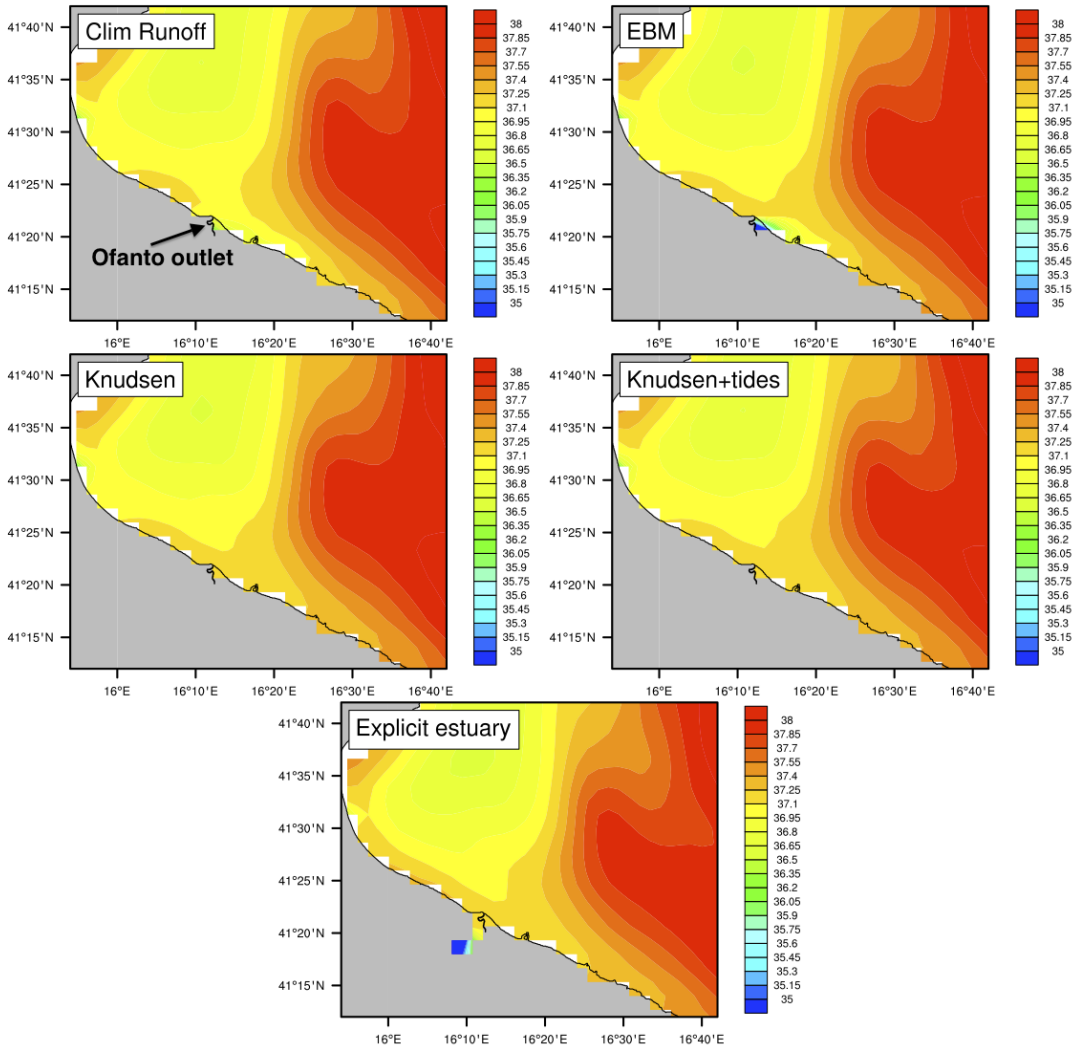

Figure 4.7: Coastal dynamics off the Ofanto estuary. Daily averaged sea surface salinity on 2011/02/19

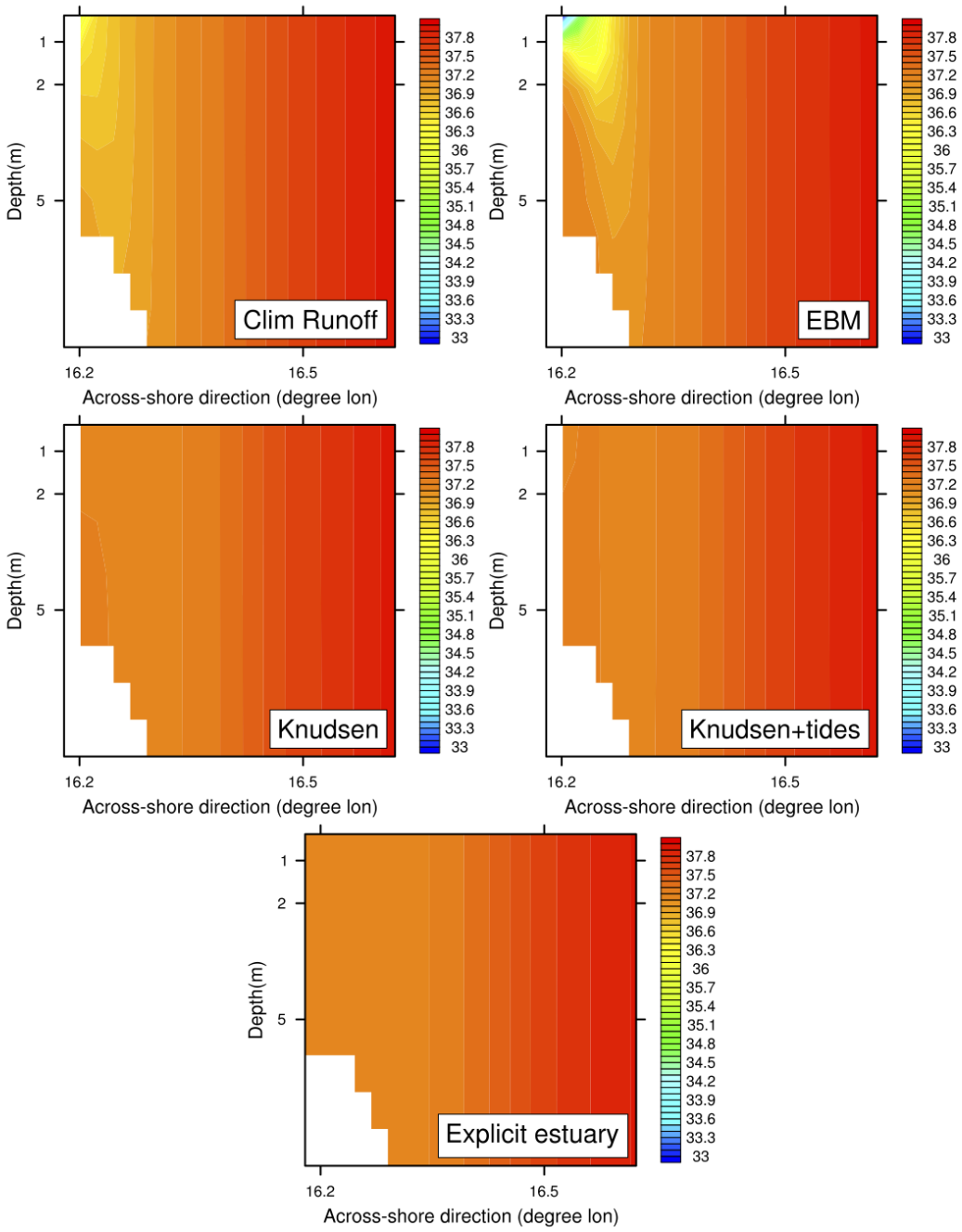

Figure 4.8: Coastal dynamics off the Ofanto estuary. Zonal transect of daily averaged salinity on 2011/02/19

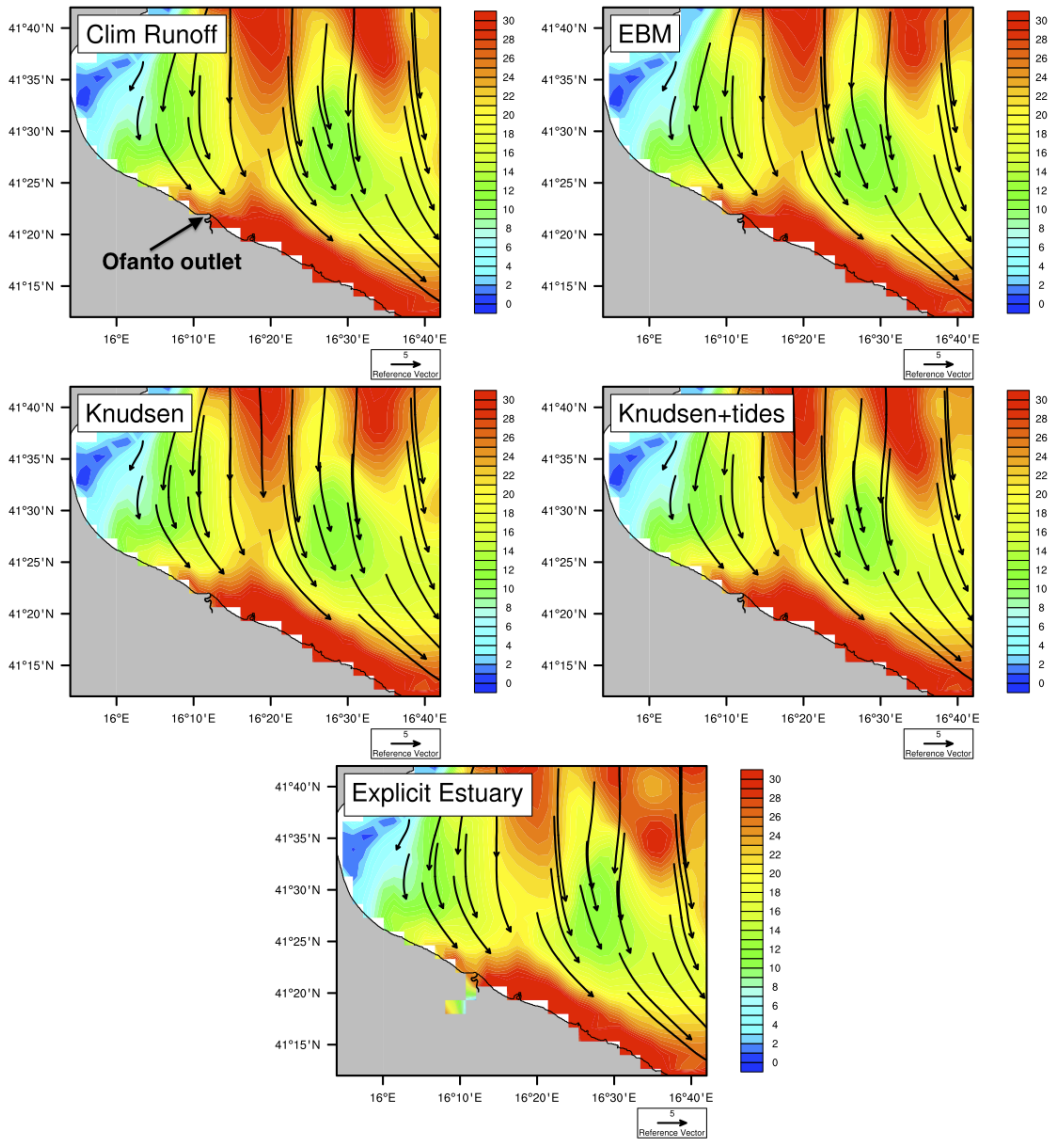

Figure 4.9: Coastal dynamics off the Ofanto estuary. Daily surface currents (units of cm/s) on 2011/02/19

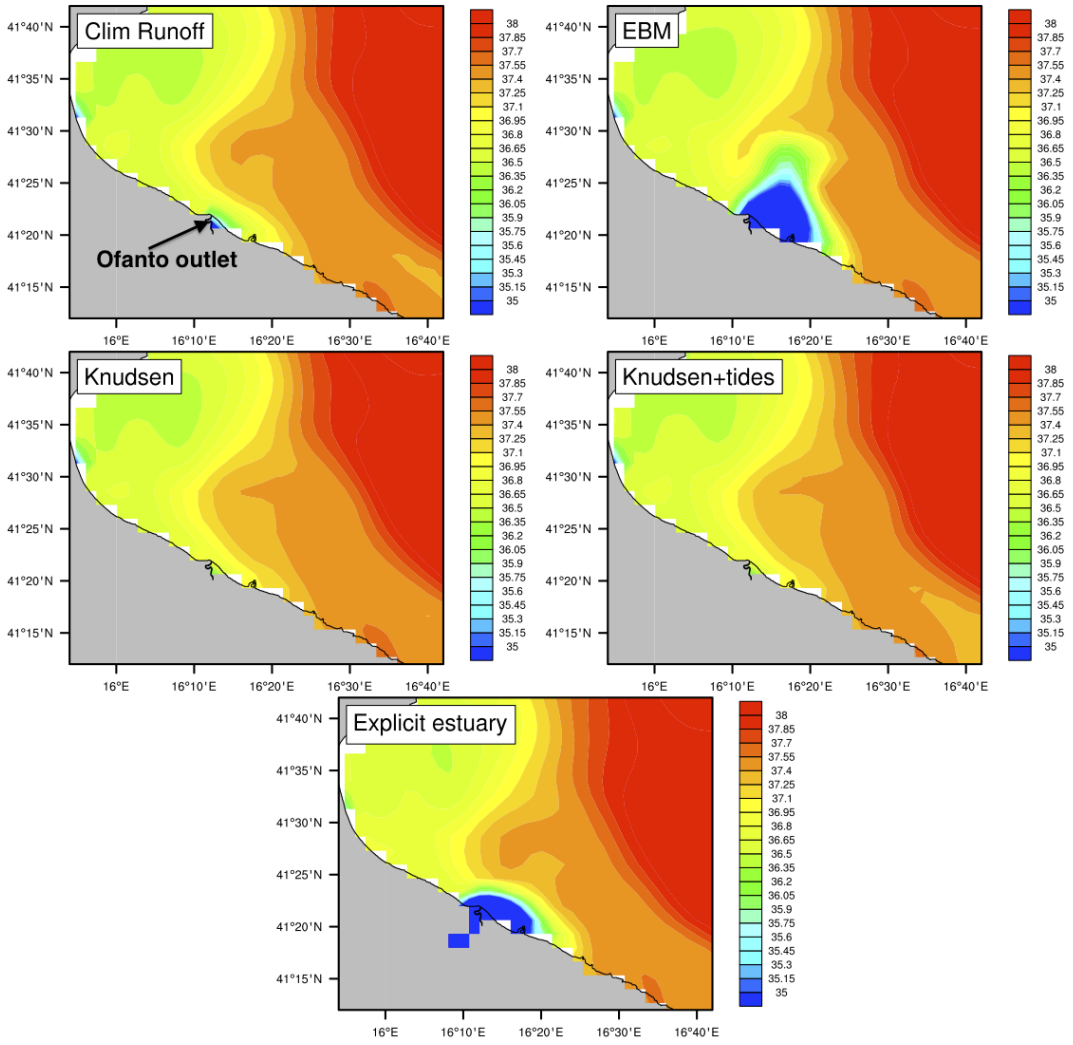

Figure 4.10: Coastal dynamics off the Ofanto estuary. Daily averaged sea surface salinity on 2011/03/03

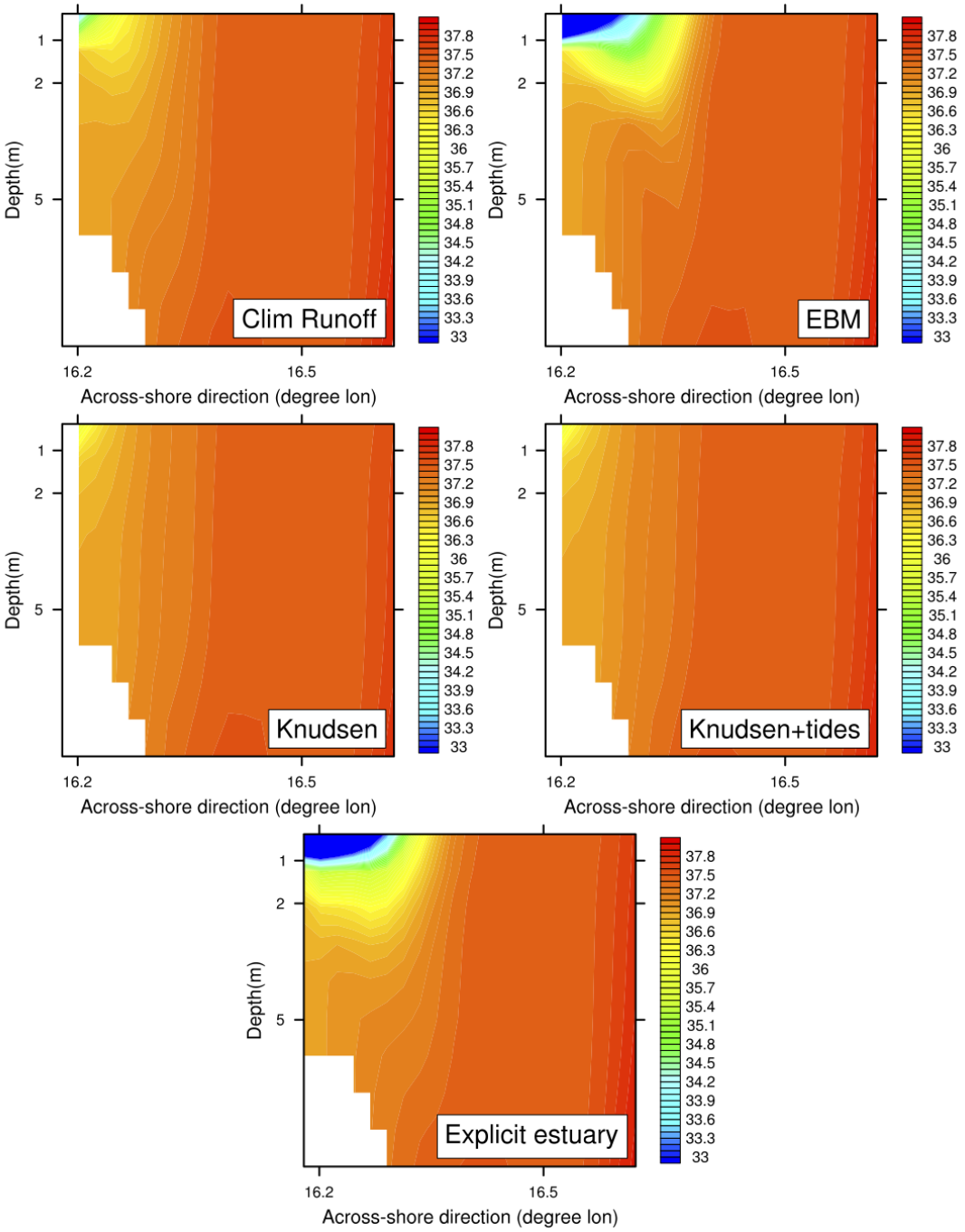

Figure 4.11: Coastal dynamics off the Ofanto estuary. Zonal transect of daily averaged salinity on 2011/03/03

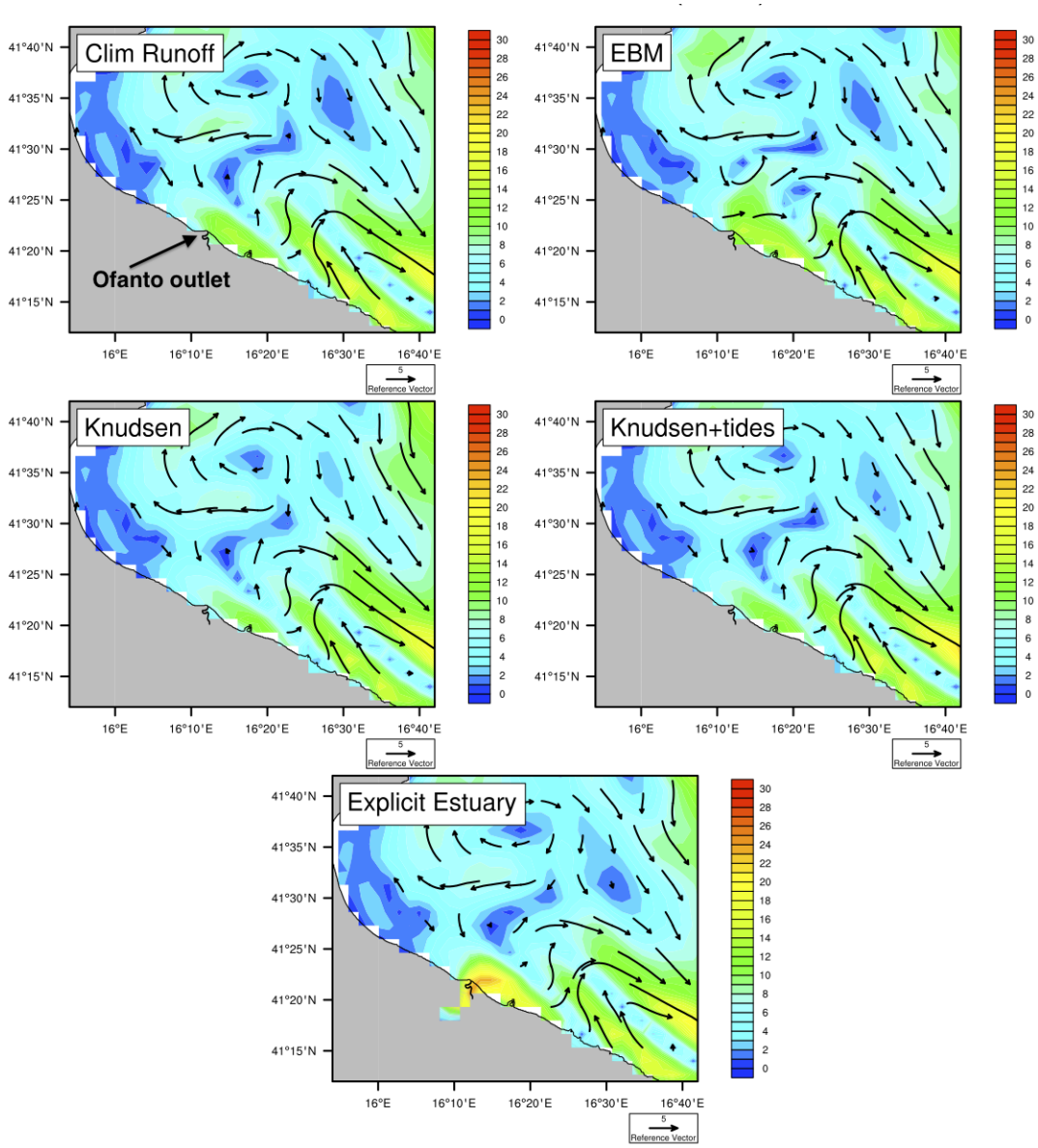

Figure 4.12: Coastal dynamics off the Ofanto estuary. Daily surface currents (units of cm/s) on 2011/03/03

5 Conclusions and future perspectives

Two main questions inspired this study.

May rivers play a significant role on the circulation and dynamics of the Central Mediterranean Sea?

How to realistically represent the riverine freshwater discharge into a regional ocean model?

The first question arose from the awareness the Central Mediterranean Sea is one of the few Mediterranean areas where river runoff is important for the coastal as well as the open sea overturning circulation. We started from the hypothesis rivers affect the buoyancy budget of the Adriatic Sea, since 1/3 of the Mediterranean discharge is here located and makes the Adriatic Sea a dilution basin. We also expect rivers influence the Ionian Sea because the Adriatic dense waters are one of the major drivers of the Ionian abyssal circulation. We used a high-resolution ocean model with a complete distribution of rivers in the Adriatic and Ionian catchment areas and we performed a twin experiment, with and without river inflow, from 1999 to 2012. We applied Spall's theoretical model, dealing with the water mass budget in an idealised marginal sea, to the Adriatic basin. We found that river runoff cannot reverse the dominant anti-estuarine character of Adriatic circulation or shut down the deep convection in the basin interior. However we demonstrated rivers affect the Adriatic dense water volumes. We showed that rivers counteract the vertical mixing processes in the Southern Adriatic sub-region by changing the water column stratification and thus they decrease the local dense water volumes. Finally we showed that the Adriatic dense waters overflowing the Otranto Strait are less dense in a realistic runoff regime, thus implying a stronger turbulent mixing with the Ionian abyssal waters and a higher offshore spreading.

The Southern Adriatic open-sea convection represents the downwelling branch which drives the overturning circulation pattern in the Central Mediterranean sub-basin. As far as we know this study provides the first investigation on river role on the Central Mediterranean overturning circulation. A key result is that the Central Mediterranean MOC is largely wind driven but large and anomalous

river runoff can affect its strength, enhancing the amplitude of the secondary estuarine cells and reducing the intensity of the dominant anti-estuarine cell.
About future perspectives we plan to perform a new Twin Experiment, with and without river representation, by extending the computational domain of our ocean model to the whole Mediterranean Sea and the time window up to 50yr. This would allow to capture the multi-decadal natural variability of the Mediterranean Sea and to weigh river role with respect to the other forcing mechanisms of the whole Mediterranean circulation.
All these results on the theoretical role of river inflow on the Central Mediterranean Sea strongly motivated us to investigate the second key question which is how to realistically represent the riverine freshwater discharge into a regional ocean model.
The regional ocean models based on finite difference grids cannot solve the estuary dynamics due to their numerical constraints. Moreover they generally treat the riverine freshwater release in a oversimplified way by means of climatological runoff, based on gauges located far from river outlets, and zero or at most constant salinity values corresponding to the runoff. Thus the estuarine dynamics triggered by the ocean water entrainment and how this affect the resulting buoyancy plume in the ROFI are not taken into account.
We aimed to overcome this shortcoming of the mesoscale ocean modeling and to increase the forecast/hindcast capability of our regional ocean model by developing a reasonable representation of the riverine freshwater discharge.
Thus first of all we implemented an integrated modelling system including the atmosphere, the hydrology and the hydraulics components in order to solve the local water cycle of a specific catchment. We highlighted the precipitation forecasting is still one of the most critical task for meteorological mesoscale models since this is the end result of many multi-scales processes interacting each other. Moreover the representation of the precipitation field is critical for ensuring the quality of the hydrological modelling. We pointed out a full description of the infiltration rate, the aquifer water storage and the river routing strongly influences the capability to predict the river streamflow along the river network and finally the net discharge at the river mouth. The ocean water entering the river mouth

and the resulting estuarine dynamics need to be solved as well.

The highly stratified estuary of the Ofanto river is considered as case study. We aim to describe the main physical processes involved in the water and energy balance of the estuary. Our results show the tidal pumping plays the predominant role in the exchange of fresher water leaving the estuary (ebb tide) and saltier ocean water entering the estuary (flood tide). We compared three approaches of the estuarine dynamics: the simple Knudsen's relation, an upgraded version of the Knudsen's relation we developed with the addition of tides, and an estuary box model developed by the University of Connecticut and the National Center for Atmospheric Research. The results of these method are used to force our regional ocean model in the ROFI of the Ofanto river. We found that the added value of better representing the estuarine dynamics and its effect on the coastal dynamics become particularly clear during the upwelling wind regime. Upwelling favourable winds act in the same direction of the freshwater release by promoting the vertical stratification and the surface offshore spreading, this results in a well defined buoyancy river plume.

The UCONN-NCAR model is the only one which is capable to represent a well defined river plume during upwelling wind. On the other hand, the estuary model based on the Knudsen's relation with the addition of tides is the most rigorous one from the theoretical point of view, thus future efforts will be devoted to the development of this new approach. Moreover we plan to assume as the next case study a river with a highly-mixed estuary and flowing into the Norther Adriatic sub-basin where the tidal pumping is expected to play a strong role.

Appendix A

The numerical model configuration

The numerical simulations were carried out using three-dimensional, finite difference primitive equations Nucleus for European Modelling of the Ocean code, NEMO v 3.4 (Madec, 2008).

The model solves prognostic equations for potential temperature, practical salinity, horizontal velocity components in the meridional and zonal directions, sea surface height and diagnostic equations for vertical velocity, hydrostatic pressure and potential density.

Boussinesq and hydrostatic hypotheses are assumed.

$$\frac{\partial u}{\partial t} + u\frac{\partial u}{\partial x} + v\frac{\partial u}{\partial y} + w\frac{\partial u}{\partial z} = -\frac{1}{\rho_0}\frac{\partial p}{\partial x} + A_m(\frac{\partial^2 u}{\partial x^2} + \frac{\partial^2 u}{\partial y^2}) + K_m\frac{\partial^2 u}{\partial z^2} + fv \quad (A.1)$$

$$\frac{\partial v}{\partial t} + u\frac{\partial v}{\partial x} + v\frac{\partial v}{\partial y} + w\frac{\partial v}{\partial z} = -\frac{1}{\rho_0}\frac{\partial p}{\partial v} + A_m(\frac{\partial^2 v}{\partial x^2} + \frac{\partial^2 v}{\partial y^2}) + K_m\frac{\partial^2 v}{\partial z^2} - fu \quad (A.2)$$

$$\frac{\partial p}{\partial z} = -\rho g \quad (A.3)$$

$$\bigtriangledown \cdot \vec{u} = 0 \quad (A.4)$$

$$\frac{\partial \eta}{\partial t} + \bigtriangledown_H \cdot ((H+\eta)\vec{u_{Hbaro}}) = P + R - E \quad (A.5)$$

$$\frac{\partial S}{\partial t} + \bigtriangledown \cdot (\vec{u}S) = A_t \bigtriangledown_H^2 S + K_t\frac{\partial^2 S}{\partial z^2} \quad (A.6)$$

$$\frac{\partial \theta}{\partial t} + \bigtriangledown \cdot (\vec{u}\theta) = A_t \bigtriangledown_H^2 \theta + K_t\frac{\partial^2 \theta}{\partial z^2} \quad (A.7)$$

$$\rho = \rho(\theta, S, p) \quad (A.8)$$

The first two equations (A.1) and (A.2) are the Navier-Stokes equations for the horizontal velocity vector $\vec{u_H} = (u, v)$. The coefficients A_m and K_m are the momentum eddy coefficients for horizontal and vertical mixing respectively, fv and $-fu$ are the horizontal components of Coriolis term on f-plane approximation. The eq.(A.3) is the Navier-Stokes equation in the vertical direction reduced to the hydrostatic equilibrium equation. The eq.(A.4) is the continuity equation with

Boussinesq hypothesis (i.e. quasi-incompressible fluid) where $\vec{u} = (u, v, w)$ which allows to compute the vertical velocity, w, as diagnostic variable. The eq.(A.5) is the vertically integrated continuity equation, written as a prognostic equation for the free surface starting from the vertical integration of eq.(A.4) and replacing the definition of barotropic velocity that is $\vec{u_{Hbaro}} = \frac{1}{H+\eta} \int_{-H}^{\eta} \vec{u_H} dz$

The eq.(A.6) and eq.(A.7) are the advection/diffusion equations for tracers with A_t and K_t the horizontal and vertical mixing coefficients of tracers. Finally the sea state equation (A.8) prescribes the ocean water density is a non linear empirical function of potential temperature, salinity and pressure (following Jackett and McDougall 1995).

The sea surface height equation (A.5) and the associated barotropic velocity equations are solved by the time-splitting formulation, thus using a smaller time step than for three-dimensional prognostic variables.

In order to solve the mesoscale variability of the Adriatic Sea, at least in the Southern sub-basin, a horizontal grid resolution equal to 1/45° was chosen, corresponding to 2.47 km in the meridional direction and 1.72 to 2.13 km in the zonal direction. The literature shows the first baroclinic Rossby radius of deformation in the Mediterranean Sea is around 10-12 km (Grilli and Pinardi, 1998; Pinardi and Masetti, 2000) if we take the open flow scale variables, but the local values may significantly reduce depending on season and latitude and moving towards the shelf areas. In the Northern Adriatic Sea it reduces up to about 3-5 km in summer and 1 km in winter (Paschini et al., 1993; Masina and Pinardi, 1994; Bergamasco and Gacic, 1996). This means our model can explicitly resolve the mesoscale activities in the Adriatic Sea, at least in the Southern sub-basin, on seasonal as well as on interannual basis with the only exception of the Northern Adriatic where the model may result eddy-permitting but not eddy-resolving.

The model bathymetry, covering both the Adriatic and Ionia Sea, is taken from the U.S. Navy 1/60° bathymetric database DBDB1 using bilinear interpolation. A total of 121 unevenly spaced z-levels with partial steps were adopted in the vertical direction. Partial steps allow a better representation of the bathymetry. The higher resolution in the top layers (23 levels in the top 35 m which is the mean depth of the NAd subregion) leads to an improved simulation of the bottom

flow in the NAd and vertical mixing during higher stratification in the summer. There are two open boundaries on the eastern and western sides of the model domain. Open boundaries data are provided as monthly means and involve the following prognostic variables interpolated on the model grid: zonal velocity (u_{3d}), meridional velocity (v_{3d}), potential temperature (θ), salinity (S), and the sea surface height (η). For both the lateral open boundary conditions, LOBCs, and the initial conditions, ICs, data are taken from daily analysis of the operational Mediterranean forecasting System, MFS (Tonani et al., 2008; Pinardi and Coppini, 2010) based on the same code, NEMO, and covering the whole Mediterranean basin with 1/16° horizontal resolution.

The numerical schemes adopted for the LOBCs are described below.

Marchesiello's algorithm (2001) was used for active tracers. It consists of the 2D radiation condition plus a relaxation/nudging term as follows:

$$\frac{\partial \phi}{\partial t} + C_{\phi x}\frac{\partial \phi}{\partial x} + C_{\phi y}\frac{\partial \phi}{\partial y} = -\frac{1}{\tau}(\phi - \phi_{nested}) \tag{A.9}$$

where ϕ is the tracer (θ or S), ϕ_{nested} is the coarser model (MFS) solution for the tracer interpolated on our model grid and provided monthly. The time scale for the nudging term, τ, is constant and equal to one day for inward propagation and 15 days for outward propagation. For outward propagation, i.e. $C_{\phi_x} > 0$ where C_{ϕ_x} is the component of the phase velocity normal to the boundary, the tangential component is set equal to zero, $C_{\phi_y} = 0$. For inward propagation, $C_{\phi_x} < 0$, the algorithm prescribes C_{ϕ_x} =C$_{\phi y} = 0$ thus reduced to a relaxation condition.

For the horizontal velocity components, u_{3d} and v_{3d}, the imposition scheme is used and thus, the incoming and outgoing information is totally determined by the coarser model data, irrespective of the inner solution.

In addition, the horizontal velocity component normal to each boundary is uniformly adjusted according to the "interpolation constraint" procedure (Pinardi et al., 2003) in order to preserve the total volume transport after data interpolation from the coarse to the fine resolution grid.

For the barotropic velocities, u_{BT} and v_{BT}, Flather's scheme (1976) was adopted. The barotropic velocity component normal to the eastern and western boundaries

is given by Flather's equation:

$$u_{BT} = u_{BTnested} - \frac{\sqrt{gH}}{H}(\eta_{nested} - \eta) \tag{A.10}$$

where η_{nested} is the coarser model sea surface height at the boundary interpolated over the finer model grid, η is the finer model sea surface height at the boundary and $u_{BTnested}$ is the coarser model normal barotropic velocity over the finer model grid computed as $u_{BTnested} = \frac{1}{H+\eta}\int_{-H}^{\eta} u_{3dnested}dz$.

The tangential barotropic velocity is set equal to zero: $v_{BT} = 0$.

In Flather's formula, η values at the boundary follow a "zero gradient boundary condition" which means $\eta_B = \eta_{B-1}$ (subscript B stands for boundary line values). This avoids numerical instabilities.

The bottom boundary condition is applied only on momentum and consists of a quadratic friction.

No slip boundary conditions are adopted along the coastline for tangential velocity.

In order to define the air-sea interaction, the vertical fluxes of momentum, heat and salt and the vertical velocity were parameterized at the sea surface. These parameterizations are the surface boundary conditions (SBCs) of the model. Wind stress and heat flux components are computed by means of "bulk formulae" (Castellari et al., 1998; Maggiore et al., 1998; Oddo et al., 2011; Madec, 2008) using atmospheric data provided by the European Centre for Medium Weather Forecasts (ECMWF). These atmospheric data (2m air temperature, 2m dew point temperature, total cloud cover, mean sea level atmospheric pressure, meridional and zonal 10m wind components) are operational analyses with a 6h frequency and with 0.5° or 0.25° horizontal resolution. Only the precipitation rate (P) data are extracted from the CMAP (CPC, Climate Prediction Center, Merged Analysis of Precipitation) monthly data set with a horizontal resolution of $2.5°X2.5°$. The surface boundary condition for temperature involves a balance between solar short-wave radiation Q_s (computed using Reed's formula, 1977), long-wave radiation Q_l (computed using Bignami et al., 1995), latent Q_e and sensible Q_h heat fluxes (by means of bulk formulae proposed by Kondo, 1975).

Reed's formula is:

$$Q_s = Q_{tot}(1 - 0.62C + 0.0019\beta)(1 - \alpha) \tag{A.11}$$

where Q_{tot} is the clear-sky radiation, C is the fractional cloud cover, β is the noon sun altitude in degrees, and α is the sea surface albedo. The albedo is computed as a function of the sun zenith angle for each grid point from Payne (1972).
The Bignami formula is:

$$Q_l = \epsilon\sigma T_s^4 - (\sigma T_A^4(0.653 + 0.00535e_A))(1 + 0.1762C^2) \tag{A.12}$$

where ϵ is the ocean emissivity, σ is the Stefan Boltzmann constant, e_A is the atmospheric vapor pressure, T_s is the sea surface temperature predicted by model, T_A is the 2m-air temperature.
The sensible Q_h and latent Q_e heat fluxes are parameterized through the Kondo bulk formula:

$$Q_h = \rho_A C_p C_H |\mathbf{u}_w|(T_s - T_A) \tag{A.13}$$

$$Q_e = \rho_A L_e C_E |\mathbf{u}_w|(e_{sat}T_s - re_{sat}T_A)(0.622/p_A) \tag{A.14}$$

where $\rho_A = \rho_A(p, T_A, r)$ is moist air density, r is the relative umidity, C_p is the specific heat capacity at constant pressure, C_H and C_E are the turbulent exchange coefficients computed according to Kondo (1975), L_e is the latent heat of vaporization, e_{sat} is the vapor pressure, $|\mathbf{u}_w|$ is the wind speed modulus, and p_A is the atmospheric pressure. For the heat flux boundary condition at the surface, we assume:

$$\rho_0 K_t \frac{\partial\theta}{\partial z}\bigg|_{z=\eta} = \frac{1}{C_p}[(1 - T_r)(Q_s - Q_l - Q_e - Q_h)] \tag{A.15}$$

where T_r is the Jerlov (1976) transmission coefficient for a "clear" water type and K_t is the vertical mixing coefficient for traces.
The wind stress involved in the surface boundary condition for momentum is calculated from the relative winds with the formula:

$$\tau_{\mathbf{w}} = \rho_{0_a} C_D |\mathbf{U}_{rel}|\mathbf{U}_{rel} \tag{A.16}$$

where $\mathbf{U}_{rel} = \mathbf{u}_w - \mathbf{u}_s = (u_{rel}, v_{rel})$ is the relative wind field that is the 10m wind horizontal velocity u_w subtracted from the sea surface horizontal velocity

u_s, ρ_{0a} is the density of the moist air and $C_D(T_a, T_s, u_w)$ is the drag coefficient which depends on air temperature, sea surface temperature and wind amplitude according to Hellerman and Rosenstein (1983).

The momentum boundary condition at the surface is:

$$\rho_0 K_m \frac{\partial(u,v)}{\partial z}\bigg|_{z=\eta} = (\tau_{wx}, \tau_{wy}) \tag{A.17}$$

where $\tau_{wx} = \rho_{0a} C_D |\mathbf{U}_{rel}| u_{rel}$ and $\tau_{wy} = \rho_{0a} C_D |\mathbf{U}_{rel}| v_{rel}$ are the wind stress components and K_m is the vertical mixing coefficient for momentum. The freshwater balance defined as evaporation minus precipitation and runoff (with the latter divided by the cell area of the river mouth), $E - P - R/A$, is directly involved in the conditions for salinity and for vertical velocity.

The salinity boundary condition at the surface reads:

$$K_t \frac{\partial S}{\partial z}\bigg|_{z=\eta} = S_{z=\eta}(E - P - \frac{R}{A}) \tag{A.18}$$

where η is the sea surface elevation. The surface boundary condition for the vertical velocity is as follows:

$$w\mid_{z=\eta} - \frac{\partial \eta}{\partial t} + (u,v)\mid_{z=\eta} \cdot \bigtriangledown_H \eta = (E - P - \frac{R}{A}) \tag{A.19}$$

where w is the vertical velocity. The Evaporation rate, E, is calculated by the latent heat flux according to $E = Q_e/L_e$. With regard to the dynamics, the following choices were selected: vector invariant form for momentum advection, bi-laplacian operator for lateral diffusion and horizontal eddy viscosity coefficient equal $-5 \cdot 10^7 m^4 s^{-1}$ according to a tuning procedure starting with MFS values, implicit vertical diffusion and TKE turbulence closure scheme (Mellor and Blumberg, 2004) to provide the vertical eddy coefficients.

With regard to the active tracers: MUSCL advection scheme, bi-laplacian operator for lateral diffusion and horizontal eddy diffusivity coefficient equal to $-3 \cdot 10^7 m^4 s^{-1}$ according to a tuning procedure, implicit and TKE dependent vertical diffusion.

Appendix B

The computation of Spall's coefficients

We followed Spall's studies (2004, 2010, 2011, 2012) on the overturning circulation in the marginal seas and we applied his theoretical model on the water mass transformation within an idealised marginal sea to the Adriatic basin. The Adriatic Sea perfectly matches the characteristics of this theoretical model. We computed Spall's non-dimensional coefficients which represent the relative balance between surface forcing and lateral eddy fluxes in the heat and salinity balance. The lateral eddy fluxes advect warm and salty water in the basin interior and detach from the cyclonic boundary current which inflows along the eastern side from the open ocean and encircles the marginal sea. Details on the cyclonic boundary current system and the exchange with the interior are drawn in Figure B.1, taken from Spall, 2012.

The combinations μ/ϵ and γ/ϵ are called respectively thermal and freshwater forcing parameter and are described below:

$$\frac{\mu}{\epsilon} = \frac{A\Gamma f_0}{\alpha_T G C_p H^2 T^*} / \frac{cP}{L} \tag{B.1}$$

$$\frac{\gamma}{\epsilon} = \frac{8A\rho_0 f_0 S_0 \alpha_s (E - P - R)}{gH^2 \alpha_T^2 T^{*2}} / \frac{cP}{L} \tag{B.2}$$

where A is the area of the Adriatic sea surface (from model domain), Γ is the relaxation constant for the basin sea surface temperature toward the atmospheric temperature (from Spall 2011), f_0 is the Coriolis parameter, α_T is the thermal expansion coefficient (from Cessi et al., 2014), α_s is the haline expansion coefficient (from Cessi et al., 2014), H is the depth of the sill (from model domain), P is the perimeter of the basin interior (from model domain), C_p is the thermal capacity (from Cessi et al., 2014), L is the width of the sloping topography over which the inflowing boundary current lies (thus computed from model results as the cross-shore width of the inflowing boundary current along the eastern shelf of the Adriatic basin).

The variable $\delta = \frac{h_x}{-\overline{\rho_x}/\overline{\rho_z}} = -0.33$ represents the topography slope over the mean

isopycnal slope following the inflowing boundary current. Thus they are both computed along the Southern Adriatic eastern shelf: h_x is the topography slope in the zonal direction, i.e. x, ρ_x is the mean isopycnal slope in the zonal direction and ρ_z is the mean isopycnal slope in the depth, z-direction. To note that δ has been computed by considering a zonal transect of potential density anomaly at $40.8°N$ (so just north of the Otranto Strait) on annual basis and focusing on the eastern side of the basin. For cyclonic boundary current, $\delta < 0$ and the topography acts to stabilize the boundary current and reduce the amount of lateral eddy flux into the interior. The quantity $c = 0.025e^{2\delta} = 0.05$ is an efficiency coefficient that depends on the bottom slope and regulates the eddy heat flux from the boundary current into the interior (Spall, 2004).

The non-dimensional parameter $\epsilon = \frac{cP}{L}$ is the ratio of the heat flux toward the basin interior due to lateral eddies compared to that advected into the Adriatic Sea through the inflowing boundary current along the Southern Adriatic eastern shelf. The inflowing boundary current is assumed to be a geostrophic current in thermal wind balance. The value of ϵ is very small for stable boundary currents and increases for boundary currents that are sufficiently unstable that they lose all their heat to the interior of the basin before it is carried all the way around the marginal sea.

Moreover the thermal and freshwater forcing parameters required to compute T^*, that is the difference between the inflowing temperature and the temperature of the atmosphere over the interior of the marginal sea, as follows:

$$T^* = T_1 - T_A = \begin{cases} 2.56°C \text{ in EXP1} \\ 2.84°C \text{ in EXP2} \end{cases}$$

where T_1 is the mean temperature of the inflowing current along the eastern boundary derived from the EXPs, T_A is the mean 2m temperature over the Adriatic basin extracted from ECMWF 25 km dataset.

Finally the surface freshwater flux is defined as follows:

$E - P = 0.66 \cdot 10^{-7}(ms^{-1})\ in\ EXP2$

$E - P - R = -2.18 \cdot 10^{-7}(ms^{-1})\ in\ EXP1$

All the quantities described above enable to compute the thermal and

freshwater forcing parameters in (B.1) and (B.2), giving:

$$\mu/\epsilon = \begin{cases} 5.0 \cdot 10^{-5} \text{ in EXP1} \\ 4.9 \cdot 10^{-5} \text{ in EXP2} \end{cases}$$

$$\gamma/\epsilon = \begin{cases} -2 \cdot 10^{-2} \text{ in EXP1} \\ 7.0 \cdot 10^{-4} \text{ in EXP2} \end{cases}$$

As discussed by Spall (2011), μ/ϵ is a measure of the relative influence of lateral eddy heat fluxes from the boundary current into the basin interior compared to heat loss to the atmosphere. For $\mu/\epsilon << 1$, lateral eddy heat flux from the boundary is very strong and leads to a relatively warm basin interior so that $T \approx T_1$, if $\mu/\epsilon > 1$ the boundary current is relatively stable and the atmosphere is able to strongly cool the basin interior so that $T \approx T_A$. Similarly γ/ϵ describes the relative role of surface forcing and lateral eddy fluxes in the salinity balance. Large values of γ/ϵ indicate dominance of atmospheric forcing implying freshwater gains in the basin interior that are not balanced by lateral eddy fluxes of salt from the boundary current, and small values indicate strong lateral eddy fluxes.

In order to evaluate the shutdown of deep convection and the reversal of the overturning circulation, the temperature and salinity anomalies of the basin convective water mass have been computed as normalized differences of T (i.e. $\triangle T$) and S (i.e. $\triangle S$) between basin interior and boundary currents (Spall 2012). A set of 2 non-dimensional equations has been derived to compute $\triangle T$ and $\triangle S$ (Spall 2012), these equations include the non-dimensional parameters μ/ϵ and γ/ϵ and describe $\triangle T$ and $\triangle S$ as function of basin geometry, atmospheric forcing and lateral eddy fluxes.

The simplified formula suggested in Spall 2012 are:

$$\triangle T = \frac{T_1 - T}{T^*} \tag{B.3}$$

$$\triangle S = \frac{(S_1 - S)\alpha_S}{\alpha_T T^*} \tag{B.4}$$

where T and S for the basin interior and T_1 and S_1 for the inflowing current

have been computed over 50-200m depth.

The ratio $\triangle S/\triangle T < 1$ means the stable circulation state is in the "Thermal Mode" with surface heat losses and freshwater gains prevailing the lateral eddy advection of warm and salt water in the basin interior (thermal and freshwater forcing coefficients are significantly high). In this case the density contrast is dominated by the temperature difference and the water in the interior of the marginal sea is more dense than that in the boundary current.

If $\triangle S/\triangle T > 1$, the stable circulation state is in the "Haline Mode" with surface heat and freshwater budget of the interiors basin favouring the lateral eddy advection of warm and salt water (thermal and freshwater forcing coefficients are low enough and the latter is eventually negative). In this case the density contrast is dominated by the salinity difference and the water in the interior of the marginal sea is less dense than that in the boundary current. Thus the boundary current detaches from the eastern shelf and spreads in the interior basin. This means in haline mode the surface boundary current is in the opposite sense, anticyclonic around the coastline, and the deep convection in the basin interior is not longer supported with reversal of the meridional overturning circulation.

The theoretical limit for shutdown of deep convection is $\triangle S/\triangle T > 0.5$, thus possible also in the Thermal Mode.

According to our findings, both EXPs are in the Thermal Mode and EXP1 is closer to the threshold limit for shutdown of deep convection than EXP2.

Results collected for EXP1 and EXP2 are summarizes in Table 2.2 and show that deep convection in the Southern Adriatic, surface cyclonic boundary current and anti-cyclonic anti-estuarine overturning circulation of the Adriatic basin characterize both experiments but in EXP1, with a realistic parameterization of river runoff, the freshwater forcing coefficient is negative and the ratio $\triangle S/\triangle T$ close to 0.5. This corroborates strong river discharge in the Adriatic Sea has the potential to trigger the shutdown of deep convection and the weakening of the anti-estuarine overturning circulation.

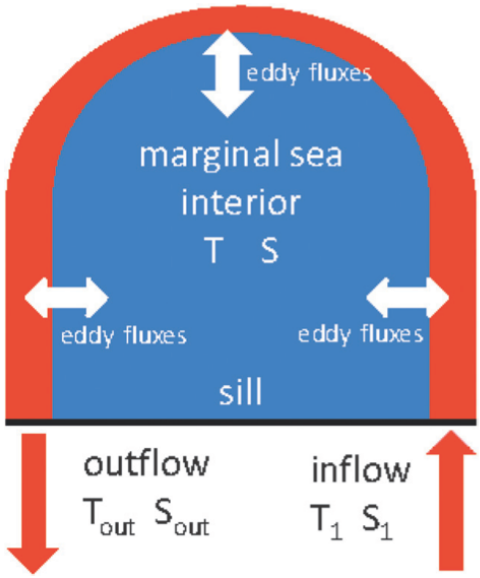

Figure B.1: Schematic of the idealized marginal sea model. (From Spall, 2012)

List of attended workshops

1st European Coupled Atmospheric-Hydrological Modeling and WRF Hydro User Workshop, Cosenza

WRF Workshop-NCAR Summer School, Boulder

NCL Workshop-NCAR, Boulder

IWMO 2014, Bergen

GODAE OceanView Coastal & Shelf Seas Task Team, Lecce

EGU Assembly 2014, Vienna. http://meetingorganizer.copernicus.org/EGU2014/EGU2014-16855.pdf

Ocean Science Meeting 2016, New Orleans.
https://agu.confex.com/agu/os16/preliminaryview.cgi/Paper90821.html

EGU Assembly 2016, Vienna. http://meetingorganizer.copernicus.org/EGU2016/EGU2016-13226.pdf

Visiting periods

Student visitor at National Center for Atmospheric Research, Boulder (Colorado, USA) over September 2015 to March 2016

Student visitor at National Center for Atmospheric Research, Boulder (Colorado, USA) over February 2016

List of papers

G.Verri, N.Pinardi, P. Oddo, S.Ciliberti and G.Coppini, 2016. Influence of river runoff in the Central Mediterranean Sea basins. Paper submitted to Ocean Dynamics

G. Verri, N. Pinardi, J. Tribbia, D. Gochis, A. Navarra, G. Coppini, T. Vukicevic, and D. Shea, 2016. A meteo-hydrological modeling study for flood events in the Ofanto river catchment. Paper submitted to the Natural Hazards and Earth System Sciences

G. Verri, N. Pinardi, J. Tribbia, F. Bryan, Y. Tseng, Q. Sun, G. Coppini, 2016. Estuarine dynamics for ocean modeling: the case study of the Ofanto estuary. Paper to be submitted to the Journal of Physical Oceanography

References

[1] *Artegiani, A., Azzolini, R., Salusti, E., 1989: On the dense water in the Adriatic Sea* Oceanol. Acta., 12, 151-160

[2] *Artegiani, A., Paschini, E., Russo, A., Bregant, D., Raicich, F., Pinardi, N., 1997a. The Adriatic Sea General Circulation. Part I: Air-Sea Interactions and Water Mass Structure* J. Phys. Ocean., 27: 1492-1514

[3] *Artegiani, A., Paschini, E., Russo, A., Bregant, D., Raicich, F., Pinardi, N., 1997b. The Adriatic Sea General Circulation. Part II: Baroclinic Circulation Structure* J. Phys. Ocean., 27: 1515-1532

[4] *Astraldi, M., Balopoulos, S., Candela, J., Font, J., Gaci?, M., Gasparini, GP., Manca, B., Theocharis, A., Tintore, J., 1999. The role of straits and channels in understanding the characteristics of Mediterranean circulation* Progress in Oceanography, 44(1-3), 65-108

[5] *Barredo, J.I., 2007. Major flood disasters in Europe: 1950-2005* Nat. Hazards 42, 125-148

[6] *Barnes, S., 1964. A technique for maximizing details in numerical weather map analysis* J. Appl. Meteor., 9(3), 396-409

[7] *Bensi, M., Rubino, A., Cardin, V., Hainbucher, D., Mancero-Mosquera, I., 2013. Structure and variability of the abyssal water masses in the Ionian Sea in the period 2003-2010* J. Geophys. Res. Oceans, 118(2), 931-943

[8] *Bergamasco, A., Gacic, M., Boscolo, R., Umgiesser, G., 1996. Winter oceanographic conditions and water mass balance in the Northern Adriatic (February 1993)* J Mar Sys, 7, 67-94

[9] *Beron-Vera, F.J., Ochoa, J., and Ripa, P., 1999. A note on boundary conditions for salt and freshwater balances* Ocean Modelling, 1, 111-118

[10] *Bethoux, J. P., 1979: Budgets of the Mediterranean Sea: their dependence on the local climate and on the characteristics of the Atlantic waters* Oceanol. Acta, 2, 157-163

[11] *Bryan, F., 1986: High-latitude salinity effects and interhemispheric thermohaline circulations* Nature, 323, 301-304

[12] *Buljan, M., Zore-Armanda, M., 1976: Oceanographical properties of the Adriatic Sea* Oceanography and Marine Biology Annual Review, 14, 11-98

[13] Buzzi, A., and Tibaldi, S., 1978. Cyclogenesis in the lee of the Alps- A case study. Royal Meteorological Society, Quarterly Journal, 104, 271-287

[14] *Castellari, S., Pinardi, N., Leaman, K., 1998. A model study of air?sea interactions in the Mediterranean Sea* J Mar Syst, 18(1-3), 89-114

[15] *Chao, S. Y., 1987. Wind driven motion near inner shelf fronts* Journal of Geophysical Research: Oceans, 92(C4), 3849-3860

[16] *Chapman, D. C., and Beardsley, R. C., 1989. On the origin of shelf water in the Middle Atlantic Bight* Journal of Physical Oceanography, 19(3), 384-391

[17] *Chen, F., MacDonald, D. G., 2006. Role of mixing in the structure and evolu- tion of a buoyant discharge plume* Journal of Geophysical Research, 111(C11)

[18] *Cessi, P., Pinardi, N., Lyubartsev, V., 2014. Energetics of semi-enclosed basins with two-layer flows at the strait* J. Phys. Oceanogr., 44, 967-979

[19] *Curchitser, E., N., Haidvogel, D., B., Iskandarani, M., 2001. Transient Adjustment of Circulation in a Midlatitude Abyssal Ocean Basin with Realistic Geometry and Bathymetry* J. Phys. Oceanogr., 31, 725-745

[20] *Cushman-Roisin, B., Gacic, M., Poulain, P. M., Artegiani, A., 2002. Physical Oceanography of the Adriatic Sea, in: Past, Present and Future* Kluwer Academic Publishers, pp. 304

[21] *Davolio, S., Miglietta, M. M., Diomede, T., Marsigli, C. , Morgillo, A., Moscatello, A., 2008. A meteo-hydrological prediction system based on a multi-model approach for precipitation forecasting* Nat. Hazards Earth Syst. Sci., 8, 143-159

[22] *Delrieu, G., V. Ducrocq, E. Gaume, J. Nicol, O. Payrastre, E. Yates, P.E. Kirstetter, H. Andrieu, P.-A. Ayral, C. Bouvier, J.-D. Creutin, M. Livet, S. Anquetin, M. Lang, L. Neppel, C. Obled, J. Parent-du-Chatelet, G.-M. Saulnier, A. Walpersdorf and W. Wobrock, 2005, The catastrophic flashflood event of 8-9 September 2002 in the Gard region, France: a first case study for the Cevennes-Vivarais Mediterranean Hydro-meteorological Observatory* J. Hydromet., 6, 34-52

[23] *Egbert, G. D., Erofeeva, S. Y., 2002. Efficient inverse modeling of barotropic ocean tides* Journal of Atmospheric and Oceanic Technology, 19(2), 183-204

[24] *Ferentinos, G., Kastanos, N., 1988. Water circulation pattern in the Otranto Strait - Eastern Mediterranean* Continental Shelf Research, 8(9), 1025-1041

[25] *Fiori, E., Comellasa, A., Molini, D., Rebora, N., Siccardi, F., Gochis, D., Tanelli, S., Parodi. A., 2014. Analysis and hindcast simulations of an extreme rainfall event in the Mediterranean area: The Genoa 2011 case* Atmospheric Research Volume 138,13-29

[26] *Fischer, H., List, E., Koh, R., Imberger, J., Brooks, N., 1979. Mixing in inland and coastal waters* Academic Press, New York

[27] *Gacic, M., Kovacevic, V., Manca, B., Papageorgiou, E. Poulain, P.-M., Scarazzato, P., Vetrano, A., 1996. Thermohaline properties and circulation in the Otranto Strait* Bulletin-Institut Oceanographique Monaco-Numero Special, 117-146

[28] *Garvine, R. W., 1999. Penetration of buoyant coastal discharge onto the continental shelf: A numerical model experiment* Journal of Physical Oceanography, 29(8), 1892-1909

[29] *Garvine, R. W., Whitney, M. M., 2006. An estuarine box model of freshwater delivery to the coastal ocean for use in climate models* Journal of Marine Research, 64(2), 173-194

[30] *Geyer, W. R., Smith, J. D., 1987. Shear instability in a highly stratified estuary* Journal of Physical Oceanography, 17(10), 1668-1679

[31] *Gochis, D. J., and Chen, F., 2003. Hydrological enhancements to the community Noah land surface model: Technical description* NCAR Sci. Tech. Note TN-4541STR, 68 pp

[32] *Gochis, D. J., Yu, W., and Yates, D.N., 2013. The WRF-Hydro Model Technical Description and User's Guide, Version 1.0* NCAR Technical Document, 120 pp

[33] *Grilli, F., Pinardi, N., 1998: The computation of Rossby radii of deformation for the Mediterranean Sea* MTP News

[34] *Guarnieri, A., Pinardi, N., Oddo, P., Bortoluzzi, G., and Ravaioli, M., 2013: Impact of tides in a baroclinic circulation model of the Adriatic Sea* J. Geophys. Res. Oceans, 118(1), 166-183

[35] *Gochis, D. J., and Chen, F., 2003. Hydrological enhancements to the community Noah land surface model: Technical description* NCAR Sci. Tech. Note TN-4541STR, 68 pp

[36] *Gochis, D.J., W. Yu, D.N. Yates, 2013. The WRF-Hydro model technical description and users guide, version 1.0. NCAR Technical Document*

[37] *Gunduz, M., Dobricic, S., Oddo, P., Pinardi, N., 2013. Impact of Levantine Intermediate Water on the interannual variability of the Adriatic Sea based on simulations with a fine resolution ocean model* Ocean Modelling, 72, 253-263

[38] *Groisman, Pavel Ya, Knight, R.W., Karl, T.R., Easterling, D.R., Sun, B., Lawrimore, J.M., 2004. Contemporary changes of the hydrological cycle over the contiguous United States: trends derived from in situ observations* J. Hydrometeorol. 5, 64-85

[39] *Groisman, Pavel Ya, Knight, Richard W., Easterling, David R., Karl, Thomas R., Hegerl, Gabriele C., Razuvaev, Vyacheslav N., 2005. Trends*

in intense precipitation in the climate record J. Climate 18, 1326-1350
Gunduz, M., Dobricic, S., Oddo, P., Pinardi, N., 2013. Impact of Levantine Intermediate Water on the interannual variability of the Adriatic Sea based on simulations with a fine resolution ocean model Ocean Modelling, 72, 253-263

[40] *Hong, S.Y., Lim, J.O. J., 2006. The WRF Single-Moment 6-Class Microphysics Scheme (WSM6)* J. Korean Meteor. Soc., 42, 129?151.

[41] *Huang, R.X., 1993. Real freshwater as a natural boundary condition for the salinity balance and thermohaline circulation forced by evaporation and precip- itation* J. Phys. Ocean. 23, 2428-2446

[42] *Iacono, M. J., Delamere, J. S., Mlawer, E. J., Shephard, M. W., Clough, S. A., and Collins, W. D., 2008. Radiative forcing by long-lived greenhouse gases: Calculations with the AER Radiative transfer models* J. Geophys. Res., 113, D13103.

[43] *Jackett, D. R., and McDougall, T. J., 1995: Minimal adjustment of hydrographic data to achieve static stability* J. Atmos. Ocean Tech., 12, 381?389

[44] *Jirka, G. H., E. E. Adams, and K. D. Stolzenbach (1981), Buoyant surface jets* J. Hydraul. Div., Proc. ASCE, 107(HY11), 1467-1487

[45] *Kain, J. S., and J. M. Fritsch, 1993. Convective parameterization for mesoscale models: The Kain-Fritcsh scheme, The representation of cumulus convection in numerical models* K. A. Emanuel and D.J. Raymond, Eds., Amer. Meteor. Soc., 246 pp.

[46] *Killworth, P. D., 2006: Time interpolation of forcing fields in ocean models* J. Phys. Oceanogr., 26, 136?143

[47] *Knudsen, M., 1900. Ein hydrographischer Lehrsatz* Ann. Hydrogr. Maritimen Meteor., 28, 316-320

[48] *Kourafalou, V.H., Oey, L.Y., Wang, J.D., Lee, T.N., 1996a. The fate of river discharge on the continental shelf. Part I: modeling the river plume*

and the inner-shelf coastal current Journal of Geophysical Research 101 (C2), 3415-3434

[49] *Kourafalou, V.H., 1999. Process studies on the Po River plume, North Adriatic Sea* Journal of Geophysical Research 104 (C2), 29963-29985

[50] *Kourafalou, V. H. and Barbopoulos, K., 2003. High resolution simulations on the North Aegean Sea seasonal circulation* Ann. Geophys., 21, 251-265

[51] *Lascaratos, A., 1993: Estimation of deep and intermediate water mass formation rates in the Mediterranean Sea* Deep Sea Research Part II: Topical Studies in Oceanography, 40(6), 1327-1332

[52] *Laviola, S., Moscatello, A., Miglietta, M. M., Cattani, E., Levizzani, V., 2011. Satellite and Numerical Model Investigation of Two Heavy Rain Events over the Central Mediterranean* Journal of Hydrometeorology, 12(4), 634-649

[53] *Lin, Y.-L., Chao, S., Wang, T. A., Kaplan, M. L., and Weglarz, R. P., 2001. Some common ingredients for heavy orographic rainfall* Weather Forecast., 16, 633-660

[54] *Lucas-Picher, P., Boberg, F., Christensen, J. H., Berg, P., 2013. Dynamical downscaling with reinitializations: A method to generate finescale climate datasets suitable for impact studies* Journal of Hydrometeorology, 14(4), 1159-1174

[55] *Ludwig, W., Dumont, E., Meybeck, M., Heussner, S., 2009: River discharges of water and nutrients to the Mediterranean and Black Sea: major drivers for ecosystem changes dur- ing past and future decades* Prog Oceanogr 80:199-217

[56] *MacCready, P., Banas, N. S., Hickey, B. M., Dever, E. P., Liu, Y., 2009. A model study of tide- and wind-induced mixing in the Columbia River Estuary and plume* Continental Shelf Research, 29(1), 278-291

[57] *MacCready, P., Geyer, W. R., 2010. Advances in Estuarine Physics* Annu. Rev. Marine. Sci., 2(1), 35-58

[58] *Madec, G., 2008. NEMO ocean engine. Note du Pole de modlisation. Institut Pierre-Simon Laplace (IPSL), France, 27: 1288-1619*

[59] *Maggiore, A., Zavatarelli, M., Angelucci, M. G., and Pinardi, N., 1998. Surface heat and water fluxes in the Adriatic Sea: Seasonal and interannual variability* Phys. Chem. Earth, 23(5-6), 561-567.

[60] *Malacic, V., and Petelin, B., 2009: Climatic circulation in the Gulf of Trieste (northern Adriatic)* Journal of Geophysical Research, 114(C7)

[61] *Manca B., Kovacevic, V., Gacic, M., Viezzoli, D., 2002. Dense water formation in the Southern Adriatic Sea and spreading into the Ionian Sea in the period 1997-1999. J Mar Syst; 33, 133-154*

[62] *Manca B., Budillon G., Scarazzato P. and Orsella L., 2003 Evolution of dynamics in the Estern Mediter- ranean affecting water mass structures and properties in the Ionian and Adriatic Seas* Jour. Geophys. Res., 108, C9, 101029-101046

[63] *Mantziafou, A. and Lascaratos, A., 2004. An eddy resolving numerical study of the general circulation and deep-water formation in the Adriatic Sea* Deep Sea Research Part I: Oceanographic Research Papers, 51(7), 921-952

[64] *Mantziafou, A. and Lascaratos, A., 2008: Deep-water formation in the Adriatic Sea: Interannual simulation for years 1979?1999* Deep Sea Research Part I: Oceanographic Research Papers, 55(11), 1403-1427

[65] *Marchesiello, P., Williams, J. M., Shchepetkin, A., 2001. Open boundary conditions for long-term integrations of regional oceanic models* Ocean Modelling, 3(1-2), 1?20

[66] *Marshall, J., Speer, K., 2012: Closure of the meridional overturning circulation through Southern Ocean upwelling* Nature Geoscience, 5(3), 171-180

[67] *Masina, S., Pinardi, N., 1994: Mesoscale data assimilation studies in the middle Adriatic sea* Continental Shelf Research 14 (12) 1293?1310

[68] *Materia, S., Dirmeyer, P.A., Guo, Z., Alessandri, A., Navarra, A., 2010. The Sensitivity of Simulated River Discharge to Land Surface Representation and Meteorological Forcings* J. Hydrometeor, 11, 334-351

[69] *Medhycos, 2001. The Mediterranean hydrological cycle observing system. Medhycos phase II, period 2002-2005* report no. 17, pp. 36

[70] *Mellor, G., and Blumberg, A., 2004. Wave breaking and ocean surface layer ther- mal response* J. Phys. Oceanogr., 34 (3), 693?698

[71] *Michelato, A., Kovacevic, V., 1991. Some dynamic features of the flow through the Otranto Strait* Bollettino di Oceanologia Teorica ed Applicata, 9, 39?51

[72] *Miglietta, M.M., Regano, A., 2008. An observational and numerical study of a flash-flood event over south-eastern Italy* Nat. Hazards Earth Syst. Sci., 8, 1417-1430

[73] *Milliman, J.D., 2001. Delivery and fate of fluvial water and sediment to the sea: a marine geologist?s view of European rivers* Scientia Marina 65 (Suppl. 2), 121? 132

[74] *Milliman, J. D., and Farnsworth, K. L., 2013. River discharge to the coastal ocean: a global synthesis* Cambridge University Press.

[75] *Munk, W., Wunsch, C., 1998. Abyssal recipes II. Energetics of tidal and wind mixing* Deep Sea Research Part I: Oceanographic Research Papers, 45(12), 1977-2010

[76] *Moeng, C. H., Dudhia, J., Klemp, J., Sullivan, P., 2007. Examining two-way grid nesting for large eddy simulation of the PBL using the WRF model* Monthly Weather Review, 135(6), 2295-2311

[77] *Monin, A.S. and A.M. Obukhov, 1954. Basic laws of turbulent mixing in the surface layer of the atmosphere* Contrib. Geophys. Inst. Acad. Sci., USSR, (151), 163-187

[78] *Moscatello, A., Miglietta, M.M., Rotunno, R., 2008. Observational analysis of a Mediterranean 'hurricane" over south-eastern Italy* Weather, Vol.63, N 10

[79] *Nickovic, S., Pejanovic, G., Djurdjevic, V., Roskar, J., and Vujadinovic, M., 2010. HYPROM hydrology surface-runoff prognostic model* Water Resour Res, 46, W11506

[80] *Niu, G.-Y., Z.-L. Yang, R. E. Dickinson, and L. E. Gulden, 2005. A simple TOPMODEL-based runoff parameterization (SIMTOP) for use in GCMs* J. Geo- phys. Res., 110

[81] *Niu, G. Y., Yang, Z. L., Dickinson, R. E., Gulden, L. E., Su, H. 2007. Development of a simple groundwater model for use in climate models and evaluation with Gravity Recovery and Climate Experiment data* Journal of Geophysical Research: Atmospheres (1984-2012), 112(D7)

[82] *Niu, G.-Y., et al. 2011. The community Noah land surface model with multiparameterization options (Noah-MP): 1. Model description and evaluation with local-scale measurements* J. Geophys. Res., 116, D12109

[83] *Oddo, P., Pinardi, N., Zavatarelli, M., 2005: A numerical study of the interannual variability of the Adriatic Sea (2000?2002)* Science of The Total Environment, 353(1-3), 39-56

[84] *Oddo, P., Guarnieri, A., 2011. A Study of the hydrographic conditions in the Adriatic Sea from numerical modelling and direct observations (2000?2008)* Ocean Sci., 7, 549-567

[85] *Pacanowski, R., Philander, S., 1981. Parameterization of vertical mixing in numerical models of tropical oceans* J. Phys. Oceanogr., 11 (11), 1443-1451

[86] *Paparella, F., Young, W. R., 2002: Horizontal convection is non-turbulent* J. Fluid Mech., 466

[87] *Pappenberger, F., Beven, K. J., Hunter, P. D., Bates, B. T., Gouweleeuw, J., Thielen, J., and de Roo, A. P. J., 2005. Cascading model uncertainty from medium range weather forecasts (10 days) through a rainfall-runoff model to flood inundation pre- dictions within the European Flood Forecasting System (EFFS)* Hydrol. Earth Syst. Sci., 9, 381-393

[88] *Pasaric, M., 2004. Annual cycle of river discharge along the Adriatic coast of Croatia* Rapports et procs-verbaux des reunions CIESMM 37, 132

[89] *Paschini, E., Artegiani, A., Pinardi, N., 1993. The mesoscale eddy field of the middle adriatic sea during fall 1988* Deep Sea Research Part I: Oceanographic Research Papers 40 (7), 1365-1377

[90] *Pedlosky, J., 1987. Geophysical Fluid Dynamics* Springer-Verlag, pp. 724

[91] *Pettenuzzo, D., Large, W. G., and Pinardi, N., 2010. On the corrections of ERA?40 surface flux products consistent with the Mediterranean heat and water budgets and the connection between basin surface total heat flux and NAO* Journal of Geophysical Research: Oceans, 115(C6)

[92] *Pickard, G. L. and Emery, W. J., 1990. Descriptive Physical Oceanography: an introduction* Elsevier

[93] *Pinardi, N., Allen, I., Demirov, E., De Mey, P., Korres, G., Lascaratos, A., Le Traon, P. Y., Maillard, C., Manzella, G., Tziavos, C., 2003: The Mediterranean ocean forecasting system: first phase of implementation (1998?2001)* Ann. Geophys., 21(1), 3-20

[94] *Pinardi, N., Arneri, E., Crise, A., Ravaioli, M., and Zavatarelli, M., 2006: The physical, sedimentary and ecological structure and variability of shelf areas in the Mediterranean Sea* The Sea, 14, 1243-1330

[95] *Pinardi, N., Coppini, G., 2010. Operational oceanography in the Mediterranean Sea: the second stage of development* Ocean Science, 6, 263-267

[96] *Pinardi, N., Masetti, E.,2000. Variability of the large scale general circulation of the Mediterranean Sea from observations and modelling: a review* Palaeogeogr. Palaeoclimatol. Palaeoecol., Volume 158, Number 3, 15 May 2000, pp. 153-173(21)

[97] *Pinardi, N., Zavatarelli, M., Adani, M., Coppini, G., Fratianni, C., Oddo, P., Tonani, M., Lyubartsev, V., Dobricic, S., Bonaduce, A., 2015. Mediterranean Sea large-scale low frequency ocean variability and water mass formation rates from 1987 to 2007: a retrospective analysis* Progress in Oceanography, 132, 318-332

[98] *Pisacane, G., Artale, V., Calmanti, S., Rupolo, V., 2006. Decadal oscillations in the Mediterranean Sea: a result of the overturning circulation variability in the eastern basin* Climate Research, 31, 257?271

[99] *Provini, A., Crosa, G., Marchetti, R., 1992. Nutrient export from Po and Adige river basins over the last 20 years* Sci. Total Environ; suppl.: 291-313

[100] *Qian, J. H., Seth, A., Zebiak, S., 2003. Reinitialized versus continuous simulations for regional climate downscaling* Monthly Weather Review, 131(11), 2857-2874

[101] Rapporto d'evento Centro Funzionale Decentrato Regione Puglia: Evento meteo-idro-pluviometrico dell'1 Marzo 2011

[102] Rapporto d'evento Centro Funzionale Decentrato Regione Puglia: Evento meteo-idro-pluviometrico del 30 Novembre-3 Dicembre 2013

[103] *Raicich, F., 1996. Note on the flow rates of the Adriatic rivers. CNR, Istituto Talassografico di Trieste Tech. Rep. RF 02/94, 8 pp*

[104] *Rahmstorf, S., 1995. Bifurcations of the Atlantic thermohaline circulation in response to changes in the hydrological cycle* Nature, 378, 145-149

[105] *Rahmstorf, S., 1996. On the freshwater forcing and transport of the Atlantic thermohaline circulation* Clim Dyn 12(12), 799-811

[106] *Roether, W., Manca, B.B., Klein, B., Bregant, D., Georgopoulos, D., Beitzel, V., Kovacevic, V., and Lucchetta, A., 1996. Recent changes in eastern Mediterranean deep waters* Science, 271, 333-335

[107] *Romano, L., Pellegrino, R., Di Santo, A.R., Fratino, U., 2009. Modellazione idraulica bidimensionale per la determinazione delle aree inondabili del fiume Ofanto* Atti 13^{ma} Conferenza Nazionale ASITA

[108] *Schiller, R.V., Kourafalou, V.H. 2010. Modeling river plume dynamics with the HYbrid Coordinate Ocean Model* Ocean Modeling, 33, 101-117

[109] *Shin, H. H., Hong, S. Y., 2013. Analysis of resolved and parameterized vertical transports in convective boundary layers at gray-zone resolutions* Journal of the Atmospheric Sciences, 70(10), 3248-3261

[110] *Simoncelli, S., Pinardi, N., Oddo, P., Mariano, A. J., Montanari, G., Rinaldi, A., Deserti., M., 2011. Coastal Rapid Environmental Assessment in the Northern Adriatic Sea* Dyn. Atmos. Oceans 52(1?2), 250-283

[111] *Simpson, J.H., Bos, W.G., Shirmer, F., Souza, A.J., Rippeth, T.P., Jones, S.E., Hydes, D., 1993. Periodic stratification in the Rhine ROFI in the North Sea* Oceanologica Acta, 16(1), 23-32

[112] *Skamarock, W. C., Klemp, J. B., Dudhia, J., Gill, D., Barker, D., Duda, M., Huang, X., Wang, W., Powers, J., 2008. A Description of the Advanced Research WRF V3*

[113] *Skliris, N., Sofianos, S., Lascaratos, A., 2007: Hydrological changes in the Mediterranean Sea in relation to changes in the freshwater budget: a numerical modelling study* Journal of Marine Systems 65, 400-416

[114] *Somot, S., Sevault, F., Deque, M., 2006: Transient climate change scenario simula- tion of the Mediterranean Sea for the twentyfirst century using a high-resolution ocean circulation model* Clim. Dyn. 27, 851-879

[115] *Spall, M., A., 2004. Boundary currents and water mass trans- formation in marginal seas* J. Phys. Oceanogr., 34, 1197-1213

[116] *Spall, M., A., 2010. Dynamics of downwelling in an eddy-resolving convective basin* J. Phys. Oceanogr., 40, 2341?2347

[117] *Spall, M., A., 2011. On the role of eddies and surface forcing in the heat transport and overturning circulation in marginal sea* J. Mar. Res., 24, 4844-4858.

[118] *Spall, M. A., 2012. Influences of Precipitation on Water Mass Transformation and Deep Convection* J. Phys. Ocean., 42, 1684-1700

[119] *Strahler, A. N., 1952. Hypsometric (area-altitude) analysis of erosional topography* Geological Society of America Bulletin, 63(11), 1117-1142

[120] *Struglia, M. V., Mariotti, A., Filograsso, A., 2004: River Discharge into the Mediterranean Sea: Climatology and Aspects of the Observed Variability* J. Climate, 17: 4740-4751

[121] *Sverdrup, H. U., 1947. Wind-driven currents in a baroclinic ocean; with application to the equatorial currents of the eastern Pacific* Proceedings of the National Academy of Sciences, 33, 318-326

[122] *Thompson, G., R. M. Rasmussen, and K. Manning, 2004. Explicit forecasts of winter precipitation using an improved bulk microphysics scheme. Part I: Description and sensitivity analysis* Mon. Wea. Rev., 132, 519-542

[123] *Tonani, M., Pinardi, N., Dobricic, S., Pujol, I., Fratianni, C., 2008. A high-resolution free surface model of the Mediterranean Sea* Ocean Sci., 4(1) 1-14

[124] *Tseng, Y.-H., Bryan, F. O., Whitney, M. M., 2016. Impacts of the representation of riverine freshwater input in the Community Earth System Model* Ocean Modelling (in revision)

[125] *Vervatis, V. D., Sofianos, S. S., Skliris, N., Somot, S., Lascaratos, A., and Rixen, M., 2013: Mechanisms controlling the thermohaline circulation pattern variability in the Aegean Levantine region. A hindcast simu-*

lation (1960-2000) with an eddy resolving model Deep Sea Research Part I: Oceanographic Research Papers, 74, 82-97

[126] *Vrsmarty, C., B. Fekete, and B. Tucker, 1996. Global River Discharge Database, RivDis* http://www.rivdis.sr.unh.edu/, U. N. Educ. Sci. And Cult. Organ., Paris

[127] *Wang, X. H., Oddo, P., Pinardi, N., 2007. On the bottom density plume on coastal zone off Gargano (Italy) in the southern Adriatic Sea and its interannual variability* J. Geophys. Res., 112 (C3)

[128] *Wu, P., and Haines, K., 1996. Modeling the dispersal of Levantine Intermediate Water and its role in Mediterranean deep water formation* J. Geophys. Res., 101, 6591-6607

[129] *Yankovsky, A.E., Chapman, D.C., 1997. A simple theory for the fate of buoyant coastal discharge* J. Phys. Oceanogr. 27, 1386-1401

[130] *Zobler, L., 1986. A world soil file for global climate modeling* National Aeronautics and Space Administration, Goddard Space Flight Center, Institute for Space Studies